ALMA MATER STUDIORUM
UNIVERSITA' DEGLI STUDI DI BOLOGNA
DIPARTIMENTO DI FISICA

Dottorato di Ricerca
GEOFISICA

Ciclo XX

ESTIMATING CRUSTAL DEFORMATION FROM GEODETIC DATA

with applications to the Messina Straits and Friuli area

Presentata da: **Daniele CHELONI**

Tutore: *Dott.* **Giulio SELVAGGI**

Co-Tutore: *Dott.* **Nicola D'AGOSTINO**

Referente: *Prof.* **Paolo BALDI**

Coordinatore Dottorato: *Chiar.mo. Prof.* **Michele DRAGONI**

Anno Esame Finale **2008**

Settore Scientifico Disciplinare **GEO/10**

INDEX

CHAPTER III GEODETIC STRAIN RATE ACROSS THE MESSINA STRAITS, SOUTHERN ITALY, FROM TRIANGULATION MEASUREMENTS BETWEEN 1971 AND 2004

CHAPTER IV INVERSION OF GEODETIC DATA FOR ESTIMATES OF SOURCE PARAMETERS

Summary

By the end of the 19th century, geodesy has contributed greatly to the knowledge of regional tectonics and fault movement through its ability to measure, at sub-centimetre precision, the relative positions of points on the Earth's surface. Nowadays the systematic analysis of geodetic measurements in active deformation regions represents therefore one of the most important tool in the study of crustal deformation over different temporal scales [e.g., *Dixon, 1991*]. This dissertation focuses on motion that can be observed geodetically with classical terrestrial position measurements, particularly triangulation and leveling observations. The work is divided into two sections: an overview of the principal methods for estimating long-term accumulation of elastic strain from terrestrial observations, and an overview of the principal methods for rigorously inverting surface coseismic deformation fields for source geometry with tests on synthetic deformation data sets and applications in two different tectonically active regions of the Italian peninsula. For the long-term accumulation of elastic strain analysis, triangulation data were available from a geodetic network across the Messina Straits area (southern Italy) for the period 1971 – 2004. From resulting angle changes, the shear strain rates as well as the orientation of the principal axes of the strain rate tensor were estimated. The computed average annual shear strain rates for the time period between 1971 and 2004 are $\dot{\gamma}_1$ = 113.89 ± 54.96 nanostrain/yr and $\dot{\gamma}_2$ = -23.38 ± 48.71 nanostrain/yr, with the orientation of the most extensional strain (θ) at N140.80° ± 19.55°E. These results suggests that the first-order strain field of the area is dominated by extension in the direction perpendicular to the trend of the Straits, sustaining the hypothesis that the Messina Straits could represents an area of active concentrated deformation. The orientation of θ agree well with GPS deformation estimates, calculated over shorter time interval, and is consistent with previous preliminary GPS estimates [*D'Agostino and Selvaggi, 2004; Serpelloni et al., 2005*] and is also similar to the direction of the 1908 (M_W 7.1) earthquake slip vector [e.g., *Boschi et al., 1989; Valensise and Pantosti, 1992; Pino et al., 2000; Amoruso et al., 2002*]. Thus, the measured strain rate can be attributed to an active extension across the Messina Straits, corresponding to a relative extension rate ranges between < 1mm/yr and up to ~ 2 mm/yr, within the portion of the Straits covered by the triangulation network. These results are consistent with the hypothesis that the Messina Straits is an important active geological boundary between the Sicilian and the Calabrian domains and support previous preliminary GPS-based estimates of strain rates across the Straits, which show that the active deformation is distributed along a greater area. Finally, the preliminary dislocation modelling has shown

that, although the current geodetic measurements do not resolve the geometry of the dislocation models, they solve well the rate of interseismic strain accumulation across the Messina Straits and give useful information about the locking the depth of the shear zone.

Geodetic data, triangulation and leveling measurements of the 1976 Friuli (NE Italy) earthquake, were available for the inversion of coseismic source parameters. From observed angle and elevation changes, the source parameters of the seismic sequence were estimated in a join inversion using an algorithm called "simulated annealing". The computed optimal uniform–slip elastic dislocation model consists of a 30° north-dipping shallow (depth 1.30 ± 0.75 km) fault plane with azimuth of 273° and accommodating reverse dextral slip of about 1.8 m. The hypocentral location and inferred fault plane of the main event are then consistent with the activation of Periadriatic overthrusts or other related thrust faults as the Gemona-Kobarid thrust. Then, the geodetic data set exclude the source solution of *Aoudia et al.* [*2000*], *Peruzza et al.* [*2002*] and *Poli et al.* [*2002*] that considers the Susans-Tricesimo thrust as the May 6 event. The best-fit source model is then more consistent with the solution of *Pondrelli et al.* [*2001*], which proposed the activation of other thrusts located more to the North of the Susans-Tricesimo thrust, probably on Periadriatic related thrust faults. The main characteristics of the leveling and triangulation data are then fit by the optimal single fault model, that is, these results are consistent with a first-order rupture process characterized by a progressive rupture of a single fault system. A single uniform-slip fault model seems to not reproduce some minor complexities of the observations, and some residual signals that are not modelled by the optimal single-fault plane solution, were observed. In fact, the single fault plane model does not reproduce some minor features of the leveling deformation field along the route 36 south of the main uplift peak, that is, a second fault seems to be necessary to reproduce these residual signals. By assuming movements along some mapped thrust located southward of the inferred optimal single-plane solution, the residual signal has been successfully modelled. In summary, the inversion results presented in this Thesis, are consistent with the activation of some Periadriatic related thrust for the main events of the sequence, and with a minor importance of the southward thrust systems of the middle Tagliamento plain.

Chapter I

Background and Motivation

1.1 Introduction

Geodesy is the scientific discipline that deals with the measurement and representation of the shape and gravity field of the Earth [e.g., *Vanicek and Krakiwsky, 1986*]. Besides the Earth's gravity field, geodesists study also many other geodynamical phenomena such as, tides, polar motion and crustal motion and includes the study of permanent crustal deformation that occurs either gradually with the steady motion of plates or suddenly with earthquakes. Hence, the systematic analysis of geodetic measurements in active deformation regions currently represents one of the most important tool in the study of crustal deformation over different temporal scales. Despite during the last decades geodetic methods and technology to measure active deformation of the Earth's crust have improved, particularly the space geodetic data derived from the Global Positioning System (GPS) and Synthetic Aperture Radar (SAR), the studies of tectonic deformation can still take advantage of classical terrestrial measurements, spanning long time of observations or being the only available measurements in some regions. In fact, repeated terrestrial geodetic observations have been successfully used to give estimates of tectonic deformation in several parts of the world, providing detailed information on ground displacements, such as how active faults move in earthquakes [e.g., *Lin & Stein, 1989; Arnadottir & Segall, 1994; Yu & Segall, 1996; Thatcher et al., 1997; King & Thatcher, 1998; Bilham & England, 2001; Nyst et al., 2006*] as well as refined estimates of the long-term accumulation of elastic strain [e.g., *Harada & Shimura, 1979; Thatcher, 1979; Savage et al., 1981; Savage, 1983; Walcott, 1984; King et al., 1987; Feigl et al., 1990; Davies et al., 1997; Hunstad et al., 2003*] over time spans of decades to a century.

The aim of this Thesis is to use terrestrial geodetic measurements to investigate crustal deformation, particularly related to two different tectonically active tectonic regions of the Italian peninsula where some open questions still remain poorly known. The first region where tectonic deformation has been analyzed is the Messina Straits area (southern Italy). This area is one of the most seismically active region of the Italian peninsula and it was struck on 1908 by a M_w 7.1 earthquake [*Boschi et al., 1995*]. Recent geodetic studies based on GPS measurements [*D'Agostino & Selvaggi, 2004; Serpelloni et al., 2005*] have pointed out that the Messina Straits can be an important boundary zone between two different domains (Calabria and Sicily) characterized by different crustal motions. Under this hypothesis, it is therefore important to define the style and kinematics along this boundary with the aim of characterizing and quantifying the strains that might be released in future earthquakes. Due to

the previous lack of a permanent GPS network across the region, estimates of crustal motion across the Straits has been relied on only a very limited number of permanent GPS stations [*D'Agostino & Selvaggi, 2004*] and/or on a small number of periodic GPS measurements [*Serpelloni et at., 2005*]. Then a precise estimate of the current strain accumulation on this presumed active structure still remains poorly known. The aim of this Thesis is to use a set of historical terrestrial geodetic observations, particularly triangulation measurements that were never elaborated in an homogeneous way, to investigate the crustal deformation accumulated in this area in relationship with the boundary kinematic condition imposed by the relative motion between the two different domains (Sicilian and Calabrian domains).

The other region where crustal deformation (on different temporal scale) has been analyzed is the Friuli region (NE Italy). This area was struck on 1976 by a sequence of moderate-to large earthquakes. Despite the 1976 Friuli earthquake has been one of the most damaging events ever recorded in Northern Italy, causing many victims and destroying large parts of several nearby localities, debate still persists about the reactivated geological structures [e.g., *Aoudia et al., 2000; Pondrelli et al., 2001; Peruzza et al., 2002; Galadini et al., 2005*]. In this Thesis, for the first time, all the geodetic displacements available, that consists of first, second and third order triangulation measurements [*IGM-RG, 1978*] plus vertical displacements from double run high-precision leveling [*Talamo et al., 1978*], were inverted to retrieve a source model for the main event that optimally fits the set of coseismic geodetic measurements. By means of the optimal source model, some considerations about the possible fault system that was reactivated during this sequence were made.

This introduction chapter provides an overview of main concepts regarding the crustal deformation models that have been developed over the last decades and finally, a short description of the organization of this Thesis.

1.2 Crustal deformation and the "seismic cycle"

With the advent of precise surveying techniques, the crustal deformation of the Earth is now routinely measured. The most obvious manifestation of active deformation of the Earth's crust is represented by earthquakes. They represent an important fraction of the Earths deformation which takes place by frictional sliding on faults, giving rise to earthquakes as a release of built-up interseismic strain. The credit for a full conceptualization of the seismic loading cycle is usually given to H. F. Reid, who worked out the theory of elastic rebound

studying the 1906 San Francisco earthquake [*1910*]. According to his *elastic rebound theory*, the causative strains of an earthquake are accumulated over a long period of time by steady motion of the regions on either side of the fault, which under normal conditions remains locked by friction. In terms of crustal deformation, the loading cycle can be divided into different phases: interseismic, coseismic and postseismic (Figure 1.1). Strain accumulates along the fault because of relative motions on either side of the fault. The fault is locked due to friction and does not move. Once the strain reaches a critical value the fault overcomes the frictional resistance and the strain is relaxed. Once the fault has finished slipping, the process of strain accumulation begins anew.

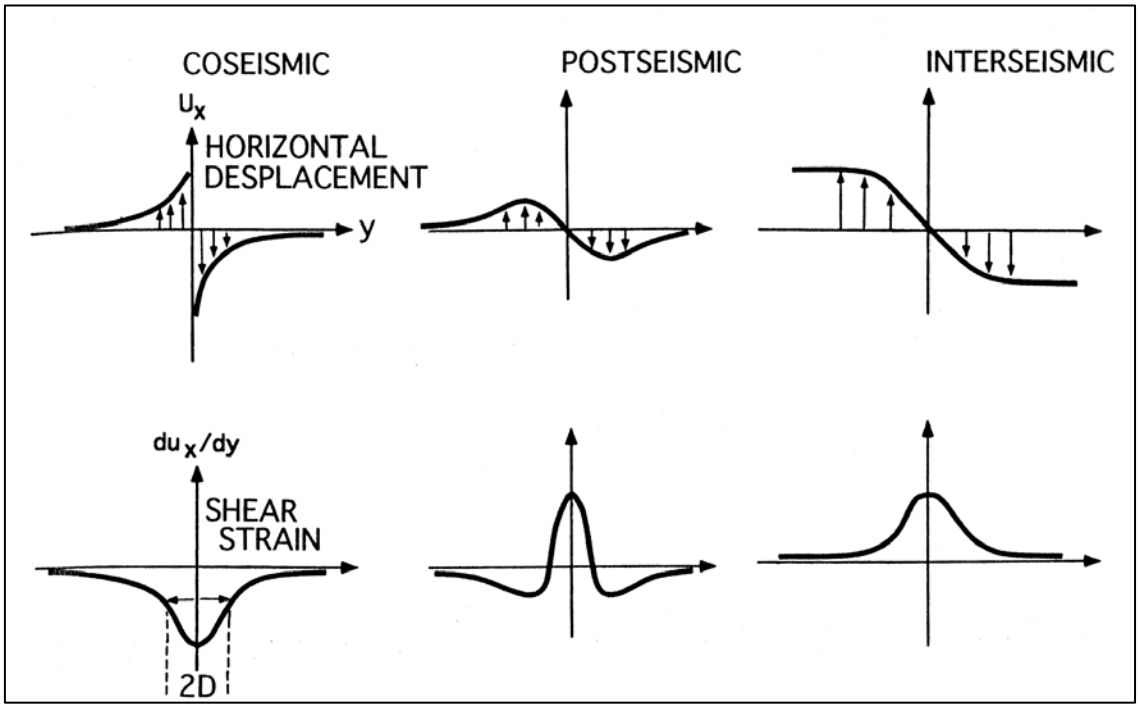

Figure 1.1 Strike-slip earthquake deformation cycle, showing horizontal displacement and shear strain component parallel to fault strike. From *Thatcher* [*1993*].

The mechanisms responsible for postseismic transient movements and steady interseismic deformation are uncertain, and two constrasting models have been proposed (Figure 1.2). In the first, the depth of coseismic faulting, D, is much less than the thickness, H, of the elastically strong lithospheric plate. Postseismic movements are caused by episodic slip immediately downdip of the coseismic rupture segment, while interseismic deformation is due to steady aseismic fault slip at greater depths. For the thin lithosphere model, $D/H \approx 1$, and bulk flow of the underlying weak layer accounts for inter-earthquake deformation in the elastic lithosphere.

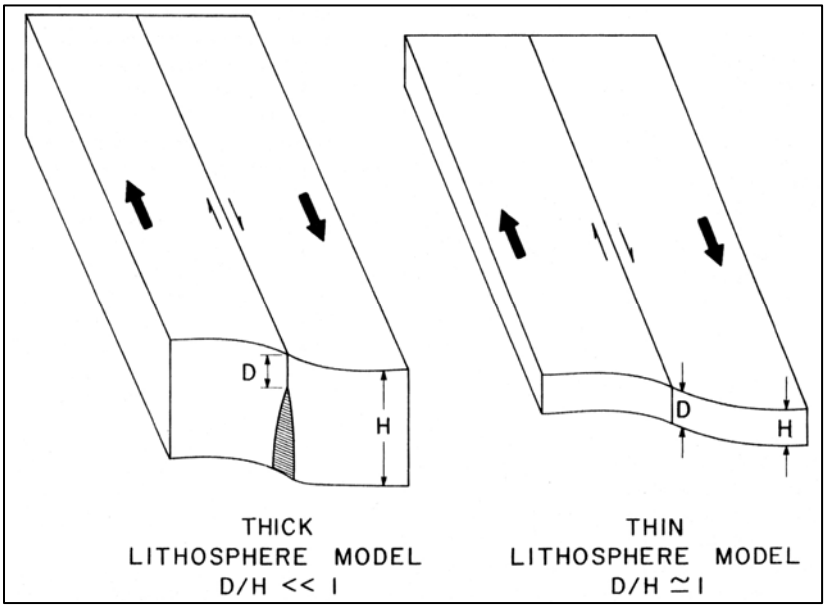

Figure 1.2 Two models for the earthquake deformation cycle on a strike-slip fault. Depth of coseismic slip = *D*, thickness of elastic lithosphere = *H*. From *Thatcher* [*1993*].

This two contrasting models for the cycle produce movements at the Earth's surface that are observationally indistinguishable [e.g. *Savage and Prescott, 1978*]. For this reason, the simplest and most common representation of strain accumulation along a long, straight fault is described by means of a vertical cut (the fault) in an elastic half-space (Figure 1.3a). Accordingly to this model, during the interseismic phase, that is, between earthquakes, the movement occur only below a certain depth *D* (namely locking depth) by extending the dislocation to infinite depth. These movements load the locked fault segment to failure. Then, the locked segment abruptly slip, during an earthquake, and so it relocks and the cycle begins anew. This representation of the earthquake cycle is the "conventional" way to describe the seismic loading cycle, and this formulation provides the same surface displacements as a model with an elastic plate (lithosphere) of thickness *D* over a viscoelastic half-space (asthenosphere) (Figure 1.3b) [*Savage, 1990*].

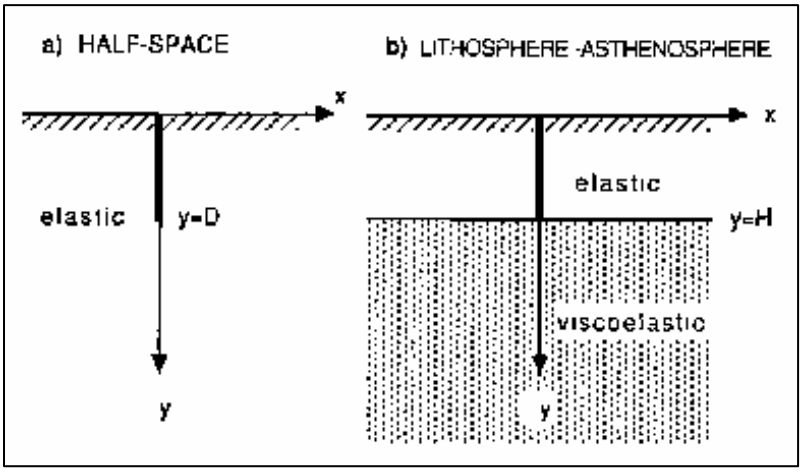

Figure 1.3 Earth models employed to describe the earthquake cycle, for the specific case of a straight transform fault. The site of coseismic rupture is shown by the heavy vertical line segment ($y=D$; $y=H$, respectively). From *Savage* [*1990*].

The cycle of earthquake strain accumulation and release can be observed using repeated geodetic survey measurements, and thus, these data can be successfully inverted to retrieve information about the seismic source on the fault (Figure 1.4) as well as rate of interseismic loading and the geometry (e.g., azimuth, dip, locking depth) of the shear zone at depth (Figure 1.5).

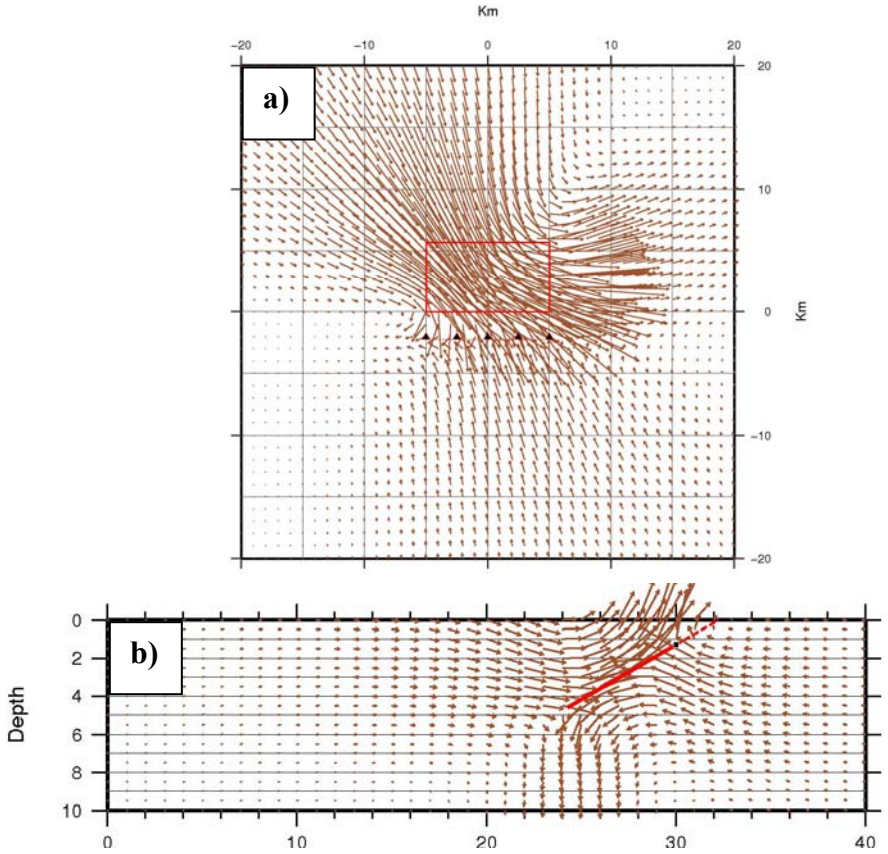

Figure 1.4 Example of coseismic dislocation modelling. The arrows represents the horizontal (a) and the vertical (b) displacements predicted by the coseismic dislocation plane depicted in red.

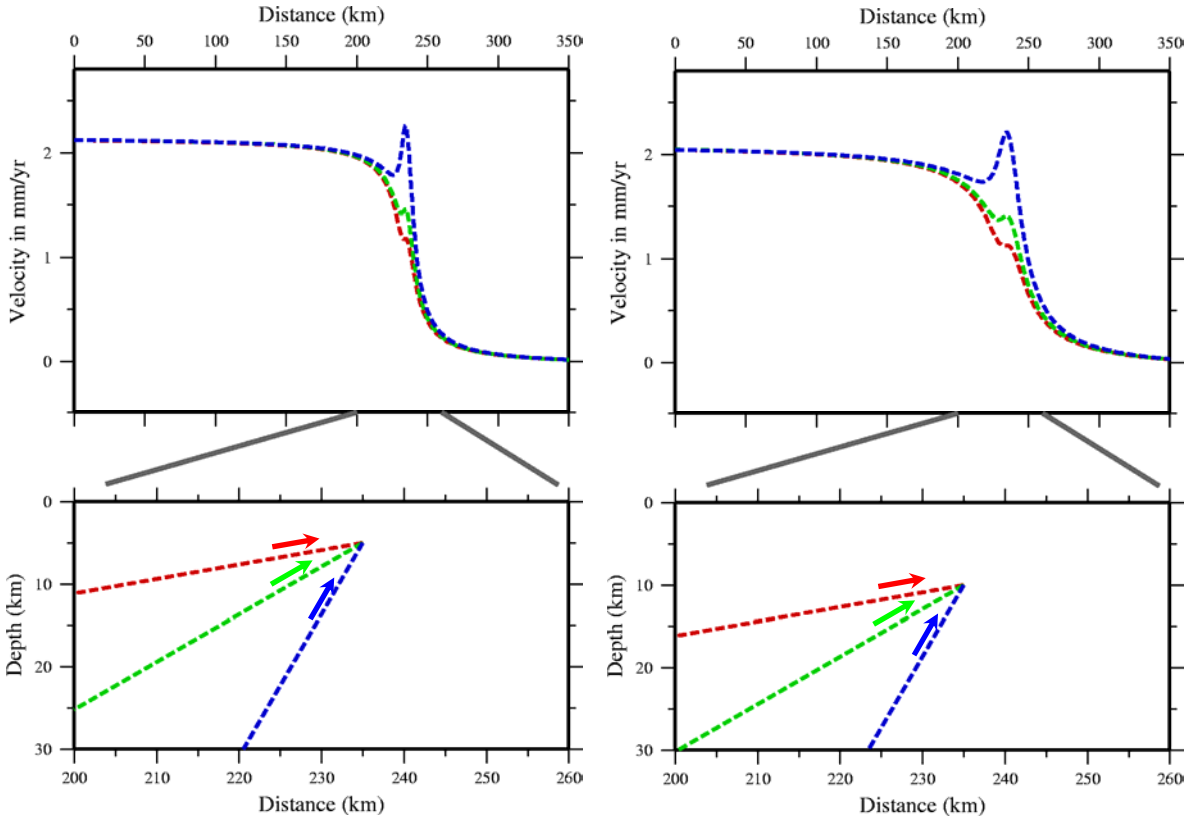

Figure 1.5 Examples of interseismic dislocation modelling. The different coloured lines indicate different geometry parameters of the shear zones. On the left the chosen locking depth is equal to 5, while on the right is 10 km. The arrows indicate the direction of motion.

1.3 Thesis organization

The aim of this Thesis is use terrestrial geodetic measurements to investigate crustal deformation, particularly related to two different active tectonic regions of the Italian peninsula. The Thesis is then composed of two separate sections: the analysis of interseismic strain accumulation and the analysis of coseismic deformation for deriving the source parameters. Following this introduction (Chapter I), the two different sections are each covered in two chapters. Chapter 2 presents an overview of the principal methods for rigorously inverting surface deformation fields for long-term accumulation of elastic strain, with tests on synthetic deformation data sets. In Chapter III the methods described in the previous section are applied to real geodetic data sets, which samples the 1971-2004 interseismic deformation field across the Messina Straits area (southern Italy).

Chapter IV discusses the analysis of the coseismic deformation fields, with an overview of the principal methods for rigorously inverting surface deformation fields for source geometry, with tests on simulated data. In Chapter V, ground motions accompanying the 1976 Friuli earthquake is investigated by means of some of the methods described in the previous chapter. A last Chapter (VI) contains final conclusions and closing remarks.

Chapter II

Inversion of Geodetic Data for Estimates of Crustal Strain Rate

2.1 Introduction

By providing a direct image of crustal motion, geodetic observations can contribute to quantify the deformation accumulated by a tectonic structure in relationship with the boundary kinematic condition imposed by the relative motion between tectonic plates. Moreover, classical terrestrial geodetic observations can be used to extend the time of observations of crustal deformation up to a century. For this reason, geodetic determinations of strain over time spans of decades to a century represent a valuable tool for assessing the long-term accumulation of elastic strain, and hence the seismic hazard of a region. Inversion of geodetic data for estimating crustal deformation is an example of the more general class of inverse problems. In this chapter, after an overview about how the deformation of the crust can be described, the methods for estimating crustal strain from terrestrial geodetic measurements are presented.

2.2 Displacement field

The displacement of a material point from its initial to its final position during deformation is represented by the vector **u**. Using a mutually orthogonal set of axis, x_1, x_2 and x_3, the vector **u** has components u_1, u_2 and u_3 in these coordinate directions. If we image a displacement field in which all movement is in the 1-direction, and a displacement varying only in the 1-direction:

$$\mathbf{u} = (u_1(x_1), 0, 0) \tag{2.2.1}$$

then the displacement at x_1 is $u_1(x_1)$ and at $x_1 + \Delta x_1$ it is $u_1(x_1 + \Delta x_1)$. Then there would be only one gradient of the displacement, by definition:

$$\frac{du_1}{dx_1} = \lim_{\Delta x_1 \to 0}\left(\frac{u_1(x_1 + \Delta x_1) - u_1(x_1)}{\Delta x_1}\right) \tag{2.2.2}$$

By the definition of the derivate, the change in displacement, Δu, is:

$$\Delta u_1 = u_1(x_1 + \Delta x_1) - u_1(x_1) = \Delta x_1 \frac{du_1}{dx_1} \tag{2.2.3}$$

If the displacements are still in the 1-direction only, but they now vary in all 3 dimensions, the three partial derivates of u_1, with respect to the three coordinate directions, must be considered:

$$\Delta u_1 = \Delta x_1 \frac{du_1}{dx_1} + \Delta x_2 \frac{du_1}{dx_2} + \Delta x_3 \frac{du_1}{dx_3} \tag{2.2.4}$$

If the displacement has a component in each of the three coordinate directions, and each of these components has gradients in each of the three directions, the total change in displacement is:

$$\begin{pmatrix} \Delta u_1 \\ \Delta u_2 \\ \Delta u_3 \end{pmatrix} = \begin{bmatrix} \frac{\partial u_1}{\partial x_1} & \frac{\partial u_1}{\partial x_2} & \frac{\partial u_1}{\partial x_3} \\ \frac{\partial u_2}{\partial x_1} & \frac{\partial u_2}{\partial x_2} & \frac{\partial u_2}{\partial x_3} \\ \frac{\partial u_3}{\partial x_1} & \frac{\partial u_3}{\partial x_2} & \frac{\partial u_3}{\partial x_3} \end{bmatrix} \begin{pmatrix} \Delta x_1 \\ \Delta x_2 \\ \Delta x_3 \end{pmatrix} \tag{2.2.5}$$

The array of terms contained between square brackets is known as the *displacement gradient tensor*. Denoting the displacement gradient tensor by **L**, and introducing the indicial notation:

$$\Delta u_I = L_{ij} \Delta x_j \tag{2.2.6}$$

The displacement gradient tensor can be spitted up into a part which represents strain and a part which represents rotation:

$$L_{ij} = \varepsilon_{ij} + \omega_{ij} = \frac{1}{2}\left(\frac{\partial u_i}{\partial x_j} + \frac{\partial u_j}{\partial x_i}\right) + \frac{1}{2}\left(\frac{\partial u_i}{\partial x_j} - \frac{\partial u_j}{\partial x_i}\right) \tag{2.2.7}$$

Not all combinations of displacement gradients produce changes of shapes. Some combinations merely produce rotation, without change of shape:

$$\begin{bmatrix} L_{11} & L_{12} & L_{13} \\ L_{21} & L_{22} & L_{23} \\ L_{31} & L_{32} & L_{33} \end{bmatrix} = \begin{bmatrix} \varepsilon_{11} & \varepsilon_{12} & \varepsilon_{13} \\ \varepsilon_{21} & \varepsilon_{22} & \varepsilon_{23} \\ \varepsilon_{31} & \varepsilon_{32} & \varepsilon_{33} \end{bmatrix} + \begin{bmatrix} 0 & \omega_{12} & \omega_{13} \\ \omega_{21} & 0 & \omega_{23} \\ \omega_{31} & \omega_{32} & 0 \end{bmatrix} \tag{2.2.8}$$

2.3 Measuring crustal strain using conventional triangulation

A variety of geodetic methods offers the possibility of compute deformations. Each of them, as well as their combinations, provide either full or partial strain information. The observed quantities involved in the strain determination, lead either to a direct or indirect determination of strain parameters. Furthermore, a statistical analysis of the results is always necessary, since the observations are not free from errors.

By the end of the 19th century, geodesy had reached a plateau: measurements of angles could be made to a precision that was limited only by the fact that these angles had to be measured through the Earth's atmosphere. Fluctuations in the refractive index of air usually limited the precision with which angles could be measured to about 1 second of arc. For this reason, analysis of triangulation data to determine earth deformation has become an important tool in the understanding of the deformation processes. Where triangulation networks have been regularly re-observed, the common means of analysis is to determine appropriate components of the strain tensor.

2.3.1 Frank's method

The methodology commonly used for evaluating tectonic strain from triangulation measurements has been established by *Frank* [*1966*] and relies in repeated observations being made of angles of a network. The component of the strain tensor that can be directly recovered from every repetition of survey on a triangulation network are the so called *shear strain*. Considering a velocity gradient of the form:

$$L = \begin{bmatrix} L_{11} & L_{12} \\ L_{21} & L_{22} \end{bmatrix} \tag{2.3.1}$$

where the vertical gradients of the horizontal velocity has been supposed not exist (because they are in any case unobservable from triangulation measurements), the rate of rotation of a material line, changed by this horizontal deformation field is:

$$\dot{\theta}_1 = L_{11}\cos\theta_1\sin\theta_1 + L_{12}\sin^2\theta_1 - L_{21}\cos^2\theta_1 - L_{22}\cos\theta_1\sin\theta_1 \tag{2.3.2}$$

where θ_1 is the angle between the considered line and the 1-axis. Similarly, the rotation of a second line going through the same point, having an orientation θ_2, would be:

$$\dot{\theta}_2 = L_{11}\cos\theta_2\sin\theta_2 + L_{12}\sin^2\theta_2 - L_{21}\cos^2\theta_2 - L_{22}\cos\theta_2\sin\theta_2 \tag{2.3.3}$$

The difference between these rates of rotation leads to the quantity that can be observed in triangulation networks, namely changes in angles:

$$\dot{\theta}_1 - \dot{\theta}_2 = \frac{(L_{11} - L_{22})}{2}(\sin 2\theta_1 - \sin 2\theta_2) + L_{12}(\sin^2\theta_1 - \sin^2\theta_2) - L_{21}(\cos^2\theta_1 - \cos^2\theta_2) \tag{2.3.4}$$

This equation may be rearranged to give:

$$\dot{\theta}_1 - \dot{\theta}_2 = \frac{\gamma_1}{2}(\sin 2\theta_1 - \sin 2\theta_2) + \gamma_2(\cos 2\theta_2 - \cos 2\theta_1) \tag{2.3.5}$$

where

$$\begin{aligned} \gamma_1 &= L_{11} - L_{22} \\ \gamma_2 &= L_{12} + L_{21} \end{aligned} \tag{2.3.6}$$

where L_{ij} are the components of the velocity gradient tensor and γ_1, γ_2 represent the shear strains. The difference between the magnitudes of the principal shear strains is another way of presenting the shear strains, namely the total shear strain (γ_{tot}):

$$\gamma_{tot} = \sqrt{\gamma_1^2 + \gamma_2^2} \tag{2.3.7}$$

The principal axes of the strain tensor are invariants and can be expressed in terms of the quantities γ_1 and γ_2. The orientation, φ, of the principal axes are given by:

$$\tan(2\varphi) = \frac{\gamma_2}{\gamma_1} \tag{2.3.8}$$

Regarding the tectonic interpretation of these quantities, a positive (or negative) value of γ_1 has the meaning of extension (or contraction) along x_1, contraction (or extension) along x_2 direction or a combination of both. A positive (or negative) γ_2 corresponds to right-lateral shear (or left-lateral) along x_1 direction, left-lateral shear (or right-lateral) in x_2 direction (Figure 2.1).

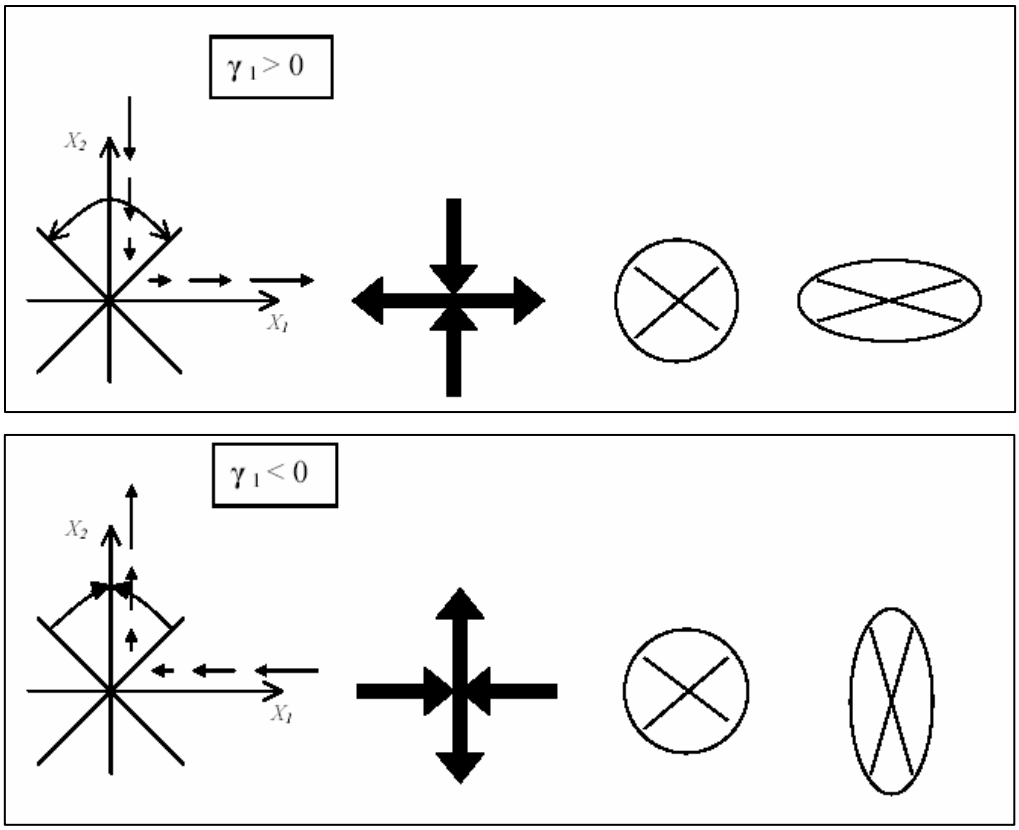

Figure 2.1 Schematic representation of the significance of the shear strains.

Now, considering a survey triangle (Figure 2.2) with side *a*, *b*, *c* taken clockwise in sequence and direction, the subtending angles at the opposite corners *A*, *B*, *C* of the triangle are:

$$\begin{aligned}\alpha_a &= \theta_b - \theta_c + 180° \\ \alpha_b &= \theta_c - \theta_a + 180°(-360°) \\ \alpha_c &= \theta_a - \theta_b + 180°\end{aligned} \tag{2.3.9}$$

where θ_a, θ_b, θ_c are the azimuths of sides *a*, *b*, *c*.

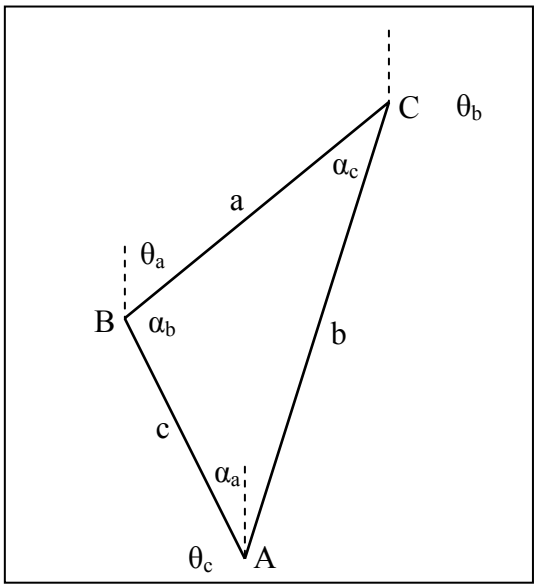

Figure 2.2 Notation for a survey triangle. Modified from *Frank* [*1966*].

Thus the angle change will be:

$$\delta\alpha_a = \delta\alpha_b - \delta\alpha_c \tag{2.3.10}$$

Hence, by assuming the same strains to operate on both vectors *b* and *c* (that is, regarding the strain as uniform over the area of the triangle):

$$\begin{aligned}\delta\alpha_a &= \frac{1}{2}(\sin 2\theta_b - \sin 2\theta_c)\gamma_1 + \frac{1}{2}(\cos 2\theta_b - \cos 2\theta_c)\gamma_2 \\ \delta\alpha_b &= \frac{1}{2}(\sin 2\theta_c - \sin 2\theta_a)\gamma_1 + \frac{1}{2}(\cos 2\theta_c - \cos 2\theta_a)\gamma_2\end{aligned} \tag{2.3.11}$$

These equations may be rewritten, using (2.3.9):

$$\begin{aligned} -\cos(\theta_b+\theta_c)\sin\alpha_a\cdot\gamma_1+\sin(\theta_b+\theta_c)\sin\alpha_a\cdot\gamma_2&=\delta\alpha_a\\ -\cos(\theta_c+\theta_a)\sin\alpha_b\cdot\gamma_1+\sin(\theta_c+\theta_a)\sin\alpha_b\cdot\gamma_2&=\delta\alpha_b \end{aligned} \tag{2.3.12}$$

Thus, the equations can be solved as simultaneous equations for the *shear strain*, γ_1 and γ_2, giving:

$$\begin{aligned} \gamma_1&=\frac{\sin(\theta_c+\theta_a)(\delta\alpha_a/\sin\alpha_a)-\sin(\theta_b+\theta_c)(\delta\alpha_b/\sin\alpha_b)}{\sin\alpha_c}\\ \gamma_2&=\frac{\cos(\theta_c+\theta_a)(\delta\alpha_a/\sin\alpha_a)-\cos(\theta_b+\theta_c)(\delta\alpha_b/\sin\alpha_b)}{\sin\alpha_c} \end{aligned} \tag{2.3.13}$$

A third equation like (2.3.11) for $\delta\alpha_c$ is not independent, and gives no additional information.

2.3.2 Prescott's method

Frank's [*1966*] method of obtaining shear strains from repeated triangulation dealt only with the angles of a single triangle, for which there are two independent angles. *Prescott* [*1976*] elaborated a method to generalize this procedure to a larger collection of independent angles. This generalization of *Frank*'s method requires that all of the angles have been observed and repeated at the same times. Under the assumptions that the strain accumulation is uniform across the area covered by the observations and that the rate of strain accumulation is constant over the time period covered by the observations, the shear strain components are replaced by their time derivates $\dot{\gamma}_1=d\gamma_1/dt$ and $\dot{\gamma}_2=d\gamma_2/dt$. A least-squares adjustment is used to obtain a single pair of $\dot{\gamma}_1$ and $\dot{\gamma}_2$. This method makes it possible to increase the signal-to-noise ratio and thus detect smaller magnitude strain fields.

An equation like (2.3.12) is formed for each repeated angle, and it is necessary now to measure all azimuths from the vertex station rather than in a particular direction around a triangle, because the angles are not necessary all of one triangle. The triangulation measurements generally consist in a direction list and angles are formed by differencing adjacent pairs of directions. Given a direction list $p_1, p_2, \ldots, p_m$ for a particular survey of a

particular station, the angles $p_2 - p_1$, $p_3 - p_2$, …, $p_m - p_{m-1}$ are formed. An observation equation is formed for each observation on an angle.

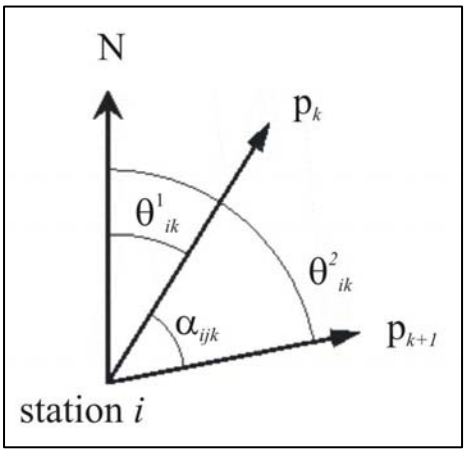

Figure 2.3 Relation between θ and α at *i*th station. The terms θ^1_{ik} and θ^2_{ik} are the azimuths of sides 1 and 2 of the *k*th angle at the *i*th station.

The observation equations take the form:

$$\alpha_{ijk} = t_{ij}\left(A^1{}_{ik}\,\dot{\gamma}_1 + A^2{}_{ik}\,\dot{\gamma}_2\right) + \alpha^0{}_{ik} \tag{2.3.14}$$

where α_{ijk} is the observed value of the k^{th} angle at the i^{th} station during the j^{th} survey; t_{ij} is the time of the j^{th} survey at the i^{th} station; $\alpha^0{}_{ik}$ is an unknown which represents the value of the k^{th} angle at station i at time $t = 0$; $A^1{}_{ik}$ and $A^2{}_{ik}$ are coefficients which depend on the orientation of the angle:

$$\begin{aligned} A^1{}_{ik} &= \left(\sin 2\theta^2{}_{ik} - \sin 2\theta^1{}_{ik}\right)/2 \\ A^2{}_{ik} &= \left(\cos 2\theta^2{}_{ik} - \cos 2\theta^1{}_{ik}\right)/2 \end{aligned} \tag{2.3.15}$$

where $\theta^2{}_{ik}$ and $\theta^1{}_{ik}$ are the azimuths of sides 1 and 2 of the *k*th angle at the *i*th station (Figure 2.3. $\dot{\gamma}_1$ and $\dot{\gamma}_2$ are the unknown strain components to be evaluated. The problem is to find, for each angle, the least-squares best-fitting straight line through the observations subject to the constraint that the slope is a function of only the shear strain rates, $\dot{\gamma}_1$ and $\dot{\gamma}_2$. The observation equations (2.3.14) are solved by traditional least-squares methods to obtain values for the unknown parameters.

2.4 Method of least-squares

Inversion of geodetic data for estimating crustal deformation is an example of a more general class of inverse problems. An inverse problem is the task that often occurs in many branches of science and mathematics where the values of some model parameter(s) must be obtained from the observed data. In regression analysis, least-squares is a method for linear regression that determines the values of unknown quantities in a statistical model by minimizing the sum of the residuals (the difference between the predicted and the observed values) squared.

The relationship between the deformation field and the strain parameters can be expressed by the explicit linear observation equation:

$$\mathbf{d} = \mathbf{G}(\mathbf{m}) + e \tag{2.4.1}$$

where **d** is the deformation data vector (i.e., the vector of observed quantities), **m** is the vector of model parameters, **G** is the function that relates the two (called data kernel) and e is a vector of observation errors. The simplest kind of solution to an inverse problem is an estimate of the model parameters. The simplest of methods for solving the linear inverse problem is based on measures of the size (i.e. length) of the estimated model parameters, $\mathbf{m}^{est}$, and of the predicted data, $\mathbf{d}^{pre}=\mathbf{G}\mathbf{m}^{est}$. This problem is often solved by the so called method of *least-squares*. The method of least-squares estimates the solution of an inverse problem by finding the model parameters that minimize a particular measure of the length of the estimated data $\mathbf{d}^{est}$, namely, its Euclidean distance from the observations (L_2 norm).

The problem of fitting a straight line to data can be used to illustrate the basic procedures applied in this technique. The model is the assertion that the data can be described by the linear equation:

$$d_i = m_1 + m_2 z_i \tag{2.4.2}$$

In this case there are two model parameters, $M = 2$, and typically there are many more than two data, that is $N > M$. Since a line is defined by precisely two points, it means that equation (2.4.2) cannot be satisfied for every i, that is, this inverse problem has no exact solution. One therefore seeks values of the model parameters that solve the equation (2.4.2) approximately, where the goodness of the approximation is defined by the error:

$$E = e^T e = \sum_i \left(d_i - m_1 - m_2 z_i\right)^2 \tag{2.4.3}$$

This problem is then solved by setting the derivates of E to zero and solving the resulting equations:

$$\begin{aligned} \frac{\partial E}{\partial m_1} &= \frac{\partial}{\partial m_1}\left[\sum_{i=1}^{N}\left[d_i - m_1 - m_2 z_i\right]^2\right] = 2m_i\sum z_i^2 + 2m_2\sum z_i - 2\sum\left(d_i z_i\right) = 0 \\ \frac{\partial E}{\partial m_2} &= \frac{\partial}{\partial m_2}\left[\sum_{i=1}^{N}\left[d_i - m_1 - m_2 z_i\right]^2\right] = 2m_i\sum z_i + 2Nm_2 - 2\sum d_i = 0 \end{aligned} \tag{2.4.4}$$

These two equations are thus solved simultaneously for m_1 and m_2, yielding the classical formulas for the least-squares fitting a line:

$$\begin{aligned} m_1 &= \frac{\left(\sum z_i^2\right)\left(\sum d_i\right) - \left(\sum z_i\right)\left(\sum z_i d_i\right)}{N\left(\sum z_i^2\right) - \left(\sum z_i\right)^2} \\ m_2 &= \frac{N\left(\sum z_i d_i\right) - \left(\sum z_i\right)\left(\sum d_i\right)}{N\left(\sum z_i^2\right) - \left(\sum z_i\right)^2} \end{aligned} \tag{2.4.5}$$

Least-squares can be extended to the general linear inverse problem, by simply computing the derivative of the error E with respect to one of the model parameters, m_q, and setting the result to zero:

$$E = \mathbf{e}^{\mathrm{T}}\mathbf{e} = (\mathbf{d} - \mathbf{G}\mathbf{m})^{\mathrm{T}}(\mathbf{d} - \mathbf{G}\mathbf{m}) = \sum_i^N \left[d_i - \sum_j^M G_{ij} m_j\right]\left[d_i - \sum_k^M G_{ik} m_k\right] \tag{2.4.6}$$

Writing in matrix notation yields:

$$\mathbf{G}^{\mathrm{T}}\mathbf{G}\mathbf{m} - \mathbf{G}^{\mathrm{T}}\mathbf{d} = 0 \tag{2.4.7}$$

where $\mathbf{G}^{\mathrm{T}}\mathbf{G}$ is a square $M \times M$ matrix which multiplies a vector $\mathbf{m}$ of length M and $\mathbf{G}^{\mathrm{T}}\mathbf{d}$ is also a vector of length M. This equation is therefore a square matrix equation for the unknown model parameters. Presuming that $[\mathbf{G}^{\mathrm{T}}\mathbf{G}]^{-1}$ exists, the least-squares solution to the inverse problem is:

$$\mathbf{m}^{est} = [\mathbf{G}^T\mathbf{G}]^{-1}\,\mathbf{G}^T\mathbf{d} \tag{2.4.8}$$

When the equation **Gm** = **d** does not provide enough information to determine uniquely all the model parameters, the problem is said to be *undetermined*. This occurs when there are more unknowns than data, that is, when $M > N$. If one were to attempt to solve this problem with least-squares, one would find that the term $[\mathbf{G}^T\mathbf{G}]^{-1}$ is singular. When there is exactly enough information to determine the model parameters, that is, when $M = N$, there is only one solution and the problem is said to be *even-determined*. The last case is when there is too much information contained in the equation **Gm** = **d** for it to possess an exact solution. This is the case in which there are more data than unknowns, that is, $N > M$. This problem is said to be *overdetermined*.

2.4.1 Weighted least-squares

Frequently some observations are made with more accuracy than others, and in this case a weighted measures of the prediction error can be useful. To accomplish this weighting, a generalized prediction error can be defined as:

$$E = e^T\mathbf{W}_e\,e \tag{2.4.9}$$

where the matrix $\mathbf{W}_e$ defines the relative contribution of each individual error to the total prediction error. Normally this matrix is a diagonal matrix (for uncorrelated data). The inverse problem solution stated above (equation 2.4.8) can then be modified to take into account these new measures of prediction error. In case of overdetermined problems, that is, when the equation **Gm** = **d** is completely overdetermined, the model parameters can be exstimated by minimizing the generalized prediction error (2.4.9), leading to the solution:

$$\mathbf{m}^{est} = [\mathbf{G}^T\,\mathbf{W}_e\,\mathbf{G}]^{-1}\,\mathbf{G}^T\,\mathbf{W}_e\,\mathbf{d} \tag{2.4.10}$$

2.4.2 The variance of the estimated model parameters

Because the observational data inevitably contain noise, this will cause errors in the estimates of the model parameters. Therefore, assuming that the data have a distribution characterized by some covariance matrix, [cov **d**], the estimates of the model parameters will have a distribution characterized by a covariance matrix [cov **m**] = **G** [cov **d**] $\mathbf{G}^{\mathrm{T}}$. If the data are uncorrelated and all of equal variance, σ_d^2, then the simple least square solution (2.4.8) has covariance:

$$[\mathrm{cov}\ \mathbf{m}] = ([\mathbf{G}^{\mathrm{T}}\mathbf{G}]^{-1}\ \mathbf{G}\ ) \sigma_d^2\, \mathbf{I}\ (\ [\mathbf{G}^{\mathrm{T}}\mathbf{G}]^{-1}\ \mathbf{G}^{-\mathrm{T}}\ )^{\mathrm{T}} = \sigma_d^2\ [\mathbf{G}^{\mathrm{T}}\mathbf{G}]^{-1} \tag{2.4.11}$$

Thus, indicating the covariance of the estimated model parameters with $\mathbf{C}_m$, and the covariance of the observational data with $\mathbf{W}_d = (\sigma_d^2)^{-1}$, the model covariance-variance matrix is:

$$\mathbf{C}_m = [\mathbf{G}^{\mathrm{T}}\, \mathbf{W}_d\, \mathbf{G}]^{-1} \tag{2.4.12}$$

2.4.3 The data resolution matrix

Once having found a generalized inverse that in some sense solves the inverse problem **d** = **Gm**, yielding an estimate of the model parameters $\mathbf{m}^{\mathrm{est}} = \mathbf{G}^{-\mathrm{g}}\ \mathbf{d}$, it is then possible to compute how well these estimates of the model parameters fits the data. By plugging these estimates into the equation **Gm** = **d**:

$$\mathbf{d}^{\mathrm{pre}} = \mathbf{G}\mathbf{m}^{\mathrm{est}} = \mathbf{G}[\mathbf{G}^{-\mathrm{g}}\mathbf{d}^{\mathrm{obs}}] = [\mathbf{G}\mathbf{G}^{-\mathrm{g}}]\mathbf{d}^{\mathrm{obs}} = \mathbf{N}\mathbf{d}^{\mathrm{obs}} \tag{2.4.13}$$

where the superscripts “obs” and “pre” mean respectively observed and predicted. The $N \times N$ square matrix $\mathbf{N} = \mathbf{G}\mathbf{G}^{-\mathrm{g}}$ is called the *data resolution matrix* [*Menke, 1984*], which describes how well the predictions match the data. The diagonal elements of the data resolution matrix indicate how much weight a datum has in its own prediction. These elements are called the *importance*, **n**, of the data [*Menke, 1984*]:

$$\mathbf{n} = \mathrm{diag}\ (\mathbf{N}) \tag{2.4.14}$$

2.5 Experiments with synthetic data

To test the efficiency of the methods described in the previous sections and test the fortran computer codes, experiments with synthetic data were made. Using elastic dislocations [*Okada, 1985*] with uniform slip, surface displacements from a velocity field are simulated. These synthetic displacements are computed in terms of angle changes and furthermore, Gaussian noise, according to an actual amount of noise, is added to these data. The test models (Figure 2.4 and 2.5) represent relatively easy problems. A forward calculation was performed to obtain relative displacements (in terms of angle changes) which are consistent with a chosen deformation field. The geometry of the synthetic model is defined in kilometric coordinates. Because of the chosen distribution of the synthetic geodetic stations (showed in Figure 2.3 and 2.4), at time T_0 the initial values of the synthetic (undeformed) angles are all equal to 45°. The model area is then deformed by applying different type of plane shear strains, corresponding to different configurations of the horizontal displacement gradient tensor (**L**).

In test case n.1 (Figure 2.4, table 2.1), the applied shear strains are equal to $\dot{\gamma}_1 = 200$ and $\dot{\gamma}_2 = 0$ nanostrain/yr[1] (azimuth of the direction of maximum extension, counterclockwise from E, equal to zero), corresponding to a displacement gradient tensor in which movements occur only along x_1 axis (the positive value of the gamma 1 shear strain indicates elongation). The displacements field was computed for three arbitrary time period ($T_2 = 2$ years; $T_{10} = 10$ years; $T_{30} = 30$ years). During this time interval the initial angles are then deformed according to the strain applied. Thus, the synthetic deformed angles, randomly perturbed in a normal distribution about their original values (using an a-priori standard deviation of 0.1 arc sec), become the input data for the inverse modeling.

In test case n.2 (Figure 2.5, table 2.2), shear strain rates of $\dot{\gamma}_1 = 0$ and $\dot{\gamma}_2 = 200$ nanostrain/yr (azimuth of the direction of maximum extension, counterclockwise from E, equal to 45°) were applied to the synthetic network, corresponding to a displacement gradient tensor in which movements correspond to right-lateral shear along x_1 direction. In table 2.4 are reported the inversion results for the different test cases. Again, the synthetic deformed angles, randomly perturbed in a normal distribution about their original values using an a-priori standard deviation of 0.1 arc sec, become the input data for the inverse modeling.

[1] Nanostrain/yr = ppm · 10^{-3}/yr

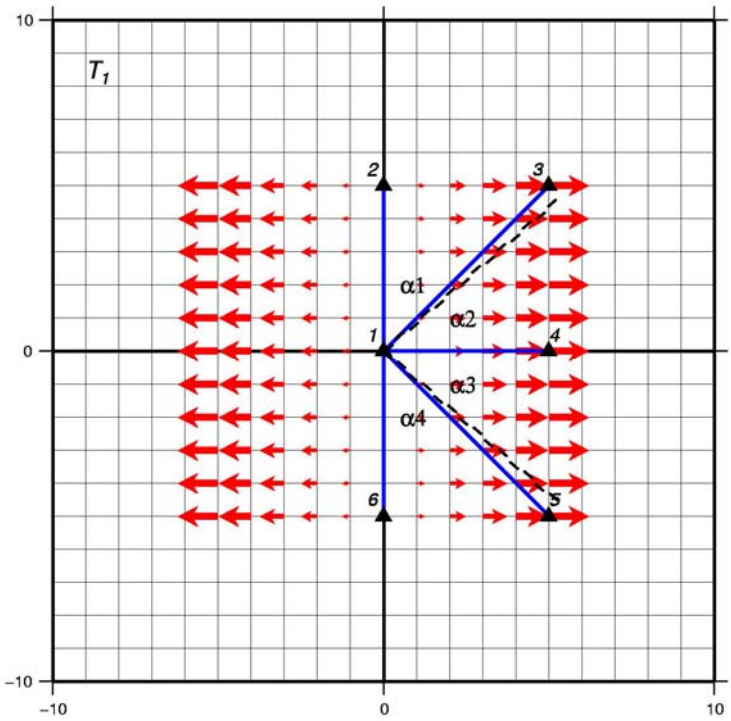

Figure 2.4 Experiment with synthetic data, Test 1. The cursive numbers indicate the geodetic station; the blue lines are the observed directions while the dashed black lines represent the deformed directions; the red arrows represent the applied strain field.

Angle			Azimuth1	Azimuth2	Time	Δα (arc sec)	Error (arc sec)
3	1	2	0	45	0	0	0.3
4	1	3	45	90	0	0	0.3
5	1	4	90	135	0	0	0.3
6	1	5	135	180	0	0	0.3
3	1	2	0	45	2	0.041	0.3
4	1	3	45	90	2	-0.041	0.3
5	1	4	90	135	2	-0.041	0.3
6	1	5	135	180	2	0.041	0.3
3	1	2	0	45	10	0.20	0.3
4	1	3	45	90	10	-0.20	0.3
5	1	4	90	135	10	-0.20	0.3
6	1	5	135	180	10	0.20	0.3
3	1	2	0	45	30	0.62	0.3
4	1	3	45	90	30	-0.62	0.3
5	1	4	90	135	30	-0.62	0.3
6	1	5	135	180	30	0.62	0.3

Table 2.1 Experiment with synthetic data, Test 1.

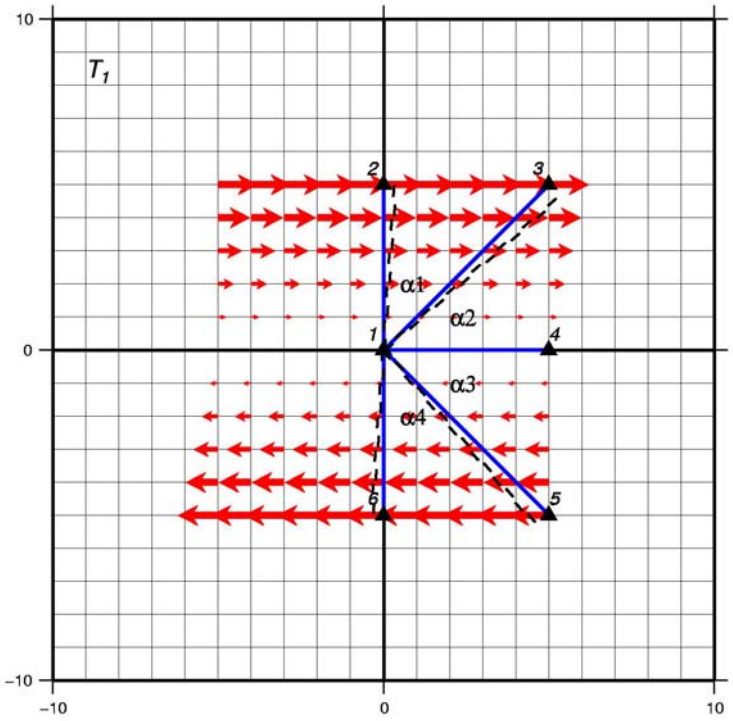

Figure 2.5 Experiment with synthetic data, Test 2. The cursive numbers indicate the geodetic station; the blue lines are the observed directions while the dashed black lines represent the deformed directions; the red arrows represent the applied strain field.

Angle			Azimuth1	Azimuth2	Time	Δα (arc sec)	Error (arc sec)
3	1	2	0	45	0	0	0.3
4	1	3	45	90	0	0	0.3
5	1	4	90	135	0	0	0.3
6	1	5	135	180	0	0	0.3
3	1	2	0	45	2	-0.041	0.3
4	1	3	45	90	2	-0.041	0.3
5	1	4	90	135	2	0.041	0.3
6	1	5	135	180	2	0.041	0.3
3	1	2	0	45	10	-0.20	0.3
4	1	3	45	90	10	-0.20	0.3
5	1	4	90	135	10	0.20	0.3
6	1	5	135	180	10	0.20	0.3
3	1	2	0	45	30	-0.62	0.3
4	1	3	45	90	30	-0.62	0.3
5	1	4	90	135	30	0.62	0.3
6	1	5	135	180	30	0.62	0.3

Table 2.2 Experiment with synthetic data, Test 2.

Test case	Synthetic shear strains			Modelled shear strains		
	Gamma1	Gamma2	Azimuth	Gamma1	Gamma2	Azimuth
1	*200.00*	*0.00*	*90.00*	*178.09±20.39*	*6.98±17.44*	*88.85*
2	*0.00*	*200.00*	*45.00*	*-21.85±15.39*	*216.26±13.17*	*42.11*

Table 2.3 Inversion results for the two test cases. The shear strains are in nanostrain/yr; the azimuths are in degrees counterclockwise from E.

2.6 Examples from the Italian area

Terrestrial geodetic observations have been successfully used to give estimates of tectonic deformation in several parts of the world, providing detailed information on ground displacements, such as refined estimates of the long-term accumulation of elastic strain [e.g., *Harada & Shimura, 1979; Thatcher, 1979; Savage et al., 1981; Savage, 1983; Walcott, 1984; King et al., 1987; Feigl et al., 1990; Davies et al., 1997; Hunstad et al., 2003*] over time spans of decades to a century. With respect to the Italian area, *Hunstad et al.* [*2003*] have successfully determined geodetic strain rates by the GPS re-measurement of the first order triangulation network of Italy, over a time span of 126 years, by using the methodology of *Frank* [*1966*]. Their results have provided important constraints about the location of the tectonically active areas of the Italian peninsula (Figure 2.6) as well as the rates of active deformation, confirming that the "classical" geodetic measurements can be successfully used in tectonic studies.

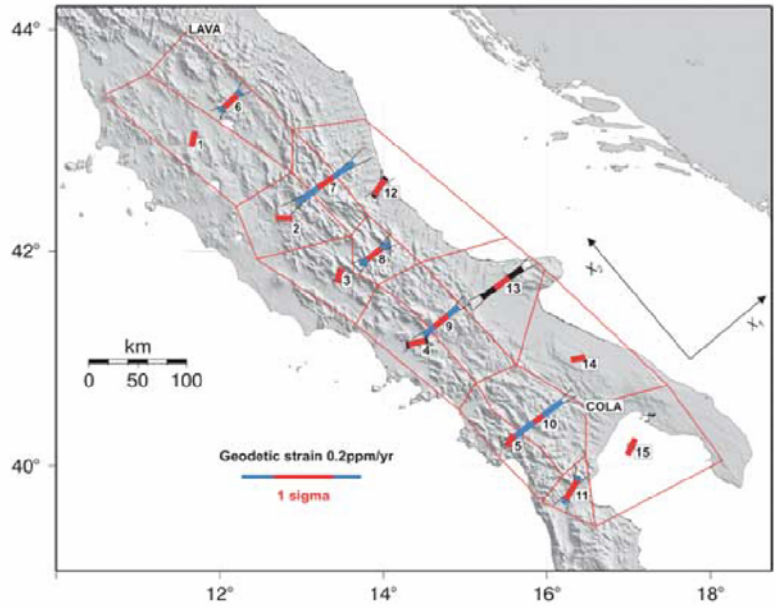

Figure 2.6 An example of geodetic strain estimation from triangulation data. The bars are proportional to the shear strain rates for the different polygonal areas [*Hunstad et al., 2003*].

2.7 Conclusions

Despite the advent of space geodetic techniques, classical terrestrial geodetic measurements can still be considered an important tool for estimating active crustal deformation, in such regions where modern space-based geodetic tools have not been available or for increasing the time span covered by the observations. Among other terrestrial geodetic technique, triangulation measurements has been considered in this Thesis. Where triangulation networks have been regularly re-observed, the common means of analysis is to determine appropriate components of the strain tensor. *Frank* [*1966*] and *Prescott* [*1976*] provided a method to estimate the shear strain components of the strain tensor by means of repeated angle observations. The observation equations are then solved by traditional least-squares methods to obtain values for the unknown shear strain parameters. Therefore, repeated triangulation measurements have been used successfully for decades to estimate crustal deformation. The synthetic experiments confirm that the written computer code reliably retrieves the model parameters of the synthetic data sets and that it is able to retrieve the shear strain parameters from the synthetic angular data. In the next Chapter the above method is applied to real observational data, related to a local triangulation network across the Messina Straits area (southern Italy).

Chapter III

Geodetic Strain Rate Across the Messina Straits (southern Italy) from Triangulation Measurements between 1971-2004

3.1 Introduction

The Messina Straits area is one of the most seismically active region of the Italian peninsula and it was struck on December 1908 by a M_w 7.1 earthquake [e.g., *Boschi et al., 1995; Valensise and Pantosti, 1992; Pino et al., 2000*]. Recent geodetic studies based on both permanent and campaign mode GPS measurements [*D'Agostino and Selvaggi, 2004; Serpelloni et al., 2005*] have pointed out that the Messina Straits can be an important boundary zone between two different domains (Calabria and Sicily) characterized by different crustal motions. Under this hypothesis, it is therefore important to define the style and kinematics along this boundary with the aim of characterizing and quantifying the strains that might be released in large earthquakes. Due to the current lack of a dense permanent GPS network across the region, estimates of crustal motion across the Straits has been relied on only a very limited number of permanent GPS stations [*D'Agostino and Selvaggi, 2004*] and/or on periodic GPS measurements [*Serpelloni et al., 2005*]. Then a precise estimate of the current strain accumulation on this presumed structure remains poorly known. The aim of this Chapter is to use a set of historical terrestrial geodetic observations, particularly triangulation measurements that were never elaborated in an homogeneous way, to investigate the possible crustal deformation accumulated by this presumed boundary zone in relationship with the boundary kinematic condition imposed by the relative motion between the two different domains. Finally, by using an elastic dislocation modelling, the rate of interseismic loading and the geometry of the shear zone at depth, will be preliminary investigated.

3.2 Seismotectonic setting

The Messina Straits is a narrow basin structure located between the Sicilian and Calabrian domains, in a crucial sector of the complex, articulated plate boundary zone between the Eurasian and African plates [*McKenzie, 1972*] (Figure 3.1). Over the Neogene and Quaternary times the evolution of this part of the plate boundary zone is generally interpreted in terms of slow relative plate convergence [*Argus et al., 1989; DeMets et al., 1994*] and fast subduction and roll-back of the Ionian lithosphere beneath the Calabrian Arc associated with back arc extension in the Tyrrhenian Sea [*Malinverno and Ryan, 1986; Patacca et al., 1990; Gueguen et al., 1998; Faccenna et al., 2001; Rosenbaum et al., 2002*]. Today, the slab is imaged by

seismic tomography and by earthquakes which deepen to the northwest down to about 500 km beneath the southeastern Tyrrhenian Sea (Figure 3.1) [*Giardini and Velonà, 1988; Amato et al., 1993; Selvaggi and Chiarabba, 1995; Wortel and Spakman, 2000*].

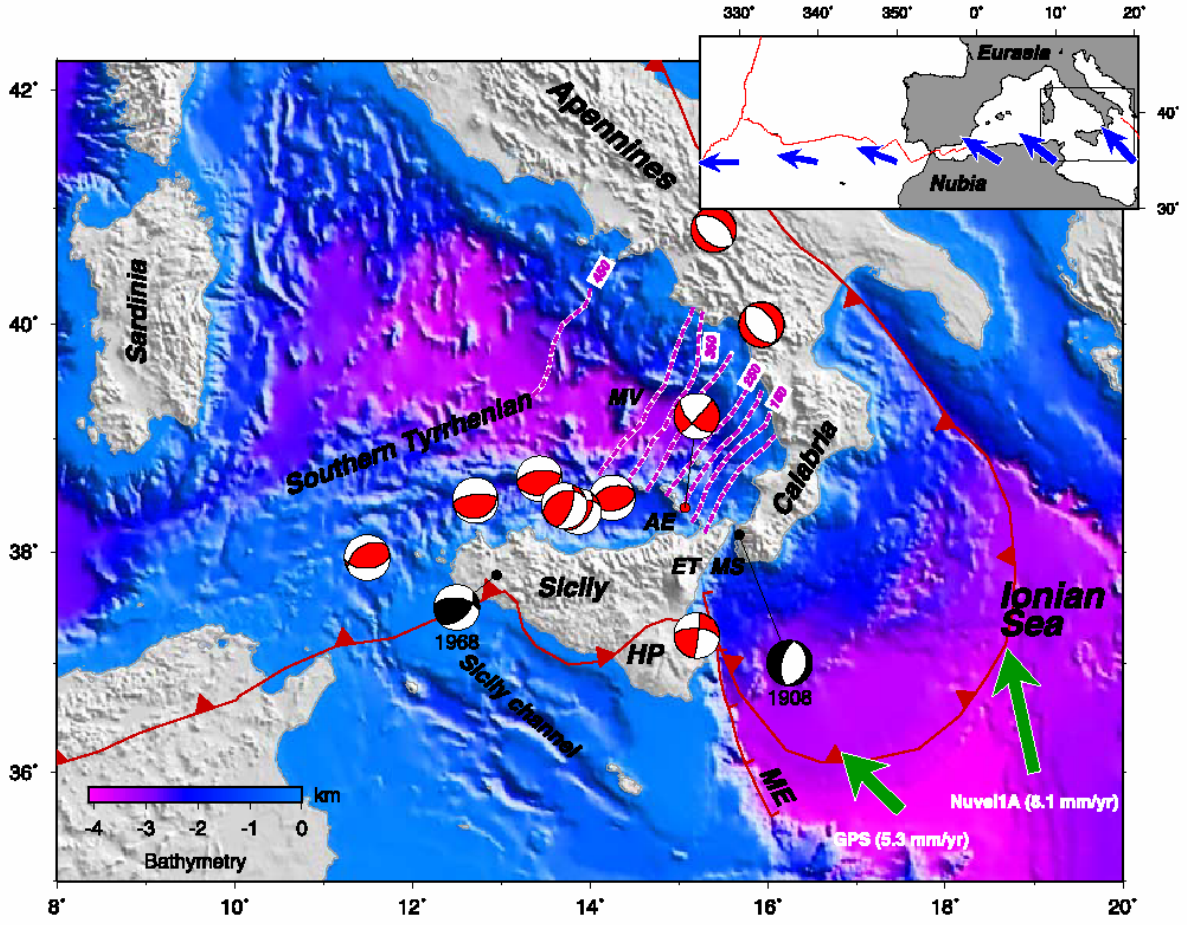

Figure 3.1 Regional tectonic map of the central Mediterranean area. Focal mechanisms are from CMT Catalog (M_W > 5, in red) and from *Anderson and Jackson* [1987] in black. The red lines show the trace of the Plio-Pleistocene subduction front and the Malta escarpment. Also shown the contours of the subducted slab labelled in kilometres (from *Frepoli et al.,* [*1996*]). The convergence vectors between Nubia and Eurasia are shown in green (according to both the Nuvel1A model and GPS pole of rotation). The inset shows the convergence vectors along the Eurasia and Nubia plate predicted by the GPS pole of rotation. Abbrevations mean: AE, Aeolian Islands; Et, Mount Etna; HP, Hyblean Plateau; ME, Malta Escarpment; MS, Messina Straits; Mv, Marsili Volcano. From *D'Agostino and Selvaggi* [*2004*].

The current instrumental seismicity (Figure 3.2) shows that crustal seismicity (depth < 35 km) is especially concentrated along the Calabrian Arc, around the Etna volcano and in a E-W trending narrow belt north of Sicily, whereas deep and intermediate earthquakes seismicity is confined east of the Aeolian Islands, marking the Ionian slab subducted beneath the Tyrrhenian Sea [*D'Agostino and Selvaggi, 2004*]. Although the subduction of the Ionian lithosphere has been characterized during the Neogene and Quaternary by a vigorous trench

retreat and back arc extension at a geological estimate rate of 50-70 mm/yr [*Patacca et al., 1990; Faccenna et al., 2001*], the current CGPS measurements show that, although subduction may be still active, the Tyrrhenian basin is not actively spreading [*D'Agostino and Selvaggi*].

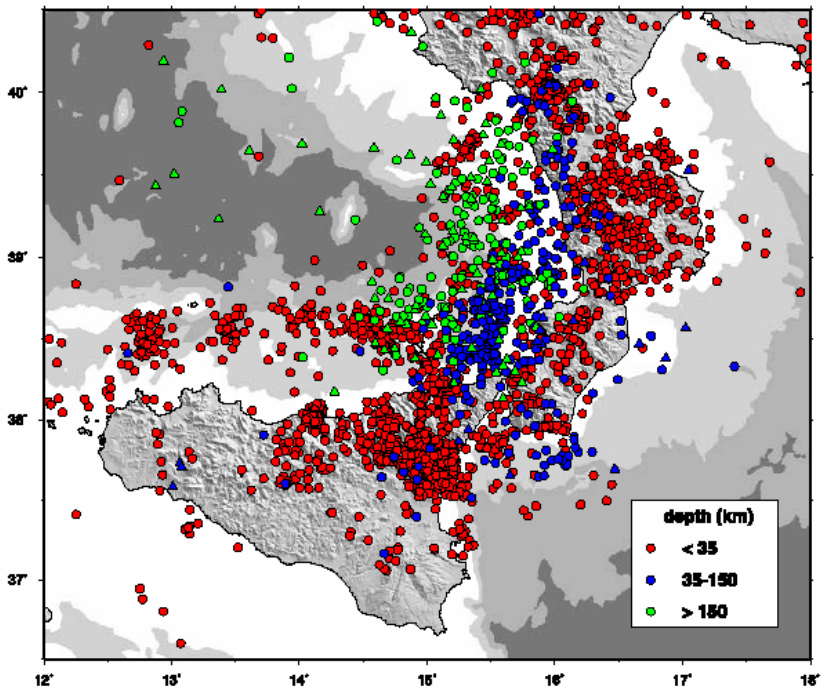

Figure 3.2 Seismicity map of the Calabrian Arc and Sicily. The earthquakes are from the Italian National Seismic Network [*Chiarabba et al., 2005*] for the period 1984-2001 (circles) and from the catalog of *Engdahl et al.,* [*1998*]. From *D'Agostino and Selvaggi* [*2004*].

Active tectonics in eastern Sicily and in the Calabrian domain is dominated by normal faulting in the Messina Straits and along the Tyrrhenian side of Calabria, describing a continuous extensional belt across the front of the Apennine-Maghrebian thrust and fold-belt [*Tortorici et al., 1995*]. The Messina Straits appears to be bordered by a system of high-angle antithetic NNE-SSW oriented normal faults (Figure 3.3) [*Ghisetti, 1984*]. This area, one of the most seismically active parts of the Italy, was struck on 28 December 1908 by a M_w 7.1 normal-faulting earthquake that was one of the greatest events ever recorded in the Central Mediterranean area and other several large events (M > 6) have taken place in the past in this area [*Boschi et al., 1997*]. Previous geological, geodetic and seismological studies have hypothesized that a NNE-SSW trending active normal fault parallel to the strike of the Straits, with variable oblique components, is responsible for the 1908 earthquake (Figure 3.3) [e.g., *Schick, 1977; Boschi et al., 1989; Valensise and Pantosti, 1992; Pino et al., 2000; Amoruso et al., 2002*].

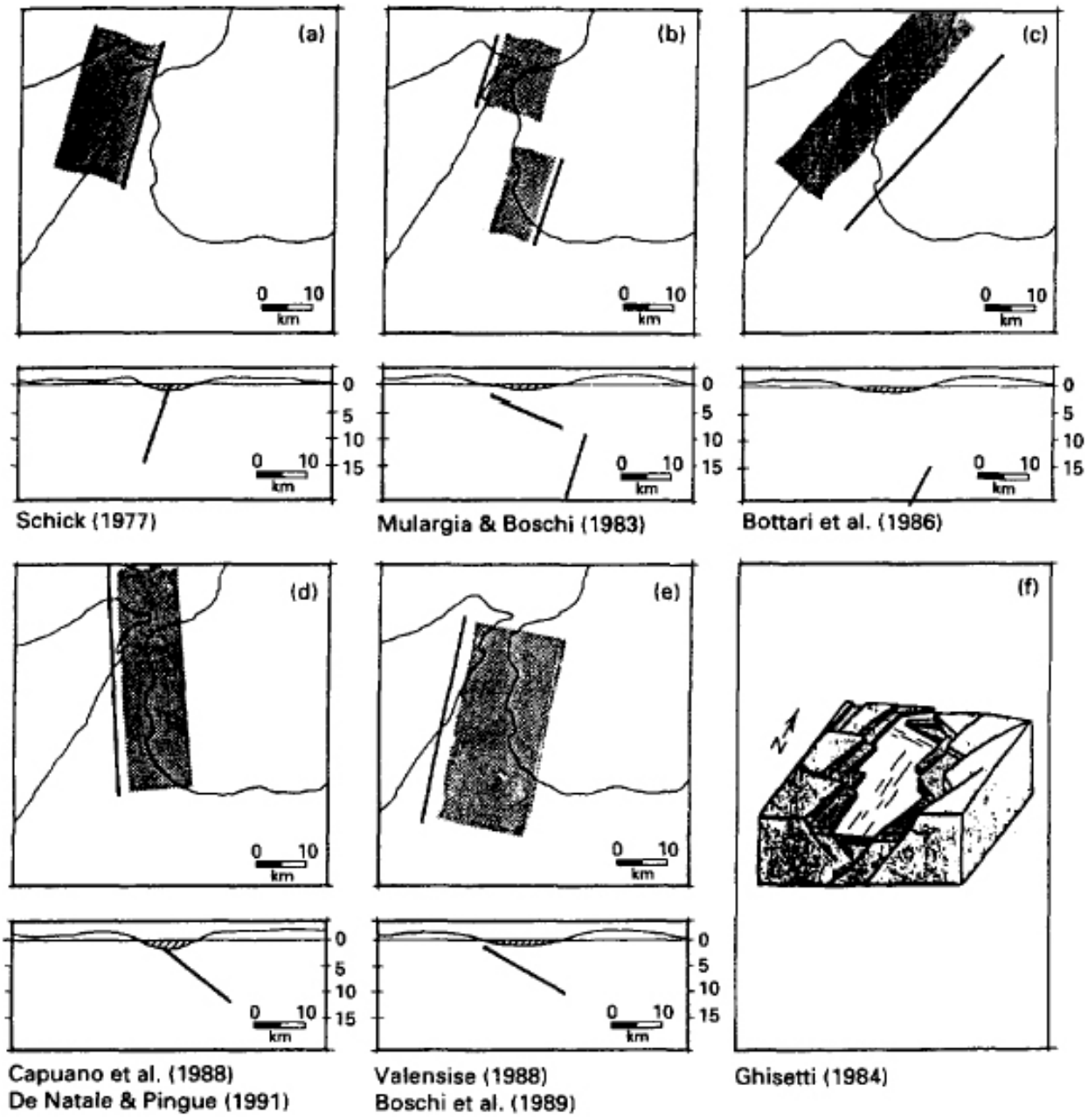

Figure 3.3 Published source modes of the 1908 earthquake, based on seismological, levelling and macroseismic observations. From *Valensise and Pantosti,* [*1992*].

More recently, a detailed study of raised Holocene shorelines [*Ferranti at al., 2007*] tentatively attributed to the 10 km exposed-onland Scilla normal fault, located along the Calabrian side of the Straits (Figure 3.4), a slip rate up to 1.1 mm/yr, that is, potentially absorbing a considerable part of the relative motion between the Sicilian and Calabrian blocks in this area.

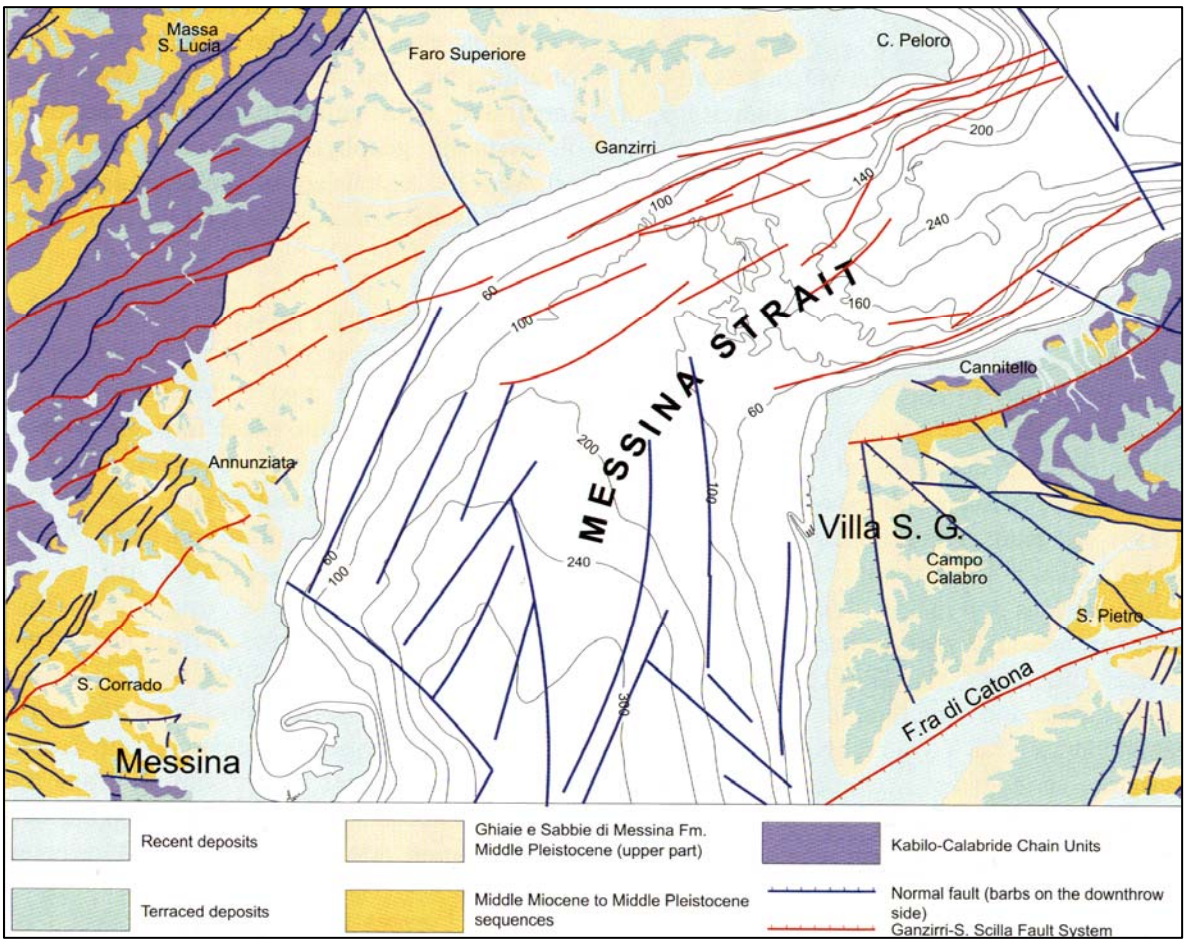

Figure 3.4 Tectonic scheme of the Messina Straits area, showing the distribution of the "Ghiaie e Sabbie di Messina" Fm. and the recent fault systems that affected the whole area. From *Guarnieri et al.,* [*2004*].

However, although the Messina Straits seems to be characterized by an extensional tectonic regime, that can be accommodated by faults situated on both sides of the Straits, the rate of interseismic loading and the geometry of the shear zone at depth is still unknown. Furthermore, although this is beyond the scope of this Thesis, it should be remarked that the regional kinematic framework in which active extension occurs in the Messina Straits is still a matter of debate [*D'Agostino and Selvaggi, 2004*].

3.3 Previous geodetic studies of active deformation across the Straits

Geodetic studies aimed at the measurement of active crustal deformation across the Messina Straits have been made since the early 1970s by different institutions. Nevertheless, evidence of active deformation have since remained elusive until very recent days. Regarding the early studies, the Messina Straits has been monitored by terrestrial surveys since the 1970 and different kind of geodetic networks were set up across the Straits.

In 1970 a control network was set up by *Caputo et al.* [*1974*]. The measurements of this network were repeated 8 time from 1970 to 1980 (Figure 3.5) in order to check the possible planimetric deformations [*Caputo et al., 1981*]. All the linear elements of the quadrilateral that has two points on the Calabrian coast and two on the Sicilian one (Figure 3.5), were measured by means of a laser geodimeter, whereas the angular elements were determined only in 1970, 1979 and 1980. Based on these measurements, *Caputo et al.* [*1981*] suggested that a shift of Sicily toward the NNE (respect to Calabria) can be observed, with a maximum value in the period between the first two measurements in September 1970 and June 1971.

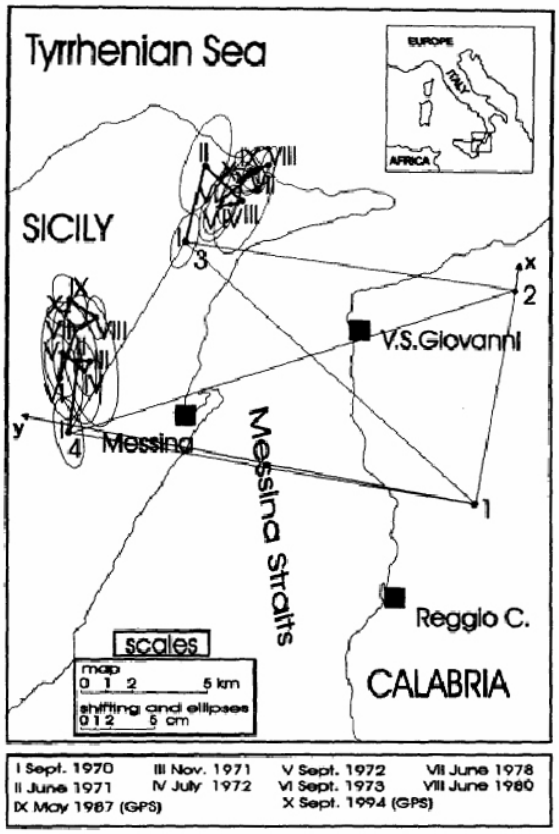

Figure 3.5 Network across the Messina Straits and displacement vectors and error ellipses suggested by the analysis of the terrestrial (from 1970 to 1980) and and the GPS (from 1987 to 1994) measurements. From *Anzidei et al.,* [*1998*].

Baldi et al. [*1983*] performed a levelling campaign along the levelling baseline of the Istituto Geografico Militare dated 1970 with the attempt to derive a picture of the current tectonic deformations in the region. They concluded that a differential subsidence of the coastlines of the Messina Straits can be observed by the levelling measurements.

Another planimetric geodetic network (see next paragraph for more details) was set up in 1971 by the Istituto Geografico Militare for the geodetic control of the Straits [*Bencini, 1975*]. According to *Arca et al.* [*1986*], the differences between both the angular and distance measurements carried out between 1971 and 1986, ranged between the limits of accuracy of the different determinations, excluding over the time span covered by the observations, any important crustal movements across the Messina Straits.

The first experimental space-based geodetic measurements across the Straits, were performed in 1987, and reported in *Achilli et al.* [*1988*], when the old terrestrial network of *Caputo et al.* [*1974, 1981*] was surveyed again by means of GPS technique (Figure 3.5). In 1994 a wider network was established and surveyed again to collect additional GPS observations [*Anzidei et al., 1998*]. Based on the analysis of the results obtained from the two GPS surveys with respect to those achieved by the previous terrestrial surveys, the authors concluded that the comparison between the 1987 and 1994 GPS surveys does not show any significant crustal deformation across the Straits during the time interval covered by the observations.

In more recent years, the improvement of the accuracy of the space-geodetic GPS technique, gives rise to new geodetic studies aimed at measuring the crustal deformation in this area. *Hollestein et al.* [*2003*] analyzed campaign mode GPS measurements, carried out between 1994 and 2001 with the aim to infer important constraints on the Africa-Eurasia plate boundary zone in southern Italy. Regarding the particular zone considered in this Thesis, according to these authors, possible extension across the Messina Straits could be evaluated from only two sites (PACE e PORO, Figure 3.6) that showed a small lengthening component, but due to the associated error, this estimate was considered to be insignificant.

D'Agostino and Selvaggi [*2004*] and *Serpelloni et al.* [*2005*] combined the periodic GPS observations with the solution of continuous GPS measurements in order to obtain a dense station coverage in the study area. According to these authors, the resulting combined GPS velocity field (Figure 3.7) shows a sudden increase in velocity across the Messina Straits up to 3 mm/yr, corresponding to a SE extensional strain rate of ~ 100 nanostrain/yr (Figure 3.7).

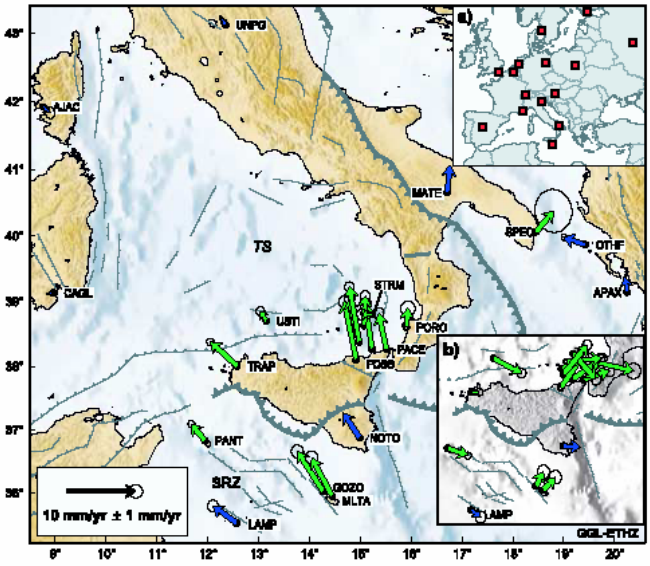

Figure 3.6 GPS velocities relative to Eurasia. Green arrows indicate campaign mode GPS measurements, while blue arrows are continuous GPS measurements. From *Hollenstein et al.,* [*2003*].

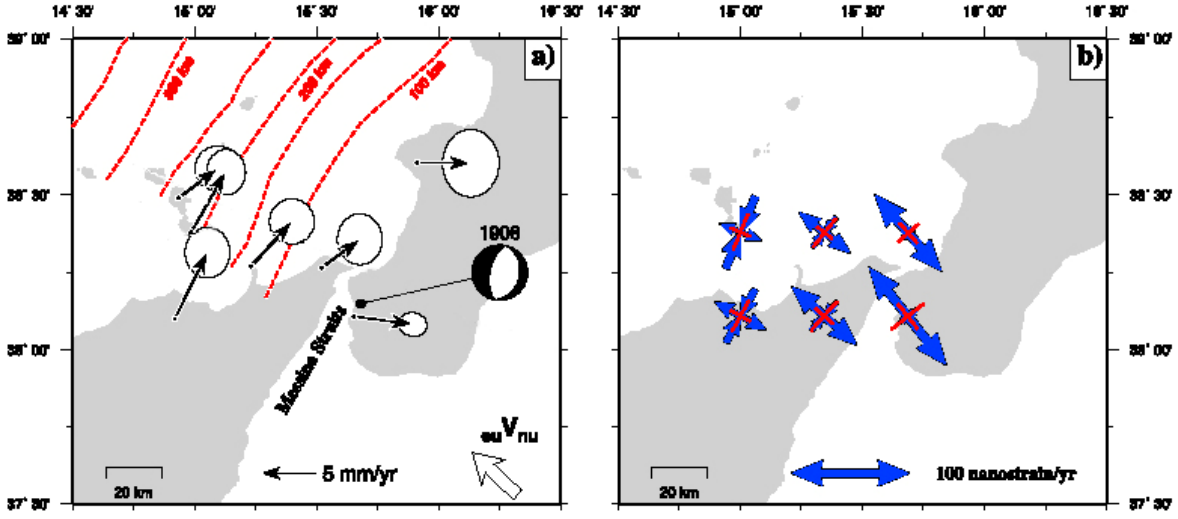

Figure 3.7 (a) Combined velocity solution in a Nubia reference frames. The thin dashed lines represent the depth contours of the Ionian slab. Also shown is the focal mechanisms of the 1908 earthquake. (b) Principal axes of the horizontal strain rate tensor (in blue) and associated 1 sigma errors (in red). From *D'Agostino and Selvaggi* [*2004*].

Due to the current lack of a dense permanent GPS network across the region, estimates of crustal motion across the Straits has been relied on only a very limited number of permanent GPS stations [*D'Agostino and Selvaggi, 2004*] and/or on periodic GPS measurements [*Serpelloni et al., 2005*]. Then a precise estimate of the current strain accumulation on this

presumed structure remains poorly known. The aim of this Chapter is to use the triangulation measurements collected by IGMI, never previously elaborated in an homogeneous way, to investigate the accumulated crustal deformation.

3.4 Geodetic data: the triangulation network

The data used in this study consist of horizontal observations of direction made in triangulation surveys between 1971 and 2004. In the early 70s of the last century the IGMI (Istituto Geodetico Militare Italiano) established a small net of trigonometric points, measured with the maximum possible accuracy [*Bencini, 1975*], through the Messina Straits, with the double aim to provide a precise geometric basis for the project and the execution of the bridge and railway connection over the Straits and to ascertain, by repeating the measurements, the existence or absence of movements of the terrain and to evaluate their size. The resurveys of this network were performed in 1973, 1986 and finally in 2004. The network consists of 7 horizontal trigonometric points, the first three situated in Calabria and the other four in Sicily, at distances ranging between 3 to 9 km (Figure 3.8).

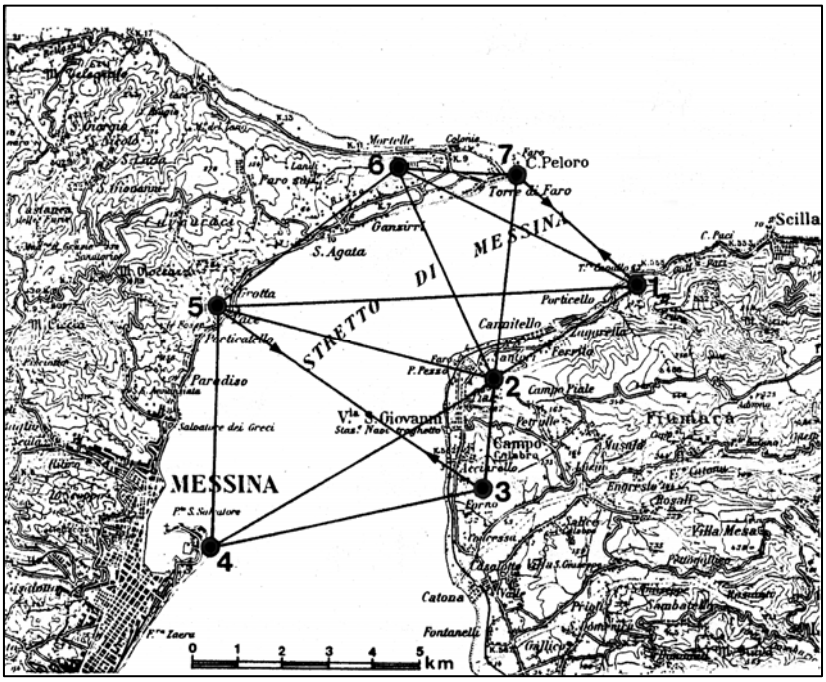

Figure 3.8 Scheme of the planimetric network established in 1971 by the Istituto Geografico Militare Italiano for the geodetic control of the Straits. Modified from *Bencini* [*1975*].

Each point has been monumented in a special way (Figure 3.9) to avoid variations due to an accidental local shifting of the station pillars [*Bencini, 1975*]. The angular stations were observed by means of a Wild T3 theodolite, by the set-of-directions method, making 24 observations in each directions (distributed into four group of six observations each) executed during different days and time, using the same procedures and instruments for all the surveys.

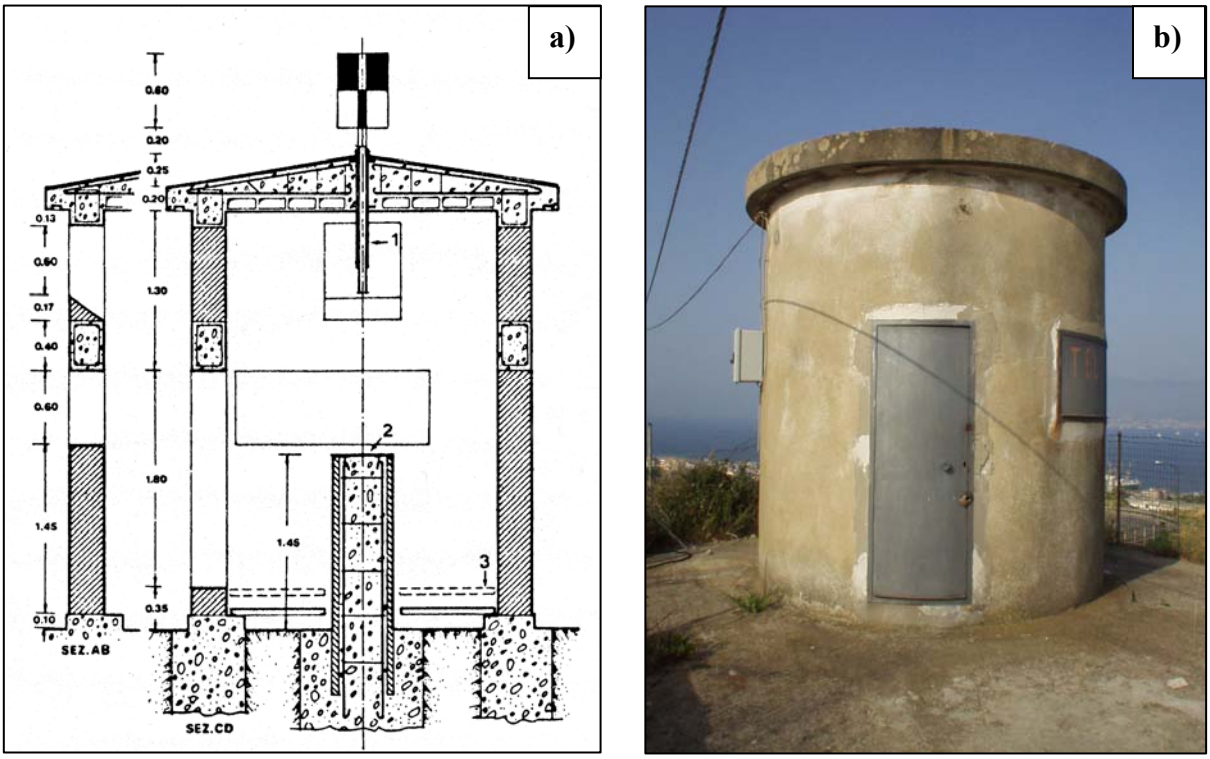

Figure 3.9 (a) Schematic plan of the pill-box built around a trigonometric point. Each point has been monumented with a circular pillar formed by a 50-cm diameter cement tube, filled with reinforced concrete and standing on a solid foundation also made of concrete. On the top of each pillar, a bronze circular plate has been fixed, 40 cm in diameter and 1 cm thick, the centre of which marks the trigonometric point. Moreover, the pillars have been protected with circular pill-boxes made of masonry and concrete, built on foundations independent from those of the pillars and supplied with openings which can be closed by means of strong iron frames, facing in the directions where the points to be observed are situated. Modified from *Bencini* [*1975*]. (b) Recent picture of a point of the network.

Because one trigonometric point was not repeated in the last survey, our final data set does not contain observations from and to that point, and finally consists of 12 repeated angles for each survey (Table 3.1). Although the average direction list has been available from *Arca et al.* [*1986*], the original handwritten campaign data were recovered from the Department of Geodesy of the Istituto Geografico Militare Italiano in Florence (courtesy of IGMI), in order to remove possible errors due to transcription. The original data are in forms of directions list, and for each direction a set of 24 observations was made. Then, all the

average directions were newly computed from the original campaign observations. Only, small differences were found between the published and the newly computed values in a couple of points. The 2004 data has not been published yet, and so this was the first time that they has been analyzed (courtesy of the I.G.M.I.). In Figure 3.10 the observed angle changes are showed, relative to the first measurement.

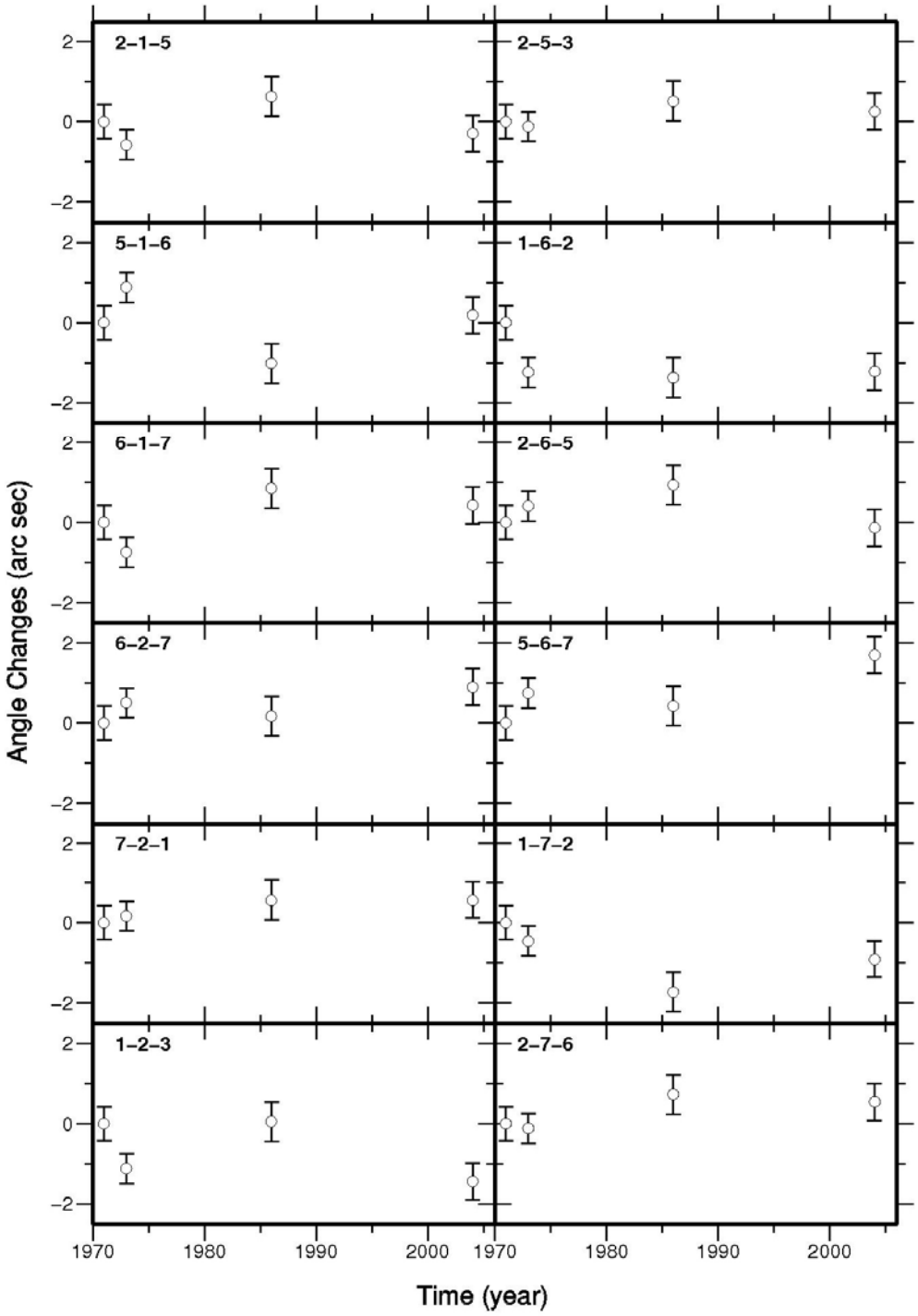

Figure 3.10 Observed angle changes measurements from 1971 to 2004. The white circles represent the observed angle changes at each epoch relative to the first measurement, with the associate 1σ errors.

Triangle			Δα (1971-1973)	Δα (1971-1986)	Δα (1971-2004)
A	**V**	**B**	arc sec	arc sec	arc sec
2	1	5	-0.5699	0.6300	-0.2900
5	1	6	0.8899	-1.0100	0.1900
6	1	7	-0.7400	0.8500	0.4300
6	2	7	0.5100	0.1800	0.9000
7	2	1	0.1699	0.5699	0.5699
1	2	3	-1.1099	0.0600	-1.4299
2	5	3	-0.1199	0.5199	0.2599
1	6	2	-1.2300	-1.3600	-1.2099
2	6	5	0.4100	0.9399	-0.1300
5	6	7	0.7499	0.4299	1.700
1	7	2	-0.4500	-1.7199	-0.9000
2	7	6	-0.1099	0.7299	0.5500

Table 3.1 The observed angle changes relative to the first measurement. Abbreviations: A, V and B are triangle vertices; Δα is the angle change. The angle vertex is at the station listed under V and is clockwise from AV to BV.

In determining the accuracy of the triangulation measurements, the method of triangle closure was adopted (for more details see paragraph 1.4.2). Using the *Ferrero's* formulation [e.g., *Bomford, 1980; Cross, 1990*] the standard error (σ_α) of an observed angle in a network of N closures is given by:

$$\sigma_\alpha = \sqrt{\frac{\sum_{i=1}^{N} \varepsilon^2}{3N}} = 0.72\varepsilon_m \qquad (3.4.1)$$

where ε_m is the average triangle closures. The average closure error of the triangles for the 4 surveys are respectively 0.54, 0.36, 0.43 and 0.46 arc sec (Table 3.2). By using the (3.4.1) the average standard error of an observed angle for the different campaign surveys ranges between 0.26 and 0.38 arc sec. Triangle closures indicate therefore that the standard deviation of a single angle is approximately 0.3 arc sec, in agreement with the nominal uncertainty estimated by the IGMI for the first-order Italian trigonometric points network ($\sigma \leq$ 0.6 arc sec).

Triangle			ε (1971)	ε (1973)	ε (1986)	ε (2004)
A	**V**	**B**	arc sec	arc sec	arc sec	arc sec
1	6	7	0.64	0.57	0.50	0.60
1	5	6	0.69	0.64	0.21	0.57
1	2	5	0.55	0.32	0.29	0.66
1	2	6	0.25	0.01	0.74	0.64
1	2	7	0.32	0.35	0.33	0.36
2	3	5	0.28	0.46	0.62	0.51
2	5	6	0.99	0.31	0.66	0.23
2	6	7	0.57	0.21	0.09	0.13

Table 3.2 The observed closure errors. Abbreviations: A, V and B are triangle vertices; ε indicates the closure error.

3.5 Strain analysis

Repeated triangulation observations have been successfully used to give estimates of tectonic interseismic strain rate in several parts of the world [e.g. *Savage,* 1983*; Hunstad et al.,* 2003]. For this reason, geodetic determinations of strain rate represent a valuable tool for assessing the long-term accumulation of elastic strain, and hence the seismic hazard of a region. Generally, two different approaches can be used for the determination of strain deformation from triangulation data. The first method involves the explicit determinations of the coordinates of all sites at each epoch with respect to a reference frame (constructed from the sites that are assumed to have remained stable during the period of observation) and thus, the computation of the displacement vectors from the difference in station position. The previous geodetic studies [*Bencini, 1975; Arca et al., 1986*] were all based on this method. However, this method should introduce some errors. For example, a movement of the reference system would cause a systematic error in the derived displacement field [*Matsu'ura et a., 1980*], and moreover unavoidably, this method involves the propagation through the network of measurement errors at individual stations.

An alternative method, formulated by *Frank* [*1966*], uses directly the difference between repeated angle observations as a measure of relative deformation of the network (see paragraph 2.3 for more details), instead of the derived displacement vectors. That is, this method permits to avoid reference frame problems and to minimize the influence of systematic errors [*Hunstad et al., 2003; Nyst et al., 2006*].

The crustal strain information that can be extract from the angular changes are the so called *shear strains* (γ_1 , γ_2) and the orientation of the greatest horizontal principal axis of the strain tensor (θ), defined as [*Frank,* 1966]:

$$\gamma_1 = \frac{\partial u_1}{\partial x_1} - \frac{\partial u_2}{\partial x_2} \qquad \gamma_2 = \frac{\partial u_1}{\partial x_2} + \frac{\partial u_2}{\partial x_1} \qquad \tan 2\theta = \frac{\gamma_2}{\gamma_1} \tag{3.4.2}$$

where the terms $\partial u_i/\partial x_j$ represent the components of the displacement gradient tensor computed in a reference frame where x_1 and x_2 axes are parallel to east and north directions respectively. A positive (or negative) value of γ_1 has the meaning of extension (or contraction) along x_1, contraction (or extension) along x_2 direction or a combination of both. A positive (or negative) γ_2 corresponds to right-lateral shear (or left-lateral) along x_1 direction, left-lateral shear (or right-lateral) in x_2 direction. This approach permits to estimate the deformation parameters independent from any assumption of scale and orientation [*Hunstad et al., 2003*]. Because of the trend direction of the Straits and because this area is characterized predominantly by NW-SE extension, we choose our coordinate axes such that x_1 axis is perpendicular to, and x_2 parallel to, the trend of the Messina Straits in the study area (Figure 3.11). This means that the γ_1 shear strains reflect only extension or contraction in the x_1 direction and γ_2 shear strains represent strike-slip motion parallel to the x_2 axis.

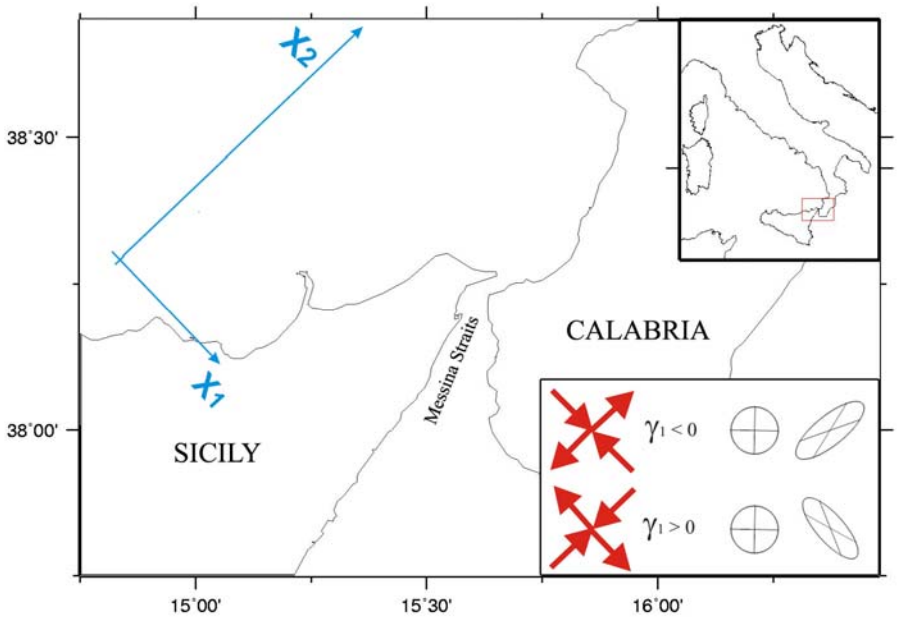

Figure 3.11 Tectonic interpretation of the shear strain rates. The x_1 and x_2 axes are taken respectively perpendicular to and parallel to the trend of Messina Straits. The inset shows the tectonic significance of the shear strain rates in this reference system.

To determine the rates of deformation the observations were processed utilizing an extended version of the *Frank*'s method [*Prescott,* 1976] that permits to adjust all of the available observations simultaneously (for more details see paragraph 2.3). This method makes it possible to increase the signal-to-noise ratio and thus detect smaller magnitude strain fields. Under the assumptions that the strain accumulation is uniform and constant over the time period covered by the observations, the time derivates of $\dot{\gamma}_1$ and $\dot{\gamma}_2$ can be calculated. An observation equation is formed for each observation of an angle:

$$\alpha_{ijk} = t_{ij}\left(A^1{}_{ik}\,\dot{\gamma}_1 + A^2{}_{ik}\,\dot{\gamma}_2\right) + \alpha^0{}_{ik} \tag{3.4.3}$$

where α_{ijk} is the observed value of the *k*th angle at the *i*th station during the *j*th survey. $t_{i,j}$ is the time of the *j*th survey at the *i*th station. $A^1{}_{ik}$ and $A^2{}_{ik}$ are coefficients which depend on the orientation of the angle (see paragraph 2.3 for more details).

The problem is to find, for each angle, the least-squares best-fitting straight line through the observations subject to the constraint that the slope is a function of only $\dot{\gamma}_1$ and $\dot{\gamma}_2$. In general *N* observed angles yield *N* independent equations like (3.4.3), from which a set of normal equations can be formed:

$$\begin{bmatrix} \alpha_{1,1971,1} \\ \alpha_{1,1971,2} \\ \cdots \\ \alpha_{1,1986,1} \\ \cdots \\ \alpha_{ijk} \end{bmatrix} = \begin{bmatrix} t_{ij}\cdot A^1{}_{11} & t_{ij}\cdot A^2{}_{11} & 1 & 0 & 0 & 0 & 0 & \ldots \\ t_{ij}\cdot A^1{}_{12} & t_{ij}\cdot A^2{}_{12} & 0 & 1 & 0 & 0 & 0 & \ldots \\ \ldots & \ldots & \ldots & \ldots & \ldots & \ldots & \ldots & \ldots \\ t_{ij}\cdot A^1{}_{11} & t_{ij}\cdot A^2{}_{11} & 1 & 0 & 0 & 0 & 0 & \ldots \\ \ldots & \ldots & \ldots & \ldots & \ldots & \ldots & \ldots & \ldots \\ t_{ij}\cdot A^1{}_{ik} & t_{ij}\cdot A^2{}_{ik} & 0 & 0 & 0 & 0 & 0 & \ldots \end{bmatrix} \bullet \begin{bmatrix} \dot{\gamma}_1 \\ \dot{\gamma}_2 \\ \alpha^0{}_{11} \\ \alpha^0{}_{12} \\ \ldots \\ \alpha^0{}_{ik} \end{bmatrix} \tag{3.4.4}$$

The observation equations (3.4.4) are then solved by traditional weighted least-squares inversion (see paragraph 2.4) to obtain values for $\dot{\gamma}_1$ and $\dot{\gamma}_2$ and $\alpha^0{}_{ik}$. However, the computation is much simplified if the origin is taken at the mean time for observations at each stations [*Prescott, 1976*]. The shift to measuring time from the mean time ($t_{ij'}$) at each station results in a much simplified matrix to be inverted (3.4.5), because $\alpha^0{}_{ik}$ unknowns can be evaluated directly and no large matrix inversion is necessary.

$$\begin{bmatrix} \alpha_{1,1971,1'} \\ \alpha_{1,1973,2'} \\ \cdots \\ \alpha_{1,1986,1'} \\ \cdots \\ \alpha_{ijk'} \end{bmatrix} = \begin{bmatrix} t_{ij'} \cdot A^1{}_{11} & t_{ij'} \cdot A^2{}_{11} \\ t_{ij'} \cdot A^1{}_{12} & t_{ij'} \cdot A^2{}_{12} \\ \cdots & \cdots \\ t_{ij'} \cdot A^1{}_{11} & t_{ij'} \cdot A^2{}_{11} \\ \cdots & \cdots \\ t_{ij'} \cdot A^1{}_{ik} & t_{ij'} \cdot A^2{}_{ik} \end{bmatrix} \bullet \begin{bmatrix} \dot{\gamma}_1 \\ \dot{\gamma}_2 \end{bmatrix} \qquad (3.4.5)$$

Because two adjacent angles have a direction in common, the observations are correlated and the usual diagonal weight matrix has been replaced by the inverse of the variance-covariance matrix. The covariance of non-adjacent angles will be zero, while the covariance of adjacent angles is given by σ_{AB}=*-1/2*σ^2_A [*Prescott,* 1976].

The resulting average annual shear strain rates are $\dot{\gamma}_1$ = 113.89 ± 54.96 nanostrain/yr and $\dot{\gamma}_2$ = -23.38 ± 48.71 nanostrain/yr, with the orientation of the most extensional strain (θ) at N140.80° ± 19.55°E (Table 3.4).

To verify that the retrieved shear strain rates are not critically affected by few angular observations, in a second inversion the observations which cumulatively provide more than 50% of the formal data importance (Figure 3.12) [*Minster et al., 1974*] (see paragraph 2.4.3 for more details) were excluded (Table 3.3).

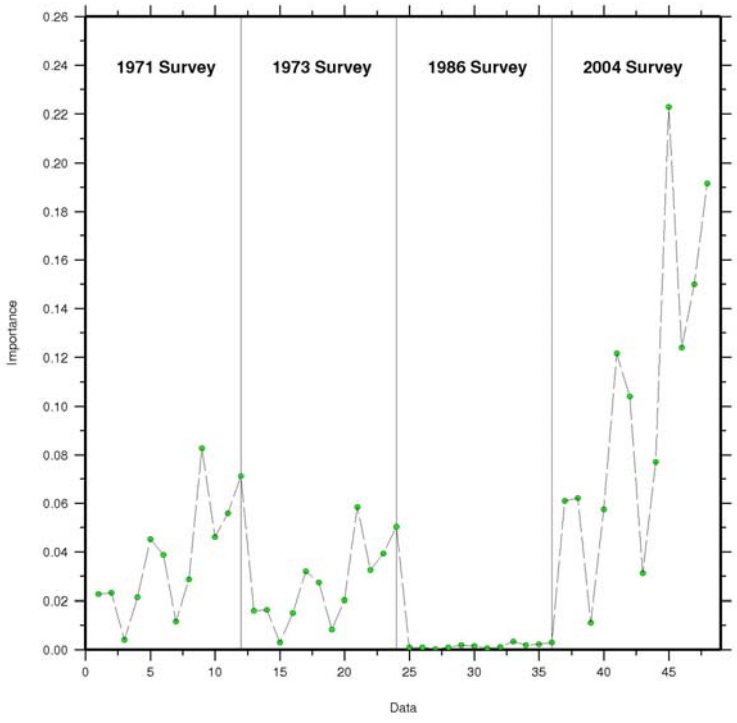

Figure 3.12 Data importance.

Angles			Survey	Importance (%)	Cum. Importance (%)
2	**6**	**5**	**2004**	***10.016***	***10.016***
2	**7**	**6**	**2004**	***8.615***	***18.632***
1	**7**	**2**	**2004**	***6.742***	***25.374***
5	**6**	**7**	**2004**	***5.566***	***30.940***
7	**2**	**1**	**2004**	***5.460***	***36.401***
1	**2**	**3**	**2004**	***4.677***	***41.079***
2	**6**	**5**	**1971**	***4.237***	***45.316***
2	**6**	**5**	**1973**	***3.980***	***49.297***
2	**7**	**6**	**1971**	***3.364***	***52.941***
1	6	2	2004	3.469	56.411
2	7	6	1973	3.423	59.834
1	7	2	1971	2.852	62.687
5	1	6	2004	2.791	65.478
2	1	5	2004	2.738	68.217
1	7	2	1973	2.679	70.896
6	2	7	2004	2.579	73.476
5	6	7	1971	2.354	75.831
7	2	1	1971	2.310	78.141
5	6	7	1973	2.212	80.353
7	2	1	1973	2.170	82.523
1	2	3	1971	1.978	84.502
1	2	3	1973	1.858	86.360
1	6	2	1971	1.467	87.828
2	5	3	2004	1.406	89.235
1	6	2	1973	1.378	90.614
5	1	6	1971	1.180	91.794
2	1	5	1971	1.158	92.953
5	1	6	1973	1.109	94.062
6	2	7	1971	1.091	95.153
2	1	5	1973	1.088	96.242
6	2	7	1973	1.025	97.267
2	5	3	1971	0.595	97.862
2	5	3	1973	0.559	98.421
6	1	7	2004	0.494	98.916
6	1	7	1971	0.209	99.125
6	1	7	1973	0.196	99.321
2	6	5	1986	0.124	99.446
2	7	6	1986	0.107	99.553
1	7	2	1986	0.083	99.637
5	6	7	1986	0.069	99.706
7	2	1	1986	0.067	99.774
1	2	3	1986	0.058	99.832
1	6	2	1986	0.043	99.875
5	1	6	1986	0.034	99.910
2	1	5	1986	0.034	99.944
6	2	7	1986	0.032	99.976
2	5	3	1986	0.017	99.993
6	1	7	1986	0.006	100

Table 3.3 Angular observations and relative importance. In bold are the observations that account for more than 50% of the formal data importance.

Thus, the remaining angles were re-inverted, and resulting shear strain rates do not significantly differ with respect of the full dataset estimates (Table 3.4).

Shear strain rates (nanostrain/year) and Orientation of the most extensional strain (degrees)					
$\dot{\gamma}_1$	$\dot{\gamma}_2$	$\sigma_{\dot{\gamma}_1}$	$\sigma_{\dot{\gamma}_2}$	θ	σ_θ
113.89	-23.38	54.96	48.71	140.80	19.55
110.76	-37.26	65.52	74.74	144.30	28.71

Table 3.4 Inversion results. The first row indicates the full dataset inversion estimates, while the second row presents the inversion results taking in account the observations which cumulatively provide more than 50% of the formal data importance.

The main characteristic of the inversion solution is then the positive value of $\dot{\gamma}_1$ strain rate which corresponds to extension along x_1 direction, that is perpendicular to the trend of the Straits. This result, together with the small estimated value of $\dot{\gamma}_2$ strain rate suggests that the first-order strain field is dominated by extension in the direction perpendicular to the trend of the Straits (Figure 3.13), sustaining the hypothesis that the Messina Straits could represents an area of active concentrated deformation.

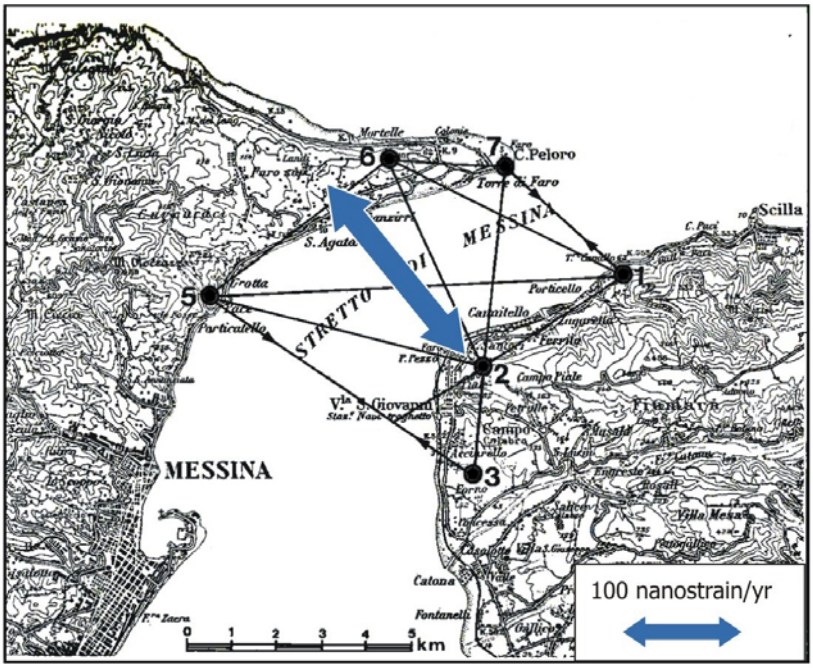

Figure 3.13 Total shear strain rate plotted along the direction of the principal axis of elongation.

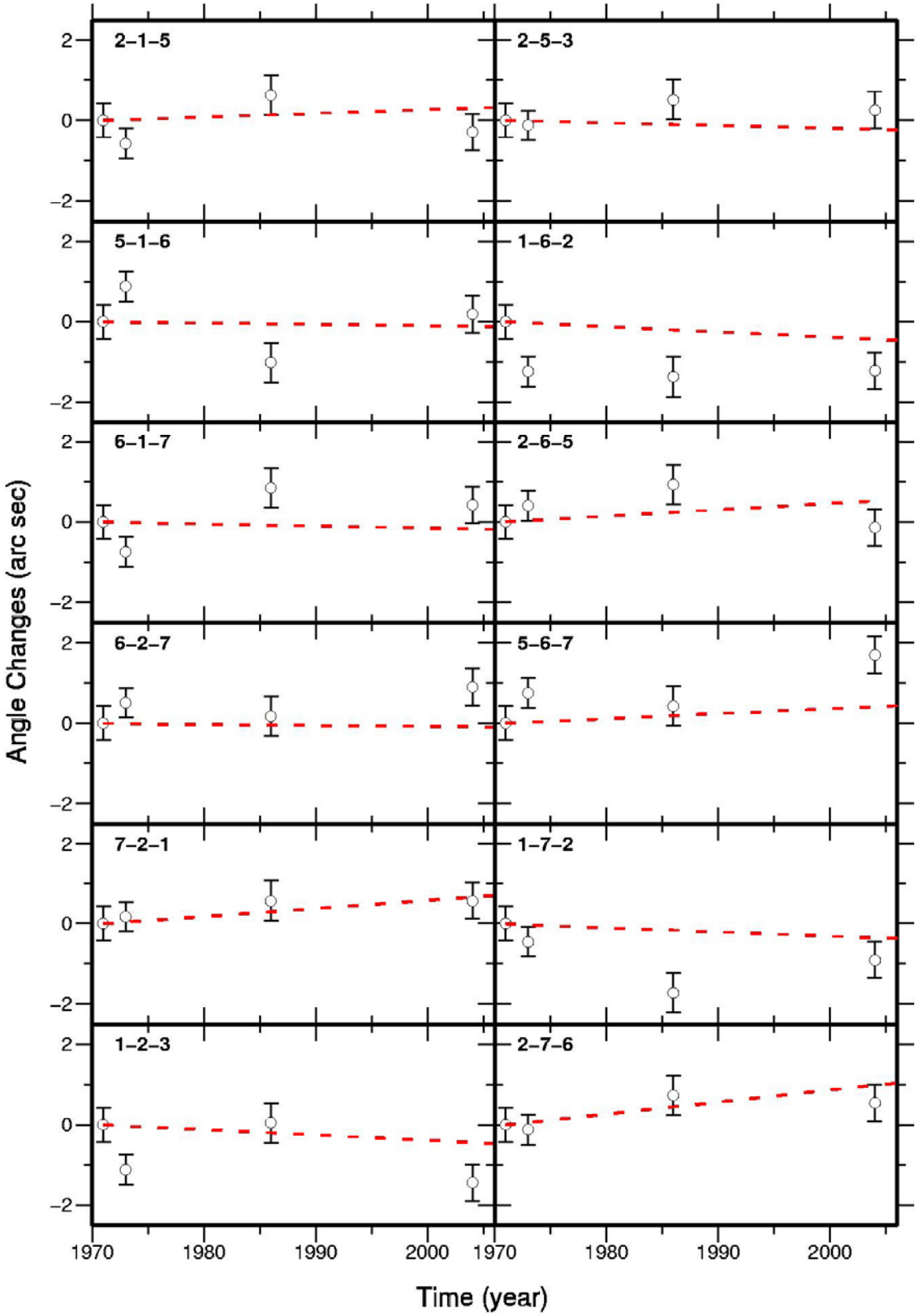

Figure 3.14 Angle changes measurements from 1971 to 2004. The white circles represent the observed angle changes at each epoch with the associate 1σ errors. The red dashed straight lines show the least-squares best-fitting model of $\dot{\gamma}_1$ and $\dot{\gamma}_2$.

3.6 Comparison with GPS[1] estimates of strain

The modern space-geodetic GPS technique represent a completely independent method to measure crustal motion (and hence strain accumulation) from the classical terrestrial measurements. Thus, GPS-based estimates of strain accumulation can be successfully used to compare and to validate the results previously achieved from the triangulation measurements. The considered GPS velocity field represent an update version of the GPS velocity solutions of *D'Agostino and Selvaggi* [*2004*] and consists of a combination of continuous site velocities with previous results from episodic campaign (Figure 3.15).

Continuous GPS measurements were analyzed using the Gipsy-Oasis II software. Nonfiducial satellite orbits, clock files and transformation parameters from free-network to ITRF2005 [*Altamini et al., 2007*] were imported from the NASA JPL (ftp.//sideshow.jpl.nasa.gov) [*Zumberge et al., 1997*]. The velocities uncertainties account for both white (non-correlated) and flicker noise (temporally correlated). The campaign episodic GPS velocity solutions are from the recent studies of *Hollenstein et al.* [*2003*] and of *Serpelloni et al.* [*2005*]. The different velocity solutions, nominally in the same Eurasian reference frame, are combined together by inverting with a weighted least-square algorithm, for the rigid rotation that minimizes the differences in velocity at the common stations, using the continuous GPS velocities as the reference solution.

GPS velocities projected perpendicular to the Messina Straits direction show that a sudden increase in velocity (≈ 3.5 mm/yr) occurs across the Straits (Figure 3.15b), corresponding to an average strain rate of ≈ 112 nanostrain/yr, indicating that active deformation is concentrated in the Messina Straits area. Both the magnitude and the orientation of the strain rate estimated by GPS observations are then consistent with independent triangulation estimates of strain (Figure 3.87), supporting the hypothesis that the Messina Straits can be an important boundary zone between Sicilian and Calabrian domains, currently accumulating deformation, that can be released in future earthquakes.

[1] The GPS velocity field was kindly provided by Dr. Nicola D'Agostino.

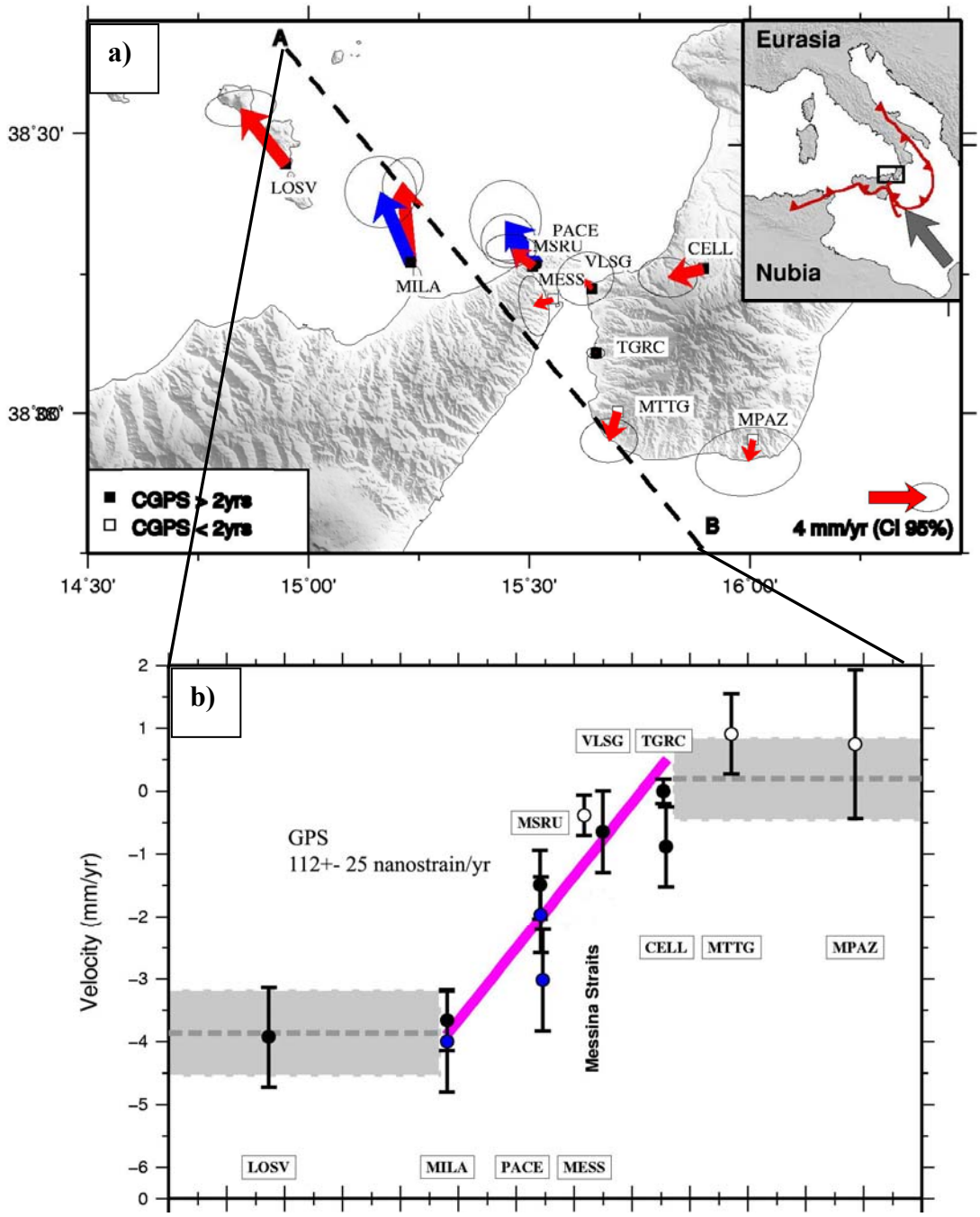

Figure 3.15 (a) CGPS velocity solution relative to the site TGRC and their 95% confidence ellipses. The GPS velocity field consists of a combination of permanent sites (red arrows) and survey-style sites (blue arrows). The inset shows the convergence vector between Eurasia and Nubia plates predicted by the GPS Eu-Nu pole of rotation. (b) Velocity in the N135°E direction as a function of distance along the same direction. The black circles indicate the continuous GPS velocity solutions with a time of observation > 2 yrs, while the white circles t < 2yrs. The error bars represent 1 standard deviation. The gray dashed lines mark the average velocity for the sites on the sides of the Messina Straits and the associated errors (gray area). The pink straight line represent the weighted linear regression of the GPS velocity solution.

3.7 Preliminary dislocation modelling

As already seen in paragraph 1.2, the strain accumulation observed during interseismic period has been successfully measured by means of geodetic observations of crustal motions and successfully modelled by means of simple elastic dislocation models [e.g., *D'Agostino et al., 2005*]. Due to the small number of GPS observations and to the poorly known three-dimensional geometry of the area, the follow dislocation modelling represents a preliminary study, in which the dislocation structure has been strongly simplified. That is, the observed horizontal displacements have been compared with the surface deformation accompanying slip on a two-dimensional planar dislocation locked above a given depth. The simplest 2-D model geometry includes only four parameters, the fault slip rate, the dip angle and the horizontal and vertical positions of the fault tip (locking depth).

In this paragraph, the horizontal displacements predicted by the two end-members of the several published seismological and geological models of the 1908 earthquake, are compared to observed geodetic displacements to attempt constraining the rate of interseismic loading and the geometry of the shear zone at depth. The two considered models can be schematically represented by means of two opposite dipping planar dislocation embedded in an elastic half-space [*Okada, 1985*]. The first source model can be schematically modelled by means of a SE-dipping surface dislocation locking below a certain depth (Figure 3.16), that is, the interseismic deformation is modelled by movement only below the locking depth by extending the dislocation to infinite depth. The second source model was indeed modelled by means of a NW-dipping shear zone (Figure 3.17). In this preliminary modelling no formal inversions have been made yet, nevertheless the tried forward models can still give some important information about the first-order characteristics of the shear zone at depth. As shown in Figure 3.16 and 3.17, both models predict horizontal surface displacements that are consistent with the observed displacement field and in particular the gradient of velocity across the Straits it is almost reproducible with both models. The major differences can be seen at the ends of the profiles, where anyway there are less observational constrains. Although these data sets do not precisely resolve the characteristic of the shear zone at depth, they can give some preliminary information about some model parameters. In fact, to reproduce the pattern of observed GPS velocities as well as the triangulation estimates of strain rate, it is necessary a locking depth that ranges between 4 and 10 km. The dip of the plane shear zone it not well constrained, varying between a large range of values. Obviously, there will be a well-known trade-off between the slip on the shear plane and the dip of the

plane. The overall extension rate is also poorly resolved because of the few GPS stations present at the end of the profile.

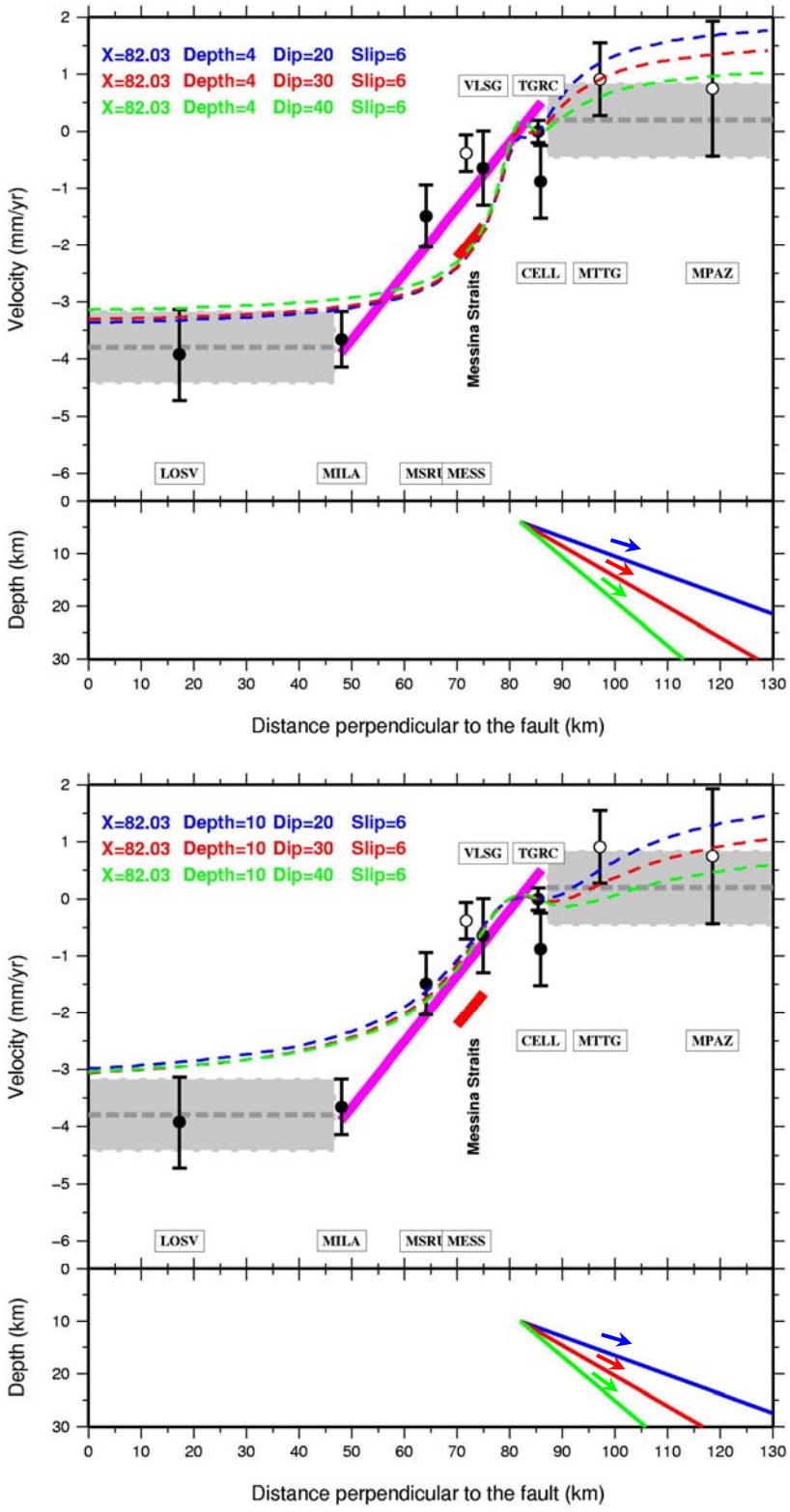

Figure 3.16 Comparison of observations (white and black circles with associated error bars) with predictions (dashed lines) for different dislocation models. The pink solid line represent the increment in velocity observed by the GPS measurements, while the red line is gradient velocity estimated by triangulation measurements. In the below box, the straight solid lines represent the interseismic model geometry.

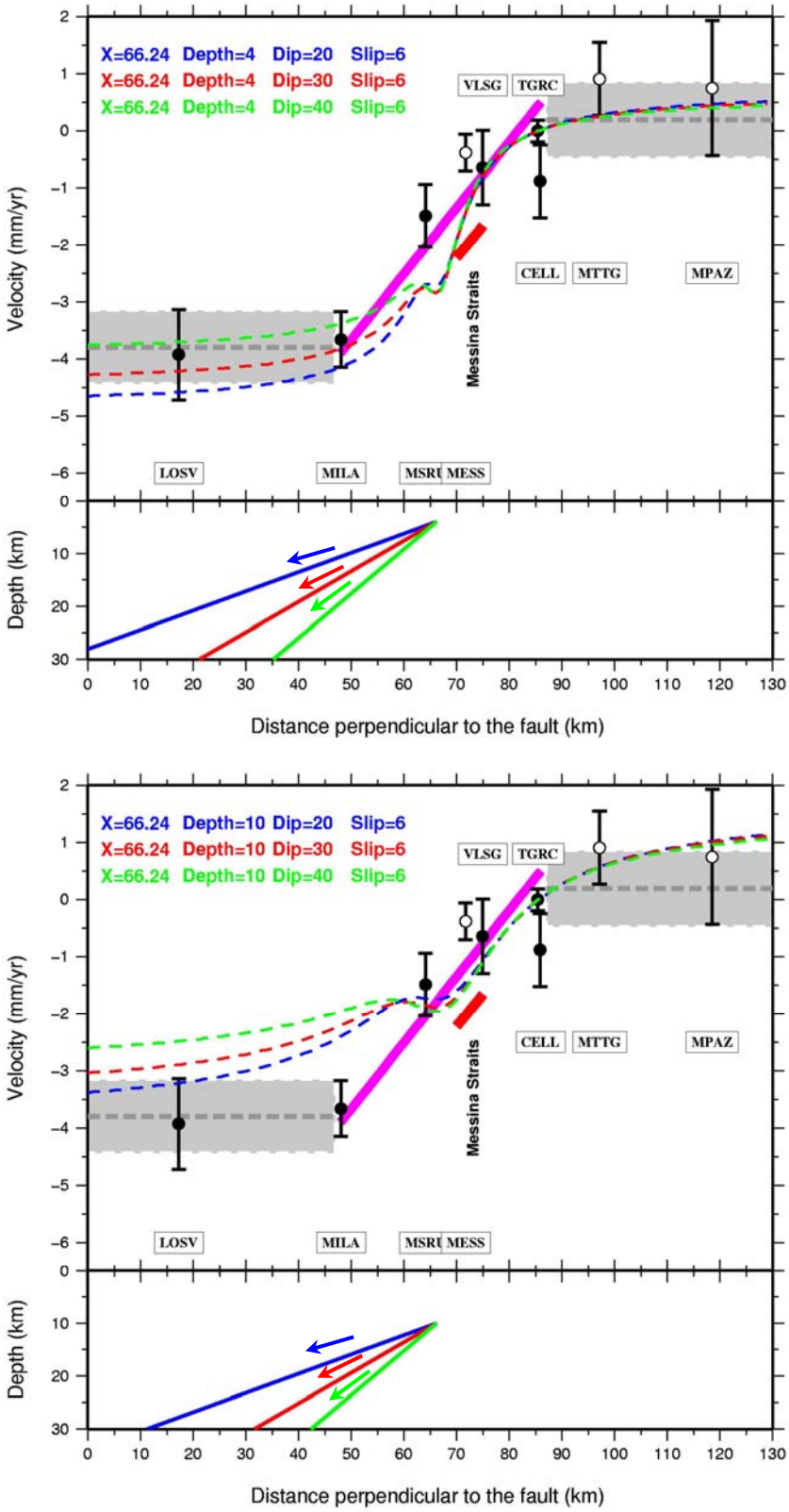

Figure 3.17 Comparison of observations (white and black circles with associated error bars) with predictions (dashed lines) for different dislocation models. The pink solid line represent the increment in velocity observed by the GPS measurements, while the red line is gradient velocity estimated by triangulation measurements. In the below box, the straight solid lines represent the interseismic model geometry.

3.8 Conclusions

In this Chapter we use data from repeated measurements of a ~ 6 km-wide triangulation network across the Messina Straits to determine rates of active crustal deformation over time span of 33 years. To determine the rates of deformation the observations were processed utilizing an extended version of the *Frank*'s method that permits to adjust all of the available observations simultaneously. The average annual shear strain rates for the time period between 1971 and 2004 are $\dot{\gamma}_1$ = 113.89 ± 54.96 nanostrain/yr and $\dot{\gamma}_2$ = -23.38 ± 48.71 nanostrain/yr, with the orientation of the most extensional strain (θ) at N140.80° ± 19.55°E, indicating that the triangulation measurements are consistent with an active NW-SE extension across the Messina Straits. The orientation of θ agree well with GPS deformation estimates, calculated over shorter time interval, and is consistent with previous preliminary GPS estimates [*D'Agostino and Selvaggi, 2004; Serpelloni et al., 2005*] and is also similar to the direction of the 1908 (M_W 7.1) earthquake slip vector [e.g., *Boschi et al., 1989; Valensise and Pantosti, 1992; Pino et al., 2000; Amoruso et al., 2002*]. We infer that the measured strain rate is due to active extension across the Messina Straits, corresponding to a relative extension rate ranges between < 1mm/yr and up to ~ 2 mm/yr, within the portion of the Straits covered by the triangulation network. These results are consistent with the hypothesis that the Messina Straits is an important active geological boundary between the Sicilian and the Calabrian domains and support previous preliminary GPS-based estimates of strain rates across the Straits, which show that the active deformation is distributed along a greater area. Finally, the preliminary dislocation modelling has shown that, although the current geodetic measurements do not resolve the geometry of the dislocation models, they solve well the rate of interseismic strain accumulation across the Messina Straits and give useful information about the locking the depth of the shear zone.

The forthcoming CGPS measurements that will come from the densification of the permanent GPS network in southern Italy as well as further observations of the existing GPS stations, will be needed to provide more detailed information about active deformation in the Messina Straits area, that have significant implications for the seismic hazard.

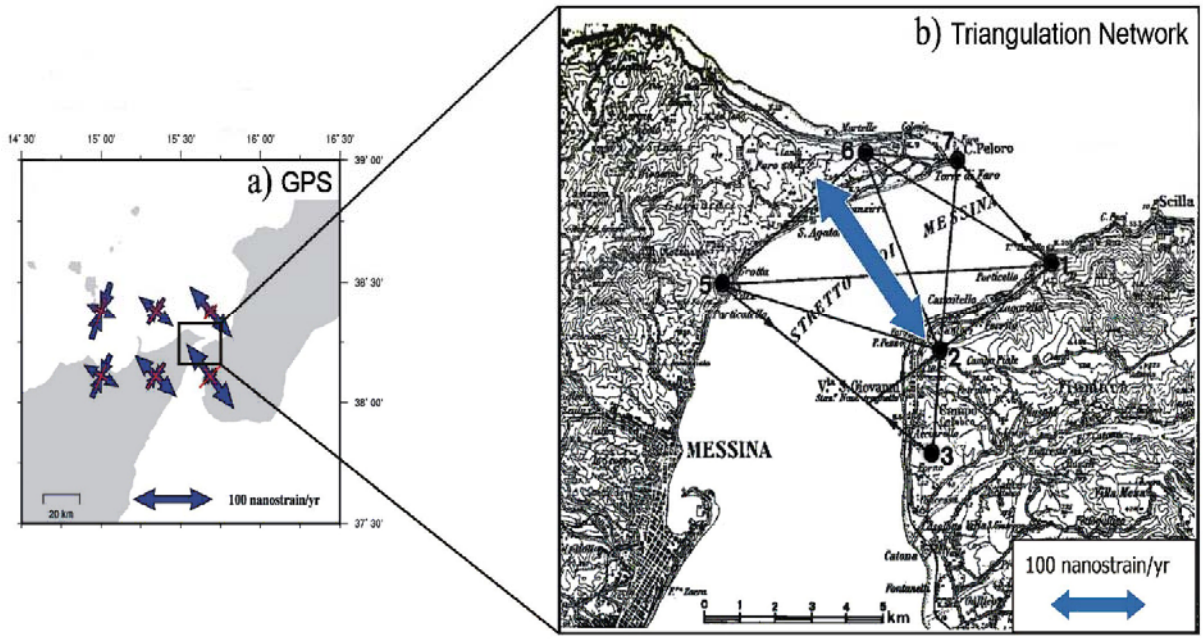

Figure 3.18 (a) Principal axes of the horizontal strain rate tensor (in blue) and associated 1 sigma errors (in red), from *D'Agostino and Selvaggi* [*2004*]. (b) Triangulation network and the direction of the most extensional direction of the strain tensor. Double arrow length is proportional to $\gamma_{tot}=\sqrt{\gamma^2_1+\gamma^2_2}$ from triangulation measurements.

Chapter IV

Inversion of Geodetic Data for Estimates of Source Parameters

4.1 Introduction

The increasingly widespread use of space geodesy has resulted in numerous high-quality surface deformation data sets, and these data can provide important constraints on fault geometry and slip distribution [*Cervelli et al., 2001*]. In addition to these space geodetic measurements, conventional geodetic data can also provide detailed information on ground displacements near faults that helps us understand how faults move during an earthquake, constraining certain fault properties. In fact, repeated surveys of geodetic networks have been successfully measured coseismic displacements in several cases by terrestrial measurements [e.g. *Lin & Stein, 1989; Arnadottir & Segall, 1994; Yu & Segall, 1996; Thatcher et al., 1997; King & Thatcher, 1998; Bilham & England, 2001; Pollitz et al., 2005; Nyst et al., 2006*]. In such analysis a popular model for fault behaviour is an elastic dislocation embedded in an elastic crust. In this chapter, after an overview about how the physical model of fault behaviour can be described, the principal methods for rigorously inverting surface deformation fields for source type and geometry from geodetic measurements are presented.

4.2 The elastic half-space model

Estimating source geometry from geodetic data requires a forward model of how the crust responds to various kind of deformation sources. The most common used crustal model is the homogeneous, isotropic, linear, elastic half-space proposed by *Okada* [1985]. Accordingly, the displacement field $u_i(x_1, x_2, x_3)$ due to a dislocation $\Delta u_j(\xi_1, \xi_2, \xi_3)$ across a surface Σ in an isotropic medium is:

$$u_i = \frac{1}{F} \iint_{\Sigma} \Delta u_j \left[\lambda \delta_{jk} \frac{\partial u_i^n}{\partial \xi_n} + \mu \left(\frac{\partial u_i^j}{\partial \xi_k} + \frac{\partial u_i^k}{\partial \xi_j} \right) v_k \right] d\Sigma \qquad (4.2.1)$$

where δ_{jk} is the Kronecker delta, λ and μ are Lame's coefficients (these parameters specify the elastic medium), v_k is the direction cosine of the normal to the surface element $d\Sigma$, and the summation convention applies. u_i^j is the ithcomponent of the displacement at (x_1, x_2, x_3) due to the *j*th direction point force of magnitude *F* at (ξ_1, ξ_2, ξ_3).

Accordingly with this model, a fault is represented by a rectangular dislocation, with uniform slip, embedded in a homogeneous, isotropic, elastic half-space. This dislocation is defined by nine model parameters that describe the geometry and the slip of the fault plane: longitude and latitude of a corner of the fault plane (x_0, y_0), length (L), width (W), strike (ϕ), dip (δ) and depth (z_0) of the upper edge of the fault plane, and magnitude and rake of the slip vector (U_1, U_2) (Figure 4.1). In spite of its limitations, the elastic half-space model is widely used primarily because of the simplicity of the expressions for the surface deformation caused by uniform, rectangular dislocations and point sources. Moreover, until recently, most geodetic data were not of sufficiently high quality to justify more complex crustal models.

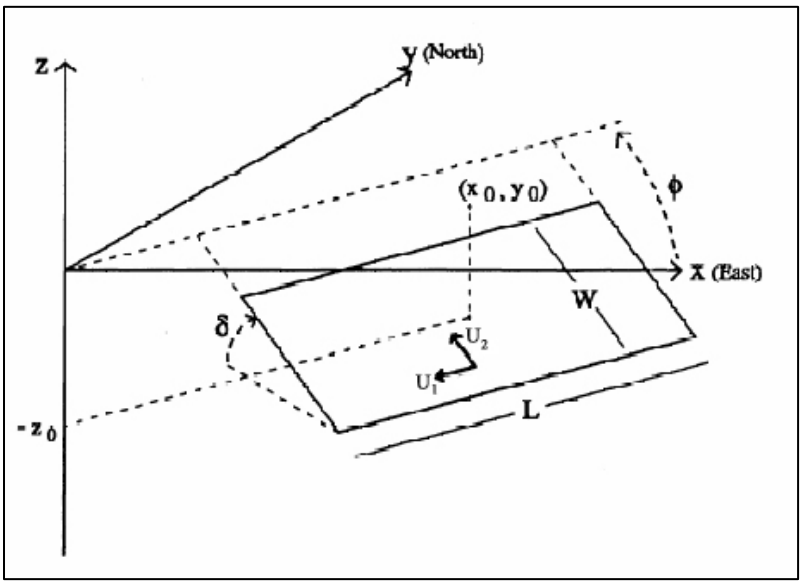

Figure 4.1 Geometry of the source model: considering a Cartesian coordinate system, elastic medium occupies the region of $z \leq 0$ and x axis is taken to be parallel to the strike direction of the fault. Further, the elementary dislocations U_1, U_2 and U_3 are defined so as to correspond to strike-slip, dip-slip, and tensile components of arbitrary dislocation. Each vector represents the movement of hanging-wall side block relative to foot-wall side block Modified from *Arnadottir and Segall* [1994].

4.3 Inversion for source parameters

Dislocation modeling is an example of a more general class of geophysical inversion techniques in which observations of surface motion are compared to predictions derived from an assumed physical model of crustal or fault behavior. In this context, geophysical inversion involves finding an optimal value of a function of several variables. The function to minimize is a misfit (or fitness) function that characterizes the differences (residuals) between observed and synthetic data calculated by using an assumed earth model.

The relationship between the deformation field and the source geometry can be expressed by the observation equation:

$$\mathbf{d} = \mathbf{G}(\mathbf{m}) + e \tag{4.3.1}$$

where **d** is the deformation data vector, **m** is the source geometry vector, **G** is the function that relates the two and *e* is a vector of observation errors. A common method to solve this inverse problem is the method of least-squares (see paragraph 2.4). However, for the source geometry estimation problem the data are related nonlinearly to the source parameters. Because analytic methods of least-squares fitting cannot be used for nonlinear fitting problems, approximation methods and searches of parameter space must be considered. For this reason, source optimization reduces to nonlinear optimization [*Cervelli et al., 2001*].

The optimal source model, $\mathbf{m}^{est}$, will minimize the misfit between observation and prediction. A common convention to quantify the misfit is the use of the weighted residual sum of squares, which can be normalized by the number of individual data, minus the number of estimated parameters (MSE, mean square error):

$$MSE = \frac{r^T \sum^{-1} r}{n - p} \tag{4.3.2}$$

where $r = d - G(m)$, $\sum$ is the data covariance, n the number of data and p the number of model parameters. For linear fitting problems, the method of least-squares can be used for determining the optimal values of the parameters that yield a minimum for the misfit function (see paragraph 2.4). For nonlinear fitting problems, the minimization must proceeded iteratively. In this case, several robust methods have been developed for finding this

minimum value and so that rigorously inverting surface deformation fields for source type and geometry:

- Derivative-based algorithms [e.g. *Arnadottir et al., 1992; Murray et al., 1996; Jonsson et al., 1999; Aoki et al., 1999*];

- Exhaustive and random searches [e.g. *Ward and Barrientos, 1986; Marshall et al., 1991; Nyst et al., 2006*];

- Monte Carlo algorithms: e.g., simulated annealing [*Metropolis et al., 1953*], random cost [*Berg, 1993*], neighbourhood [*Sambridge, 1999*] and genetic algorithms [*Holland, 1975*].

Derivative-based algorithms offer the most straightforward and efficient approach to solving this optimization problem [*Gill et al., 1981*]. However, due to their depending on the gradient and higher-order derivatives to guide them through misfit space, these kind of algorithms can get trapped in local minima and then never find the global minimum. A consequence of this fact, it is that these algorithms strongly depend on the initial guess and so they work well only when the initial guess is near the global minimum.

The second class of algorithms (exhaustive and random searches) are based on the discretization of the misfit space and the subsequently searching through the resulting grid. So that, these type of algorithms do not suffer the problem of local minima. However, because the number of possible combinations increases exponentially with the number of estimated parameters, exhaustive searches are viable only when the number of parameters remains small.

The last class of algorithms combined the efficiency of a derivative-based method with robustness of a random search. In fact, the common feature of all Monte Carlo class of algorithms is an element of randomness that permits an occasional uphill move that permits they to escape local minima, that is, the algorithms will not always move from a candidate model with higher misfit to a model with lower misfit. In the following sections, three different nonlinear fitting methods that have been used in this Thesis are presented.

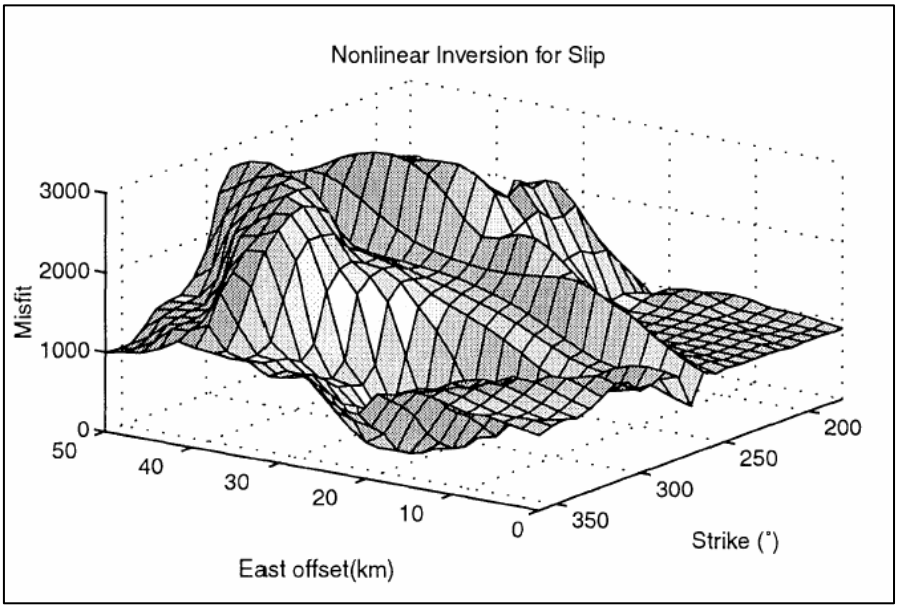

Figure 4.2 Misfit space depicted in three dimensions, i.e., misfit as function of two model parameters. Note that the space is highly complicated and characterized by multiple hills and valleys, that is, containing multiple minima. From *Cervelli* [2001].

4.3.1 Exhaustive searches

In computer science, exhaustive search or "brute-force" search is a trivial but very general problem-solving technique, that consists of systematically enumerating all possible candidates for the solution and checking whether each candidate satisfies the problem's statement. Then this method involves discretizing the misfit space and then searching exhaustively through the resulting grid. Its cost is proportional to the number of candidate solutions, which, in many practical problems, tends to grow very quickly as the size of the problem increases. In fact, the number of possible combinations equals Q^p, where Q is the number of divisions in the grid and p is the number of parameters [*Cervelli et al., 2001*]. So that, grid-search methods are viable only when the number of model parameters stays small. For this reason, use of grid search methods for most geophysical applications, for which the model space is very large and the forward calculation is slow, is far from being practical. However, exhaustive search is simple to implement, and will always find a solution if it exists, and therefore this type of technique has been successfully used [e.g., *Walter, 1993; Zhao and Helmberger, 1994; D'Agostino et al., 2005; Nyst et al., 2005*].

4.3.2 Monte Carlo algorithms

Monte Carlo methods are pure random search methods in which models are drawn uniformly at random and tested against the data [*Sen and Stoffa, 1995*]. That is, a Monte Carlo algorithm is a computational algorithm which relies on repeated random sampling to compute its results. Monte Carlo methods tend to be used when it is infeasible or impossible to compute an exact result with a deterministic algorithm. This class of searching algorithms combines the efficiency of a derivative-based method with the robustness of a random search. Every Monte Carlo algorithms has an element of randomness that permits an occasional uphill move and then to escape local minima.

In a Monte Carlo inversion, each model parameter is allowed to vary within a predefined search interval (determined a priori). Thus for each model parameter m_i:

$$m_i^{\min} \leq m_i \leq m_i^{\max} \tag{4.3.3}$$

Synthetic data are then generated for the new model and compared with observations. The model is accepted deterministically based on an acceptance criterion which determines how well the synthetic data compare with the observations. The generation-acceptance/rejection process is repeated until a stopping criterion is satisfied.

In this Thesis, two different Monte Carlo class of algorithms have been tested and used: a genetic algorithm and a simulated annealing algorithm.

4.3.2.1 Genetic algorithms

A *genetic algorithm* (GA) is a stochastic global search method used in computing to find exact or approximate solutions to optimization and search problems, that is, capable of near-optimal solutions for multivariable functions. That is, GA's are used to solve highly non-linear and non-local optimization problems. These type of algorithms were first proposed by *Holland* [*1975*], based on analogies with the process of biological evolution. Thus, a genetic algorithm works by mimicking the process of natural selection population's evolution according to the natural selection principle of survival of the fittest. By analogy with the natural behavior, each model parameters correspond to a gene and all of the coded model parameters are joined together into a long bit string, analogous to a chromosome, which

represents the genetic information of each individual (model), which will be modified by the algorithm. Typically, the algorithm starts with an initial population of individuals chosen at random from the discrete model space, each representing a possible solution. The forward problem is then solved and a fitness score is assigned to each individual. That is, in each generation, the fitness of every individual in the population is evaluated. Individuals with higher fitness are given more opportunities to "crossbreed" with others in the population to produce "offspring" that form a new population the same size as the original. The algorithm iterates by taking those offspring as a new generation and repeats the process until a satisfactory solution is obtained, without dependence on initial model. Commonly, the algorithm terminates when either a maximum number of generations has been produced, or a satisfactory fitness level has been reached for the population. That is, GA only requires the knowledge of the limits of the model parameters within the search space that includes the solution.

The specific genetic algorithm used in this Thesis implements the genetic global optimization algorithm used, e.g., in *Bagh et al.* [*2007*]. The basic steps in this GA are then initialization, selection, crossover and mutation. Initially many individuals solutions (models) are randomly generated to form an initial population. The population size depends on the nature of the problem, but typically contains several hundreds of possible solution. The population is generated randomly, covering the entire range of the user-defined space solutions. During each successive generation, a proportion of the existing population is selected to breed a new generation. Individual solutions are selected through a fitness-based process, where fitter solutions (as measured by a user-defined fitness function) are typically more likely to be selected. Once the models are selected and paired, the next step is to generate a second generation population of solutions from those selected through genetic operators (crossover and mutation). The genetic operator of crossover is the mechanism that allows genetic information between the paired models to be shared, i.e., crossover causes the exchange of some information between the paired models, thereby generating new pairs of models. Mutation is the random alteration of a bit. Generally the average fitness will have increased by this procedure for the population, since only the best "organism" from the first generation are selected for breeding, along with a small proportion of less fit solutions. This generational process is repeated until a termination condition has been reached. In particular, the termination conditions of the GA used in this Thesis, are based on a threshold misfit value and a fixed number of generations reached.

Recently the GA (introduced to geophysics by *Stoffa and Sen* [*1991*]) has been applied to geophysical problems such as velocity structure estimation [e.g *Chang et al., 2004; Bagh et al., 2007*], hypocentral parameters [e.g. *Kim et al., 2006*] and seismic source rupture modeling of fault plane [e.g. *Zeng and Anderson, 1996*].

4.3.2.2 Simulated annealing

Among nonlinear geophysical inversion methods, *simulated annealin*g (SA) is one of the most used global optimization algorithms. In fact, SA has been successfully used in many geophysical inverse problems [e.g. *Rothman, 1985, 1986; Basu and Frazer, 1990; Sen and Stoffa, 1991; Amoruso et al., 1998; Aoki et al., 1999*]. Simulated annealing is a generic probabilistic algorithm for the global optimization problem, namely locating a good approximation to the global minimum of a given function in a larger space. The name and inspiration come from annealing in metallurgy, a technique involving heating and controlled cooling of a material to increase the size of its crystals and reduce their defects. The heat causes the atoms to become unstuck from their initial positions (a local minimum of the internal energy) and wander randomly through states of higher energy; the slow cooling gives them more changes of finding configurations with lower internal energy than the initial one. *Metropolis et al.* [*1953*] first incorporated these kinds of principles into numerical calculations.

In simulated annealing, the likelihood of choosing a lower misfit model over a higher one depends not only in the misfit difference between the two but also on the state of annealing process at the time of the choice. In fact, by analogy with this physical process, each step of the SA algorithm replaces the current solution by a random "nearby" solution, chosen with a probability that depends on the difference between the corresponding function misfit values and on a global parameter T (called temperature), that is gradually decreased during the process. The dependency is such that at high temperatures all models have roughly equal chances of getting picked (the algorithm essentially functions as a random search), while at low temperatures the algorithm favors low misfit models (Figure 4.3), that is, in the final stages of annealing, the probabilities associated with low misfit become very high, making uphill moves extremely unlikely.

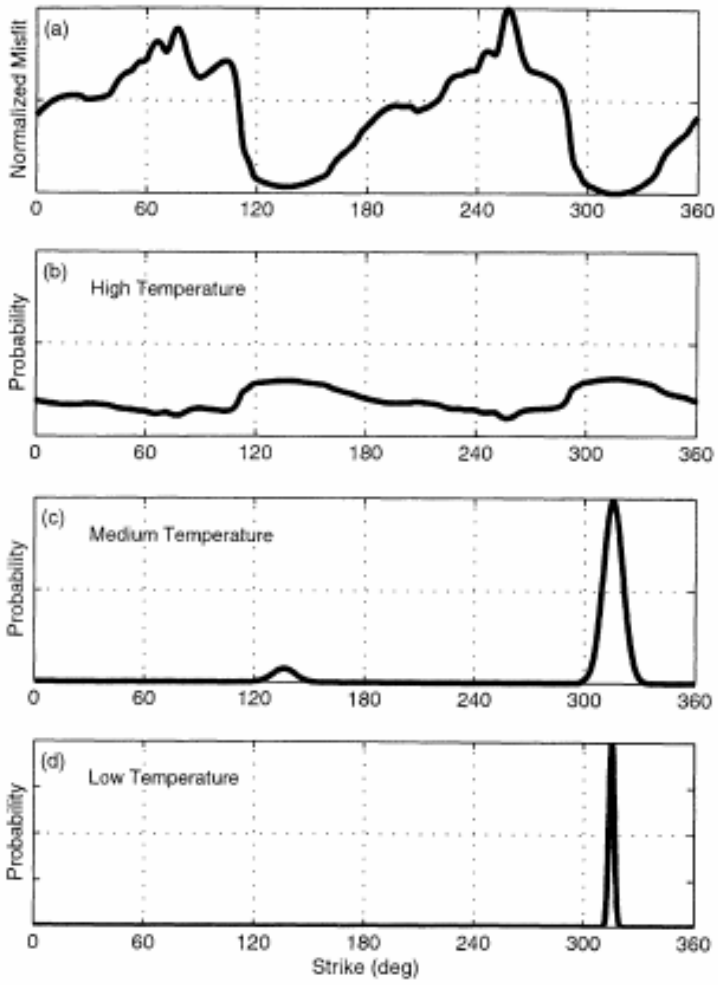

Figure 4.3 Probability density function for simulated annealing at three different temperatures. (a) Misfit as a function of a single model parameter. Corresponding probability density function at high (b), medium (c) and low (d) temperature. Note that at high temperature the density function is quite flat and lower misfit models are only slightly more favored than higher misfit models, whereas at low temperatures, the parameter value that minimizes the misfit becomes overwhelmingly probable. From *Cervelli* [2001].

During the annealing process, the temperature lowers according to a "cooling schedule". The most significant complication to the simulated annealing algorithm is then the cooling schedule, i.e., how the temperature changes as the annealing progresses. A cooling schedule includes the starting temperature, T_0, the rate of cooling, the amount of time to be spent at each temperature, and the time at which to stop [*Basu and Frazer, 1990*].

The specific annealing algorithm used in this Thesis implements the continuous simulated annealing global optimization algorithm described in *Corana et al.* [*1987*] and *Goffe et al.* [*1994*]. It proceeds as follows (Figure 4.4). SA tries to find the global minimum (or maximum) of a N dimensional function, moving both up and downhill and as the optimization

process proceeds, it focuses on the most promising area. To start, it randomly chooses a trial point (*X'*) within the step length (*VM* a vector of length *N*, i.e., the step length over which the algorithm searches for minima) of the user selected starting point (X_0). The function is evaluated at this trial point (*f'*) and its value is compared to its value at the initial point (*f*). If the value (*f'*) of the function is greater than *f*, the point *X'* is accepted and the algorithm moves downhill. In a minimization problem, all downhill moves are accepted and the algorithm continues from that trial point. Uphill moves may be accepted, in fact, if *f'* is greater or equal to *f*, the *Metropolis* [*1953*] criteria decides on acceptance. It uses *T* (temperature) and the size of the uphill move in a probabilistic manner. The value:

$$p = e^{\left(\frac{f'-f}{T}\right)} \tag{4.3.4}$$

is computed and compared to *p'*, a uniformly distributed random number from (0,1). If *p* is greater than *p'*, the new point is accepted and the algorithm moves uphill. Two factors decrease the probability of a uphill move: lower temperatures and larger differences in the function's value. Furthermore, the decision on uphill moves contains a random element.

If the trial is rejected, another point is chosen instead for a trial evaluation. Each element of *VM* periodically adjusted so that half of all function evaluations in that direction are accepted. A fall in *T* is imposed upon the system with the temperature reduction factor (*RT*) variable by:

$$T(i+1) = RT * T(i) \tag{4.3.5}$$

where *i* is the *i*th iteration. Thus, as *T* declines, uphill moves are less likely to be accepted and the percentage of rejections rise. Given the scheme for the selection for *VM*, *VM* falls. Thus, as *T* declines, *VM* falls and SA focuses upon the most promising area for optimization.

The parameter *T* is then crucial in using SA successfully, because it influences *VM*, the step length over which the algorithm searches for minima. In fact, for a small initial *T*, the step length may be too small and thus not enough of the function might be evaluated to find the global minimum. To determine the starting temperature that is consistent with optimizing a function, it is then worthwhile to run some trial runs first. As it is well described later, the parameters *T* and *RT* used in the applications, were principally taken from *Corana et al.* [*1987*] and from *Goffe et al.* [1994].

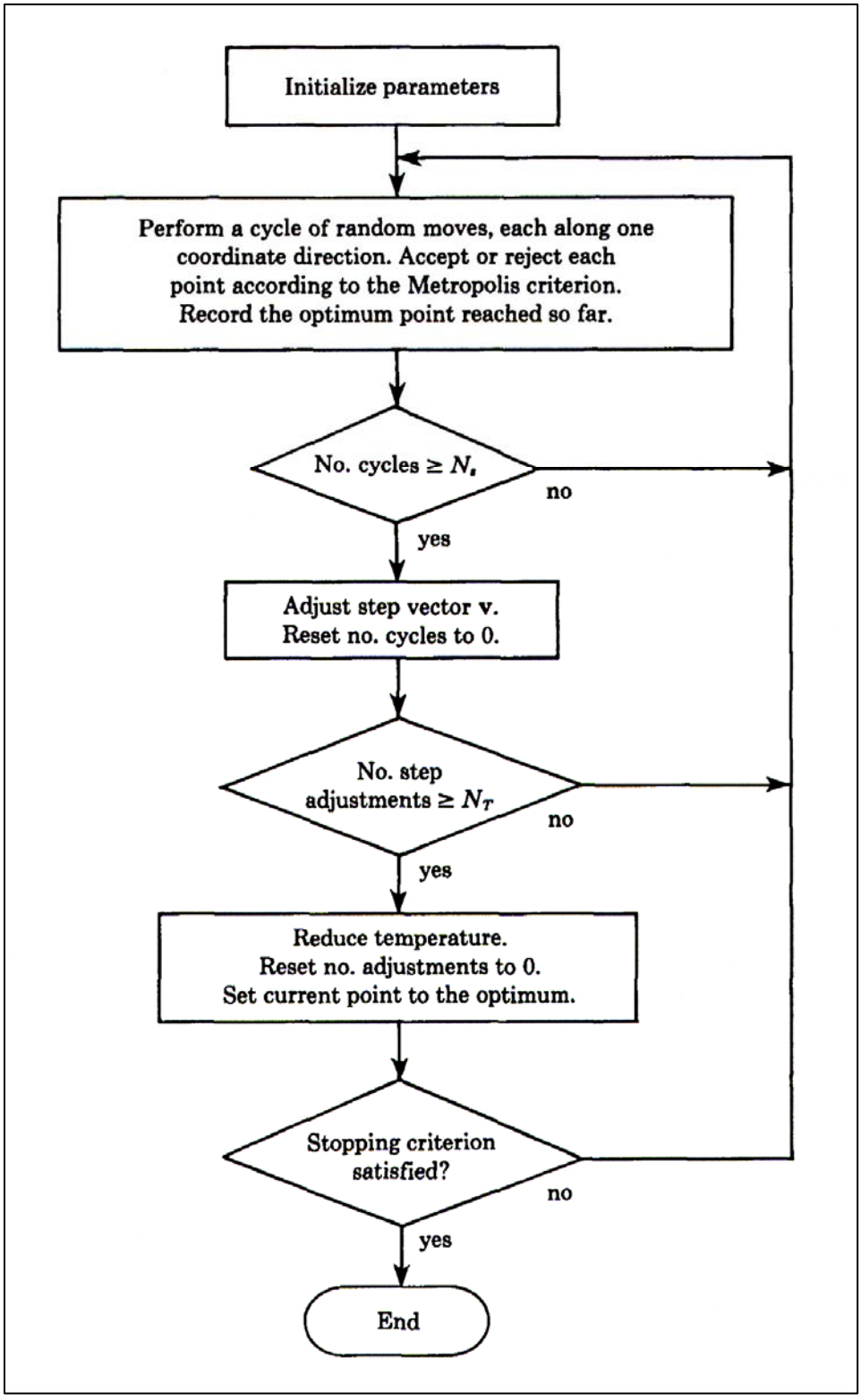

Figure 4.4 A conceptual scheme of the simulated annealing (SA) minimization algorithm. Modified from *Corana et al.* [1987].

4.4 Uncertainties in nonlinear models

Assessing confidence intervals associated with estimated source parameters remains an important problem in geophysical inversion problems. In fact, to assess how well the model is constrained by the data, it is important to estimate confidence intervals for the model parameters. This problem is not a straightforward procedure when the model is a nonlinear function of the data. In general, confidence regions will be much more complex and much harder to assess with respect to linear cases where noise follows a Gaussian probability distribution. In reality, noise accounts for only part of the difference between parameter estimates and their actual values, and then the distinction between uncertainties about source model parameters and uncertainties about the model itself must be kept clear [*Cervelli et al., 2001*].

Following *Press* [*1992*], a conceptual scheme of an experiment that measures a set of *M* parameters (**a**) is represented in Figure 4.5.

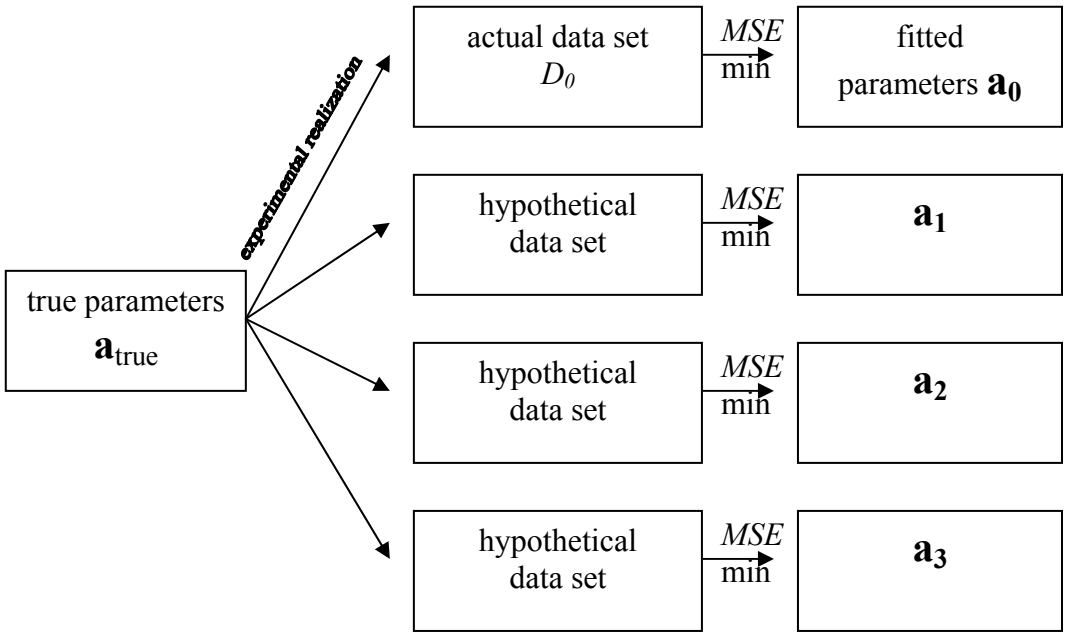

Figure 4.5 A conceptual scheme of an experiment. True parameters $\mathbf{a}_{true}$ are realized in a data set, from which fitted (observed) parameters $\mathbf{a}_0$ are obtained. If the experiment were repeated many times, new data sets and new values of the fitted parameters would be obtained. Modified from *Press* [1992].

In general, in an experimenter, there is some underlying true set of parameters, $\mathbf{a}_{true}$, that are unknown from the experimenter. These true parameters are statistically realized, along with some random measurements errors, as a measured data set, D_0, and obviously this data set is known to the experimenter. The goal is to fit the measured data to a model by minimization of the misfit or some other technique, and then obtain fitted values for the parameters of the model, $\mathbf{a}_0$. Because measurement errors have a random component, the measured data set, D_0, is not a unique realization of the true (unknown) parameters, $\mathbf{a}_{true}$. Rather, there are infinitely many other realizations of the true parameters as "*hypothetical data sets*" (D_1, D_2, …) each of which could have been the one measured, but happened not to be. Each one, had it been realized, would have given a slightly different set of fitted parameters, $\mathbf{a}_1$, $\mathbf{a}_2$, …, respectively. These parameter sets, $\mathbf{a}_i$, therefore occur with some probability distribution in the p-dimensional space of all possible parameter sets, $\mathbf{a}$. The actual measured set, $\mathbf{a}_0$, is one member drawn form this distribution. If the distribution of the difference $\mathbf{a}_i - \mathbf{a}_{true}$ were known, one would know everything that there is to know about the quantitative uncertainties in the experimental measurement $\mathbf{a}_0$. So the problem is to find some way of estimating or approximating the probability distribution $\mathbf{a}_i - \mathbf{a}_{true}$ without knowing $\mathbf{a}_{true}$ and without having available infinite hypothetical data sets.

Two are the principal methods that have been developed to estimate the individual confidence limits on estimated model parameters from the data itself: the Monte Carlo simulation technique and the Bootstrap method. Both are modern, computer-intensive, general purpose approaches to statistical inference, falling within a broader class of resampling methods.

4.4.1 Monte Carlo simulation technique

The a posteriori uncertainty associated with each parameter estimate can be calculated by a *Monte Carlo simulation technique* (Figure 4.6) [*Press et al., 1992*]. The base of this method is the consideration that the shape of the probability distribution $\mathbf{a}_i - \mathbf{a}_0$ can be nearly the same as the shape of the probability distribution $\mathbf{a}_i - \mathbf{a}_{true}$. In this way, the only assumption made is that the way in which random errors enter the experiment and data analysis does not vary rapidly as a function of $\mathbf{a}_{true}$, so that $\mathbf{a}_0$ can be considered as a reasonable surrogate, i.e., the fitted parameters from an actual experiment are used as surrogates for the true parameters. The procedure to generate multiple synthetic (modified) data sets (D^S_1, D^S_2, ...), is to draw

(computer-generated) random numbers from appropriate distributions so as to mimic measurements errors and then adding these synthetic realizations of data noise to the original data. Then for each modified data sets, D^S_j, exactly the same procedure for estimation of parameters, e.g., misfit minimization, as was performed on the actual data (to get parameters $\mathbf{a}_0$) is performed, giving simulated measured parameters, $\mathbf{a}^S_1$, $\mathbf{a}^S_1$, … . The distribution of these fitted parameters around the (known) surrogate true parameters, $\mathbf{a}_0$, is thus studied to map out the desired probability distribution in p dimensions, i.e., the results of many optimization runs using these modified input data provide a distribution of models which outline the confidence intervals of the optimum source model parameters. This method has been successfully used in many source estimation problems [e.g., *Feigl et al., 1995; Wright et al., 1999; Sudhaus and Jonsson, 2007*].

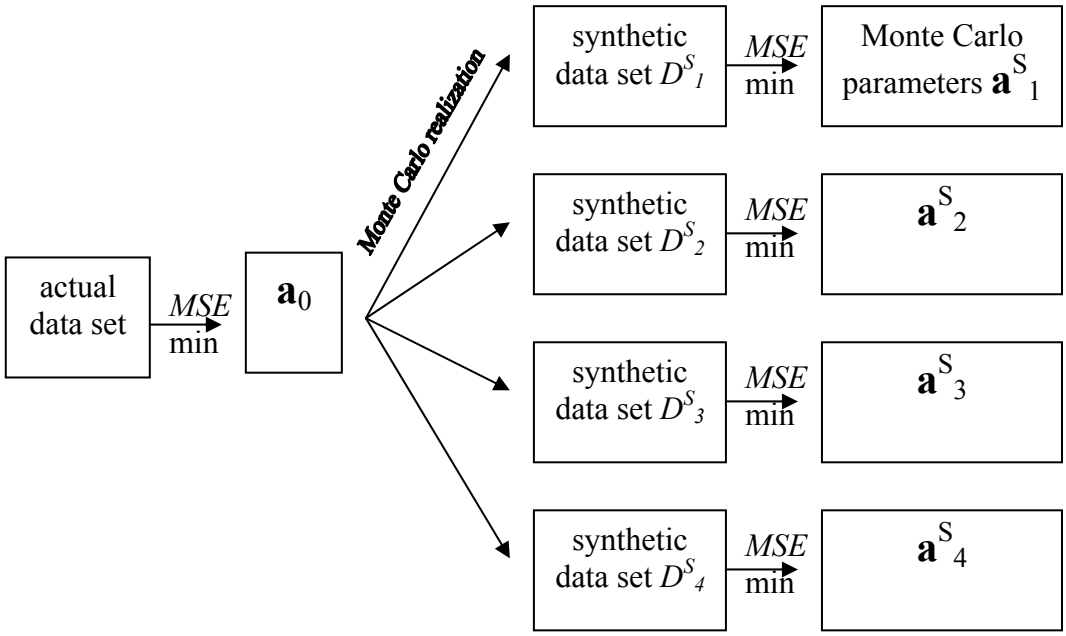

Figure 4.6 Monte Carlo simulation of an experiment. Computer-generated random numbers are used to simulate many synthetic data sets, and each of these is analyzed to obtain its fitted parameters. The distribution of these fitted parameters around the surrogate parameters is thus studied. Modified from *Press* [1992].

4.4.2 The bootstrap method

The *bootstrap method* [*Arnadottir et al., 1992; Efron and Tibshirani, 1993*], builds confidence intervals by randomly resampling from the data, with replacement (i.e., a particular datum can be resampled more than once, others not at all). That is, this technique uses actual data set, D_0, with its n data points, to generate any number of synthetic data sets,

D^S_1, D^S_2, …, also with n data points. The procedure is simply to draw n data points at a time with replacement from the set D_0. Due to the replacement, each modified data sets is composed by a random fraction of the original points (typically ≈ 37%) that are replaced by duplicated original points. As in the Monte Carlo simulation technique, these modified data sets are subjected to the same estimation procedure as was performed on the original data, giving a set of simulated measured parameters $\mathbf{a}^S_1$, $\mathbf{a}^S_1$, … . Again, the distribution of these parameters is used to make inference about errors of model estimated parameters. The distribution obtained is the bootstrapped estimate of the sampling distribution. Thus, the basic steps in the bootstrap procedure are:

- from the empirical distribution function, draw a random resample of size n from the original sample (of size n either) with replacement;

- calculate the statistic of interest for this resample;

- repeat steps 1 and 2 B times, where B is a large number, in order to create B resamples (typically, B is at least equal to 1000 when an estimate of confidence interval around the statistic of interest is required);

- construct the relative frequency histogram from the B number of the statistic of interest, obtained from the B resamples; the distribution obtained is the bootstrap estimate if the sampling distribution of the statistic of interest.

For a large class of problems the bootstrap thus does yield easy estimated of the errors in an estimated parameter set [e.g., *Cervelli et al., 2001*]. However, bootstrapping does not overcome the weakness of small samples as basis for inference. In fact, some estimators of **a**, might be particularly sensitive to all the points be present and in that case, the bootstrap is going to give wrong distribution. Even if other bootstrap procedures (e.g., the bootstrap bias-corrected accelerated method, the bootstrap tilting interval method) more accurate than standard methods have been formulated, they may not be accurate for very small samples, that is, bootstrap inference from a small sample may therefore be unreliable [*Hesterberg et al., 2006*].

4.5 Simultaneous inversion for source geometry and variable slip

Most deformation models, including source model, have at least one parameter that is linearly related to the deformation field (e.g., the slip). Then, for a given set of the remaining nonlinear parameters it is possible to solve, using conventional least-squares, for the optimal values of the linear parameters, that is, projecting the linear parameters out of the misfit space [*Cervelli et al., 2001*]. The advantage is that, implicitly solving for the linear parameters at each iterations, it reduces the dimension of the misfit space and this should increase optimization efficiency. However, the effect of projecting the linear parameters out of the optimization problem is to flatten the misfit space (Figure 4.6), which degrades the performance of Monte Carlo algorithms. Further, *Cervelli at al.* [*2001*] state that when the Monte Carlo algorithms operate on all the parameters, linear parameters included, it is no less efficient than separate linear inversion and that for source inversion problems, in several cases the Monte Carlo algorithms more consistently converge to the global minimum when they are permitted to operate over all the parameters.

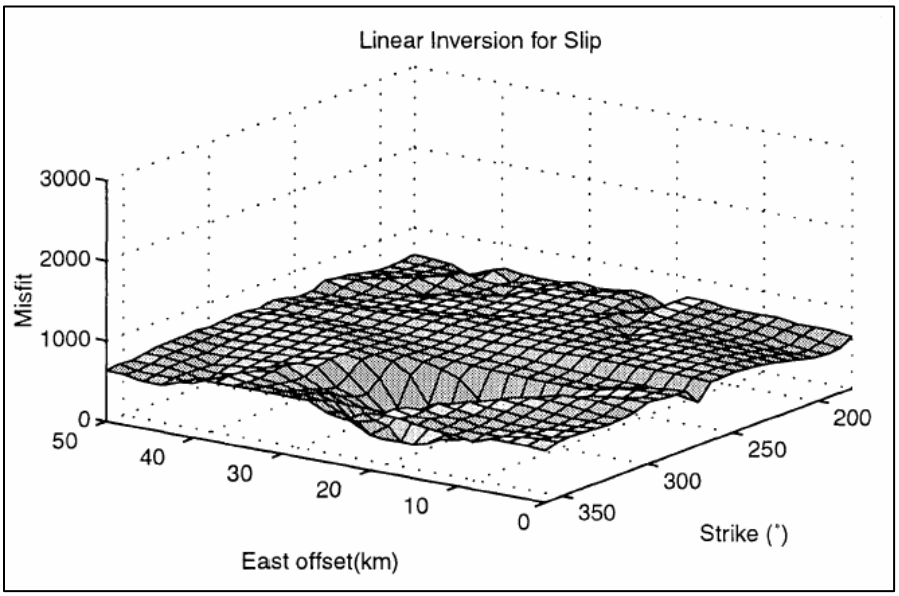

Figure 4.6 Misfit space as function of two model parameters when all the linear parameters are set at their optimal values, in a least-squares sense. The effect is to flatten the misfit space. From *Cervelli et al.,* [2001].

4.6 Experiments with synthetic data

To test the efficiency of the optimization methods described in the previous sections, experiments with synthetic data are presented. The two following test cases represent the end-members from a variety of scenarios that span a wide range of signal-to-noise ratios (SNR). Thus, using elastic dislocations [*Okada, 1985*] with uniform slip, surface displacements from two earthquake were simulated. These synthetic displacements were computed in terms of both angle and elevation changes and furthermore, a synthetic realization of a Gaussian noise was added to the simulated observations. The distribution of the synthetic geodetic stations it is taken to be similar to the real distribution of the application case (see next chapter).

4.6.1 Test Case 1

In test Case 1 the synthetic displacements are very large, corresponding to those generated by a $M_W \sim 7$ earthquake (Figure 4.8).

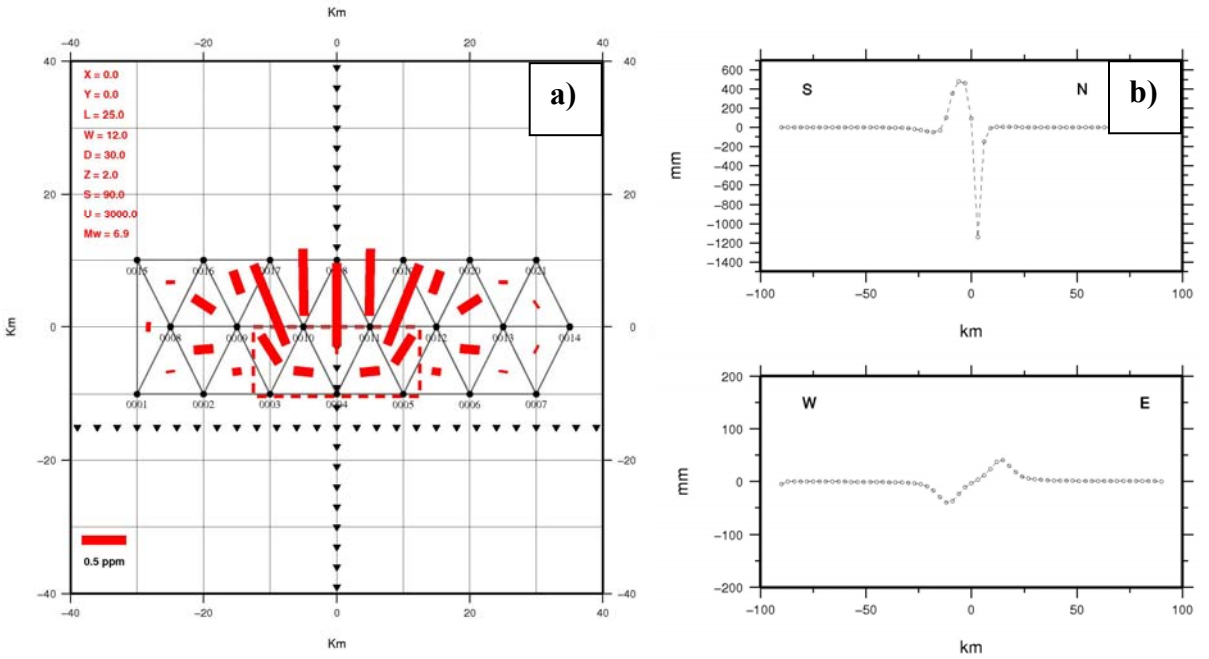

Figure 4.8 (a) The observed displacement field in terms of angle changes for the simulated earthquake represented by Test Case 1. The angle changes are depicted as shear strain (red bars) plotted in the direction of maximum compression. The synthetic dislocation surface is depicted by red dashed box. The net of triangles represents the position of the triangulation geodetic stations, while the inverted triangles indicate the position of the two leveling lines. (b) The observed elevation changes produced by the fault model of Test Case 1, are plotted along each lines. Note that these data are plotted as relative elevation changes between consecutive benchmarks of each route, instead of absolute elevation changes.

Thus, the corresponding high value of the SNR of this case yields to a very deep minimum in misfit space, that potentially could be easily found by the considered optimization algorithms. The synthetic angle and elevation changes, randomly perturbed in a normal distribution about their original values (using an a-priori standard deviation respectively of 0.5 arc sec and 10 mm), were then the input of the two inversion algorithms (GA and SA) considered in this Thesis.

Regarding the optimization technique based on GA, a population of 300 individuals (that in this case means 300 source models) and 300 iterations were chosen in the inversion [*Bagh et al., 2007*]. The GA stopped the search when 70% of the generated source models had an individual global misfit less than a certain threshold. The GA only requires the knowledge of the limits of the model parameters within the search space that include the solution. The ranges of the model parameters used in the inversions as well as the best-fit model parameters are reported in Table 4.1.

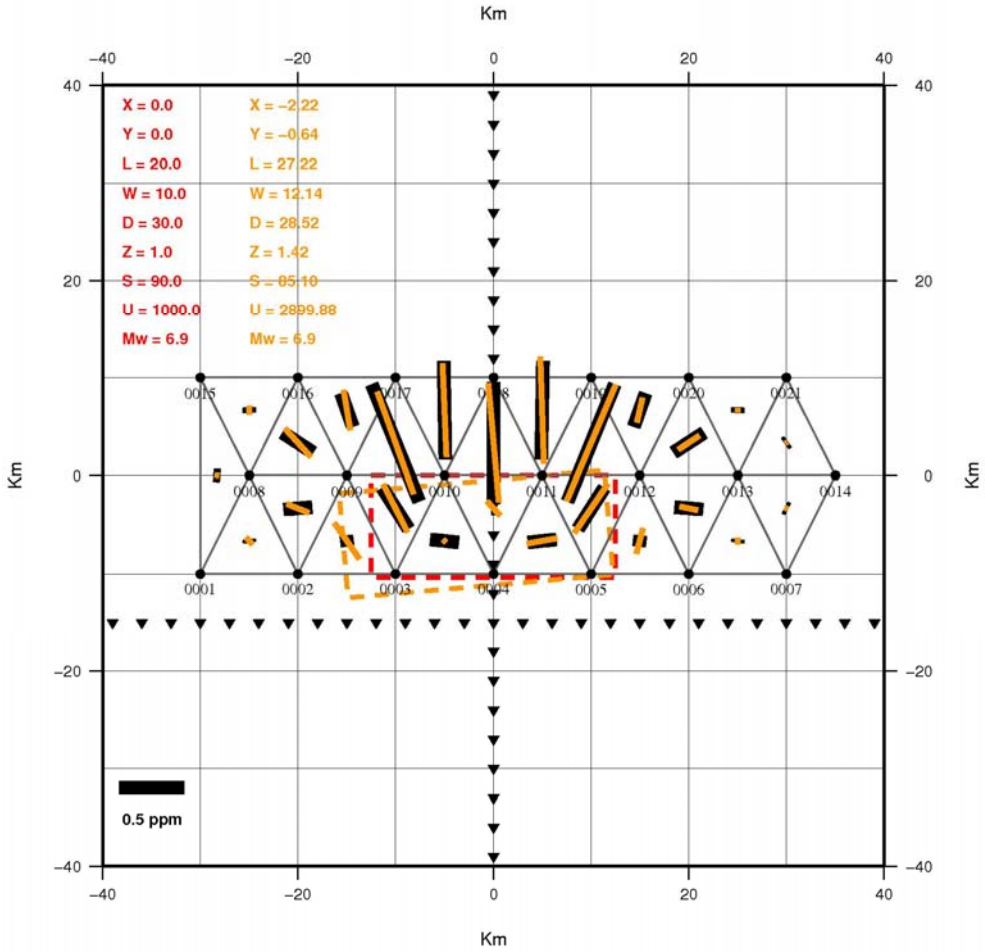

Figure 4.9 GA inversion results. The observed displacement field in terms of angle changes for the simulated earthquake represented by Test Case 1. The angle changes are depicted as shear strain (red bars) plotted in the direction of maximum compression. The synthetic dislocation surface is depicted by red dashed box. The net of triangles represents the position of the triangulation geodetic stations, while the inverted triangles indicate the position of the two leveling lines.

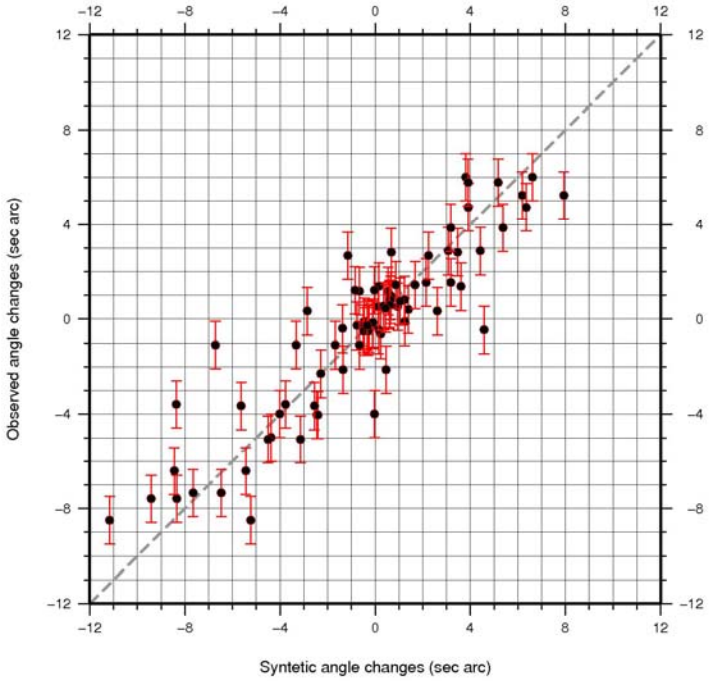

Figure 4.10 GA inversion results. Correlation between observed and modelled angle changes.

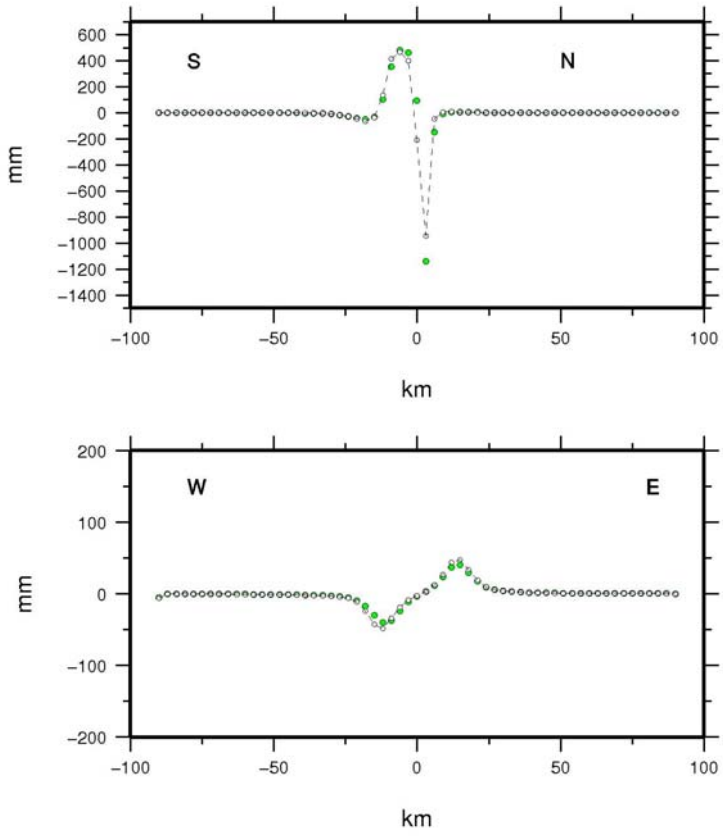

Figure 4.11 GA inversion results. The observed elevation changes are depicted in green, while the modelled elevation changes are depicted in white. Note that these data are plotted as relative elevation changes between consecutive benchmarks of each route, instead of absolute elevation changes.

Regarding the SA optimization technique, as already seen in paragraph 4.3.2.2, the SA algorithm need an appropriate cooling schedule to work well. The parameters that defines this schedule include a starting temperature (T_0), a temperature reduction factor (RT), a number of cycles (NS) and a number of iterations (NT). The suggested values used in these inversions generally come from the work of *Corana et al.* [*1987*]. Obviously also the range of value parameters were set (Table 4.1), according to the previous inversion.

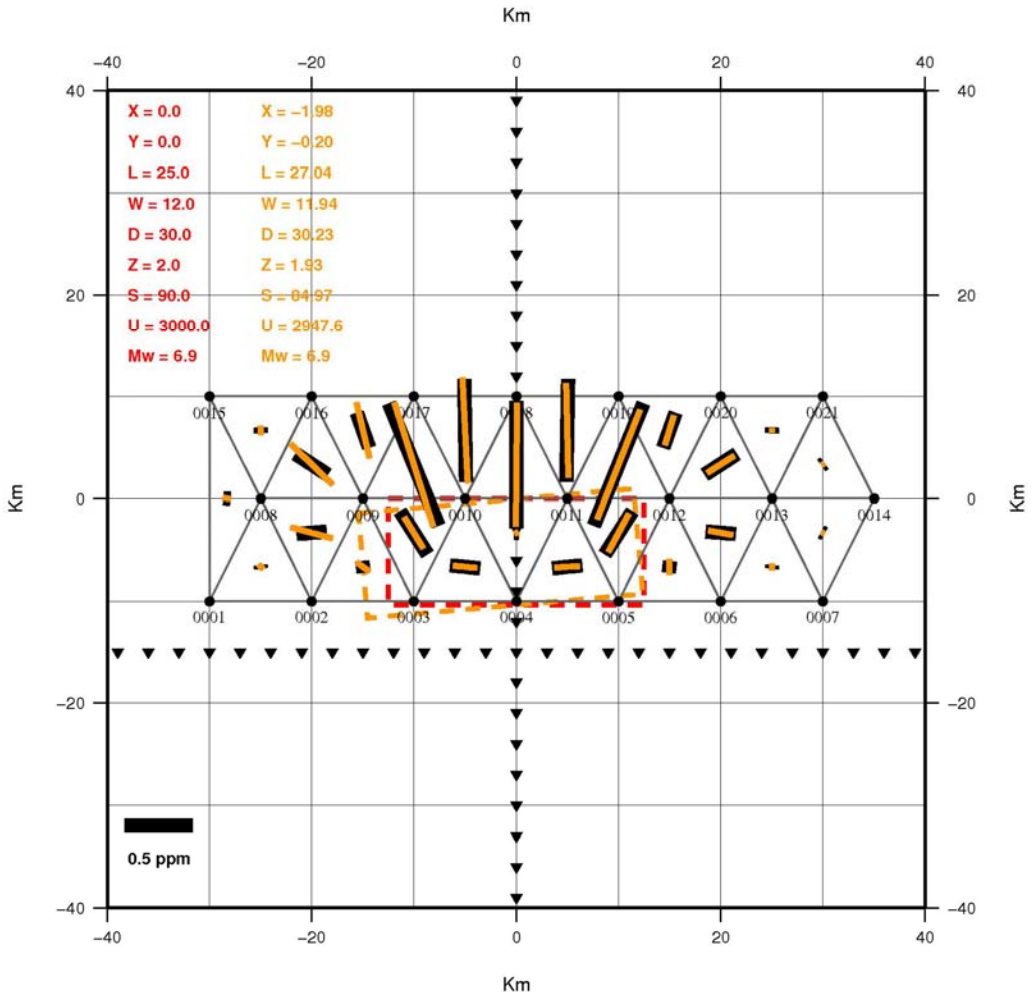

Figure 4.12 SA inversion results. The observed displacement field in terms of angle changes for the simulated earthquake represented by Test Case 1. The angle changes are depicted as shear strain (red bars) plotted in the direction of maximum compression. The synthetic dislocation surface is depicted by red dashed box. The net of triangles represents the position of the triangulation geodetic stations, while the inverted triangles indicate the position of the two leveling lines.

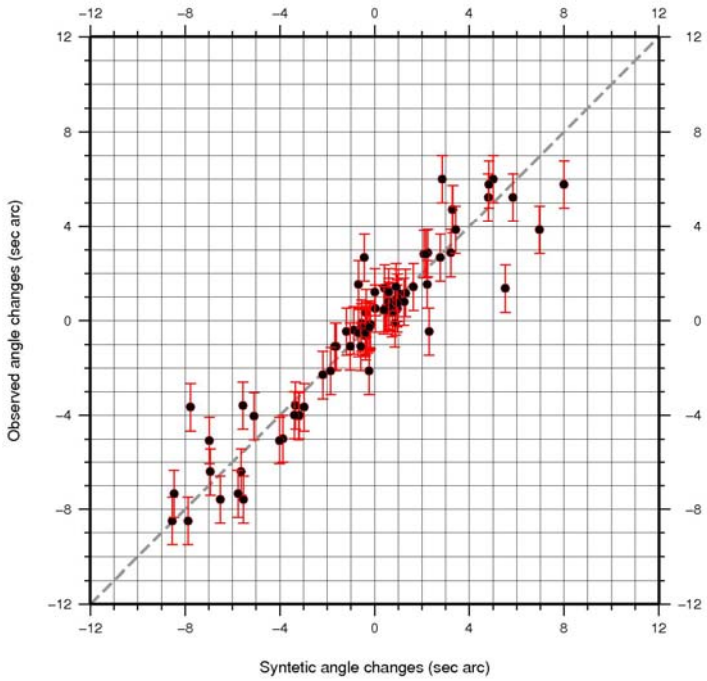

Figure 4.13 SA inversion results. Correlation between observed and modelled angle changes.

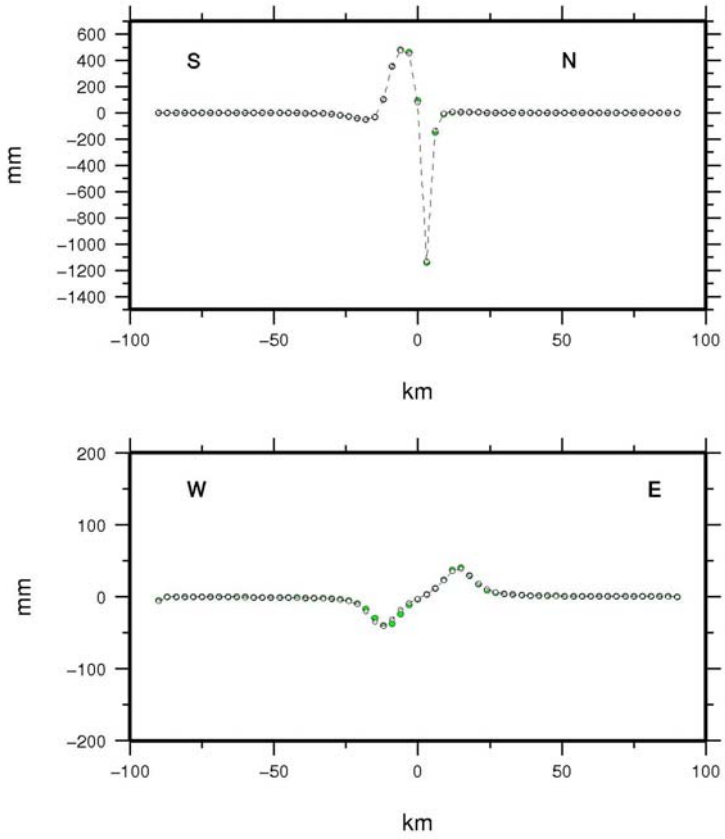

Figure 4.14 SA inversion results. The observed elevation changes are depicted in green, while the modelled elevation changes are depicted in white. Note that these data are plotted as relative elevation changes between consecutive benchmarks of each route, instead of absolute elevation changes.

4.6.2 Test Case 2

In test Case 2 the synthetic displacements correspond to those generated by a smaller earthquake, $M_W \sim 6$ (Figure 4.15).

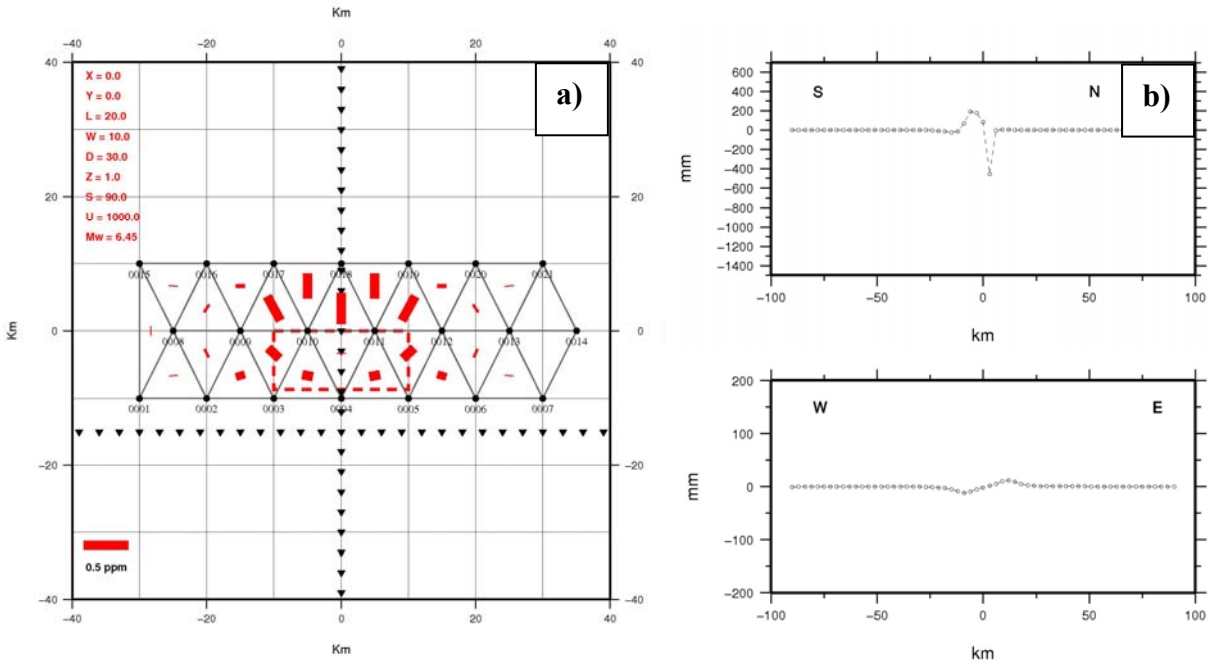

Figure 4.15 (a) The observed displacement field in terms of angle changes for the simulated earthquake represented by Test Case 2. The angle changes are depicted as shear strain (red bars) plotted in the direction of maximum compression. The synthetic dislocation surface is depicted by red dashed box. The net of triangles represents the position of the triangulation geodetic stations, while the inverted triangles indicate the position of the two leveling lines. (b) The observed elevation changes produced by the fault model of Test Case 2, are plotted along each lines. Note that these data are plotted as relative elevation changes between consecutive benchmarks of each route, instead of absolute elevation changes.

Thus, the corresponding low value of the SNR, yields a misfit space without a well defined deep minimum, and this makes more difficult for a optimization algorithm to find the global minimum. Again, the synthetic angle and elevation changes, randomly perturbed in a normal distribution about their original values (using an a-priori standard deviation respectively of 0.5 arc sec and 10 mm), were then the input of the two inversion algorithms (GA and SA) considered in this Thesis.

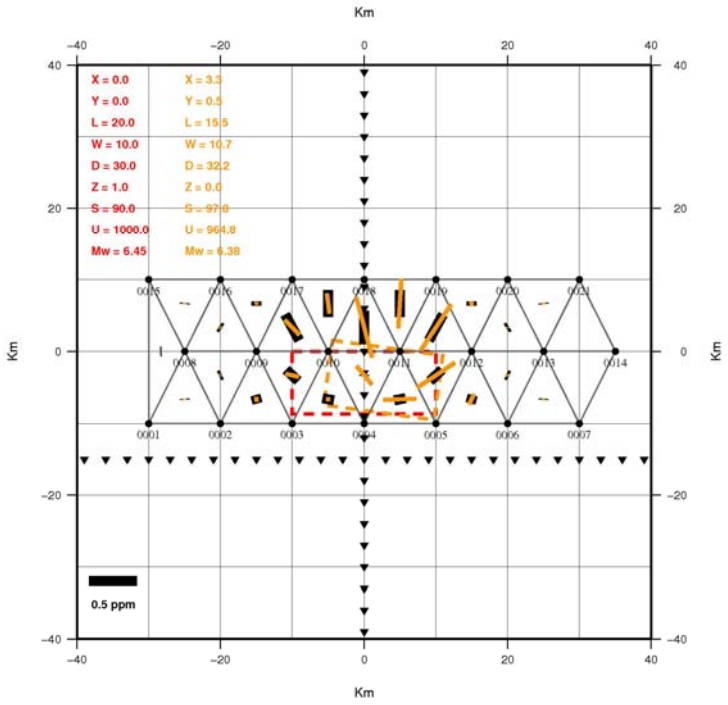

Figure 4.16 GA inversion results. The observed displacement field in terms of angle changes for the simulated earthquake represented by Test Case 2. The angle changes are depicted as shear strain (red bars) plotted in the direction of maximum compression. The synthetic dislocation surface is depicted by red dashed box. The net of triangles represents the position of the triangulation geodetic stations, while the inverted triangles indicate the position of the two leveling lines.

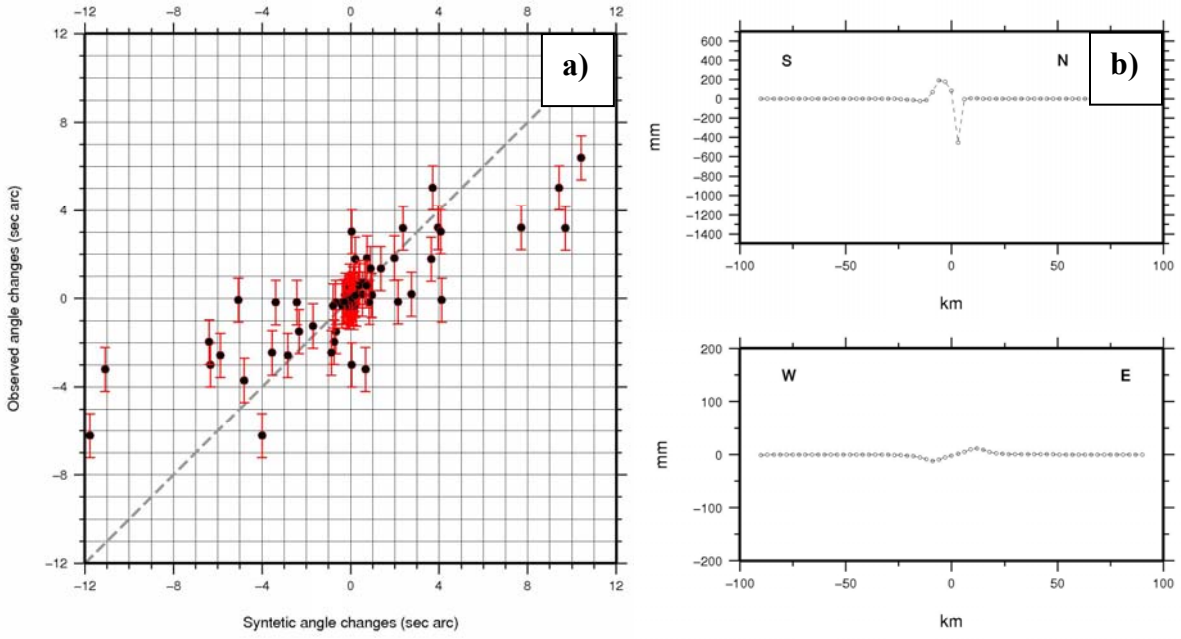

Figure 4.16 GA inversion results. (a) Correlation between observed and modelled angle changes. (b) The observed elevation changes are depicted in green, while the modelled elevation changes are depicted in white. The observed elevation changes are depicted in green, while the modelled elevation changes are depicted in white. Note that these data are plotted as relative elevation changes between consecutive benchmarks of each route, instead of absolute elevation changes.

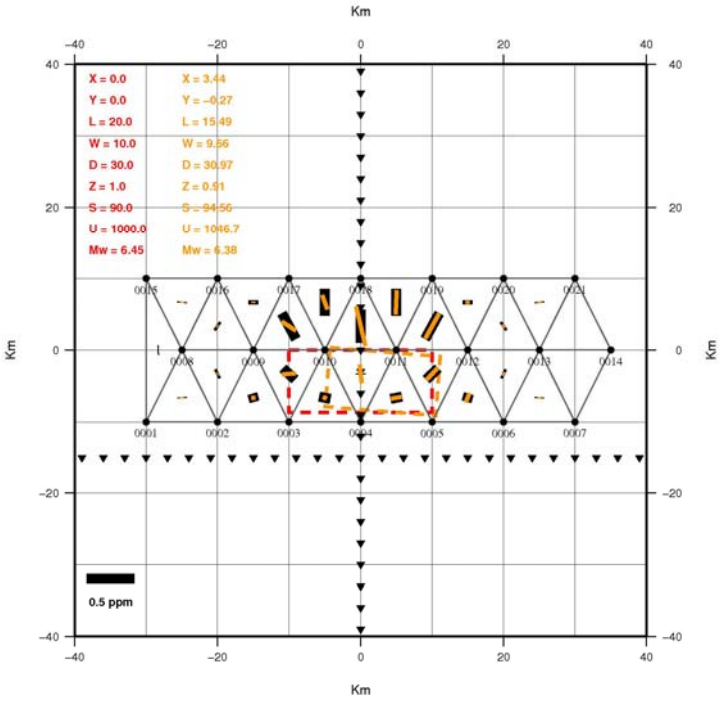

Figure 4.18 SA inversion results. The observed displacement field in terms of angle changes for the simulated earthquake represented by Test Case 2. The angle changes are depicted as shear strain (red bars) plotted in the direction of maximum compression. The synthetic dislocation surface is depicted by red dashed box. The net of triangles represents the position of the triangulation geodetic stations, while the inverted triangles indicate the position of the two leveling lines.

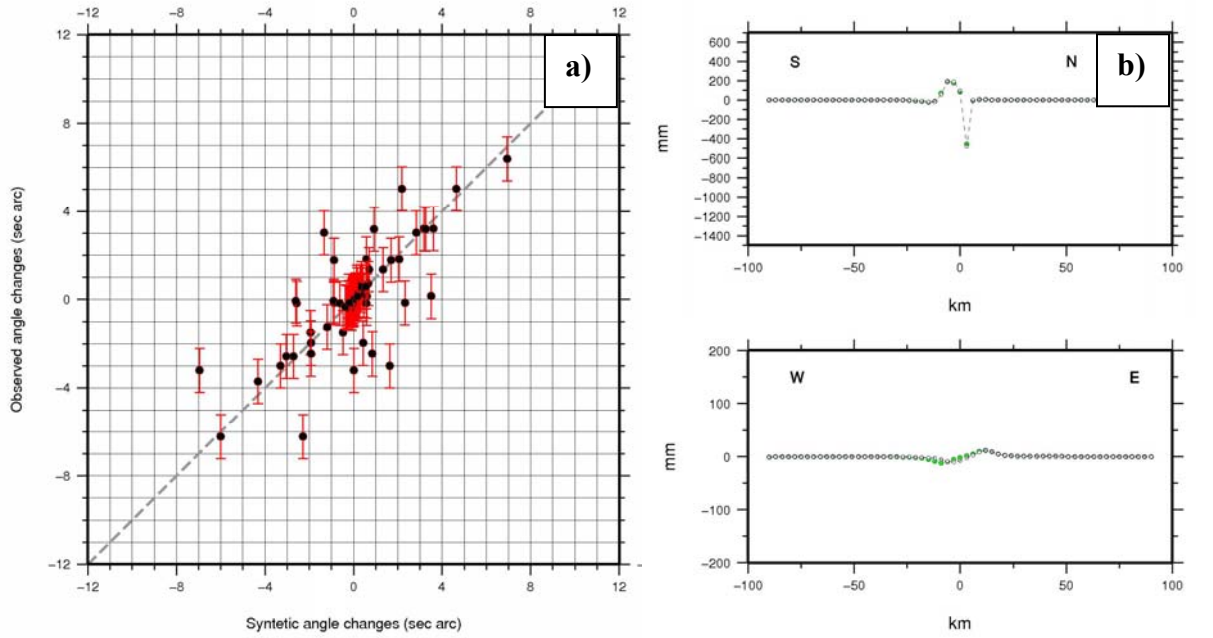

Figure 4.19 SA inversion results. (a) Correlation between observed and modelled angle changes. (b) The observed elevation changes are depicted in green, while the modelled elevation changes are depicted in white. The observed elevation changes are depicted in green, while the modelled elevation changes are depicted in white. Note that these data are plotted as relative elevation changes between consecutive benchmarks of each route, instead of absolute elevation changes.

		Inversion Bounds		Inversion Method	
Parameter	**True Value**	**Lower**	**Upper**	**GA**	**SA**
East offset (km)	0	-30	30	*-2.22*	*-1.98*
North offset (km)	0	-30	30	*-0.64*	*-0.20*
Depth (km)	2	0	10	*1.42*	*1.93*
Length (km)	25	1	40	*27.22*	*27.04*
Width (km)	12	1	20	*12.14*	*11.94*
Strike (deg)	90	20	140	*85.10*	*84.97*
Dip (deg)	30	10	60	*28.52*	*30.23*
Slip (cm)	300	0	500	*289.99*	*294.76*
Mw	6.9			*6.9*	*6.9*

Table 4.1 The Test Case 1 inversion results.

		Inversion Bounds		Inversion Method	
Parameter	**True Value**	**Lower**	**Upper**	**GA**	**SA**
East offset (km)	0	-30	30	*3.31*	*3.44*
North offset (km)	0	-30	30	*0.50*	*-0.27*
Depth (km)	2	0	10	*0.00*	*0.91*
Length (km)	20	1	40	*15.54*	*15.49*
Width (km)	10	1	20	*10.71*	*9.66*
Strike (deg)	90	20	140	*97.82*	*94.56*
Dip (deg)	30	10	60	*32.25*	*30.97*
Slip (cm)	100	0	500	*96.48*	*104.67*
Mw	6.45			*6.38*	*6.38*

Table 4.2 The Test Case 2 inversion results.

Both simulated annealing and genetic algorithms were used to find the global minimum in the two test cases. With respect to the Test Case 1, because of the high SNR, in the many inversions that have been run, both simulated annealing and genetic algorithm found the the global minimum very rapidly. Because of the added noise, the minimum in the misfit function does not precisely correspond to the actual model. Nonetheless, the recovered model mimics the actual model almost perfectly (Figure 4.9 and 4.12).

In cases of smaller SNR, both algorithms seem to work well for finding the vicinity of global minima in misfit space (Figure 4.16 and 4.18). As can be seen in Figure 4.16a, the genetic algorithm inversion result is in favour of models that overestimate the angular observations, while the simulated annealing seems to better estimate the angular observations (Figure 4.19b). The elevation changes are very well reproduced (Figure 4.16b and 4.19b) by both algorithms. Finally, SA generally runs much more quickly than GA, and for this reason, when the same optimization problem needs to be run many time (i.e., for confidence intervals analysis), the use of SA are then preferable.

4.7 Examples from the literature

Terrestrial geodetic observations have been successfully used to give estimates of tectonic deformation in several parts of the world, providing detailed information on ground displacements, such as how active faults move in earthquakes [e.g., *Lin & Stein, 1989; Arnadottir & Segall, 1994; Yu & Segall, 1996; Thatcher et al., 1997; King & Thatcher, 1998; Bilham & England, 2001; Nyst et al., 2006*]. Here, an example from the literature is reported (Figure 4.20), to demonstrate that the historical angular observations can be successfully used to infer source geometry.

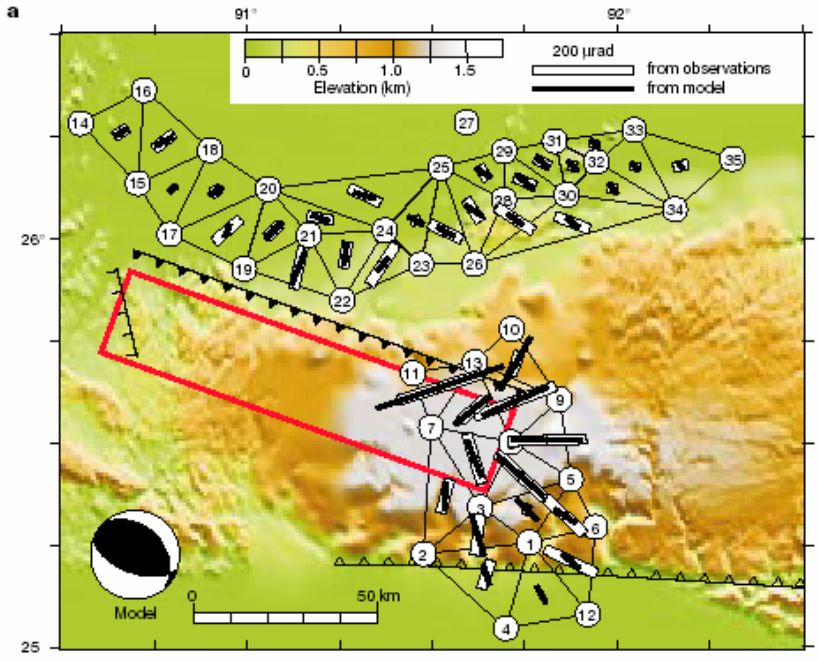

Figure 4.20 Example of inversion of angular geodetic data for source parameters: epicentral region of the Great 1897 Assam earthquake. The bars indicate the shear strains. From *Bilham and England* [*2001*].

4.8 Conclusions

Estimating source geometry from geodetic data is an example of a more general class of geophysical inversion techniques in which observations of surface motion are compared to predictions derived from an assumed physical model of crustal behaviour. In this context, geophysical inversion involves finding an optimal value of a function of several variables. Monte Carlo class of algorithms work well for finding the vicinity of global minima in misfit space. Moreover, because no prior model is required by a Monte Carlo algorithm, if a source estimate from an inversion agrees with geological observation, this is an independent confirmation of the result. In this Thesis, two different Monte Carlo algorithms have been tested and used: a genetic algorithm (GA) and a simulated annealing algorithm (SA). Because the two algorithms function very differently, they provide good independent cross-checks of one another. In the next section (Chapter V), a Monte Carlo optimization method is applied to real observational data set, to estimate source parameters of the 1976 Friuli earthquake.

Chapter V

Source Parameters of the 1976 Friuli (NE Italy) Earthquake Constrained by Triangulation and Leveling Data

5.1 Introduction

Although the 1976 Friuli earthquake has been one of the most damaging events recorded in Northern Italy in the 20th century, causing many victims and destroying large parts of several localities nearby the epicentral area, debate still persists about the reactivated geological structures (see next Paragraph for more details) [e.g., *Aoudia et al., 2000; Pondrelli et al.,2001; Peruzza et al., 2002; Galadini et al., 2005*]. In this Thesis, for the first time, all the geodetic data available, that consist of first to third order triangulation measurements plus vertical displacements from double run high-precision leveling, were jointly inverted to retrieve a source model for the main event that optimally fits the set of coseismic geodetic measurements.

5.2 Seismotectonic setting

The Friuli region is located in the easternmost part of the Southalpine chain, a SSE verging thrust belt characterized by fault propagation faulting and fault bend folding that cause shortening and imbrication of the chain [*Galadini et al., 2005*]. This area is then characterized by the presence of various thrust systems (Figure 5.1). Particularly, the main tectonic structures in the study area, are both E-W trending overthrusts and NW-SE trending overthrusts and faults [e.g., *Amato et al., 1976; Zanferrari et al., 1982*]. The structures with an E-W trending belong to the Alpine tectonic system and are located north of the Periadriatic thrust (PO in Figure 5.1), generally characterized by a dip of about 40° to the North, while the NW-SE trending structures, belonging to the Dinaric system are characterized by a shallower dip angle to the N-NE [e.g., *Amato et al., 1976; Zanferrari et al., 1982; Perniola et al., 2004*]. This structural setting was produced by the superposition of different tectonic phases [e.g., *Doglioni and Bosellini, 1987*].

The current compressional tectonic setting of the Friuli is dominated by the northward motion of the Adriatic microplate with respect to Eurasia (Figure 5.1 and 5.2) [e.g., *Calais et al., 2002; Battaglia et al., 2004; D'Agostino et al., 2005; Serpelloni et al., 2005*] at a GPS estimated rate of ~2.4 mm/yr [e.g., *D'Agostino et al., 2005*]. Regional seismicity and GPS measurements show that most of the current convergence between these two plates is absorbed in the southern Alps through thrusting and crustal thickening with very little or no motion transferred to the north (Figure 5.2a) [*D'Agostino et al., 2005*].

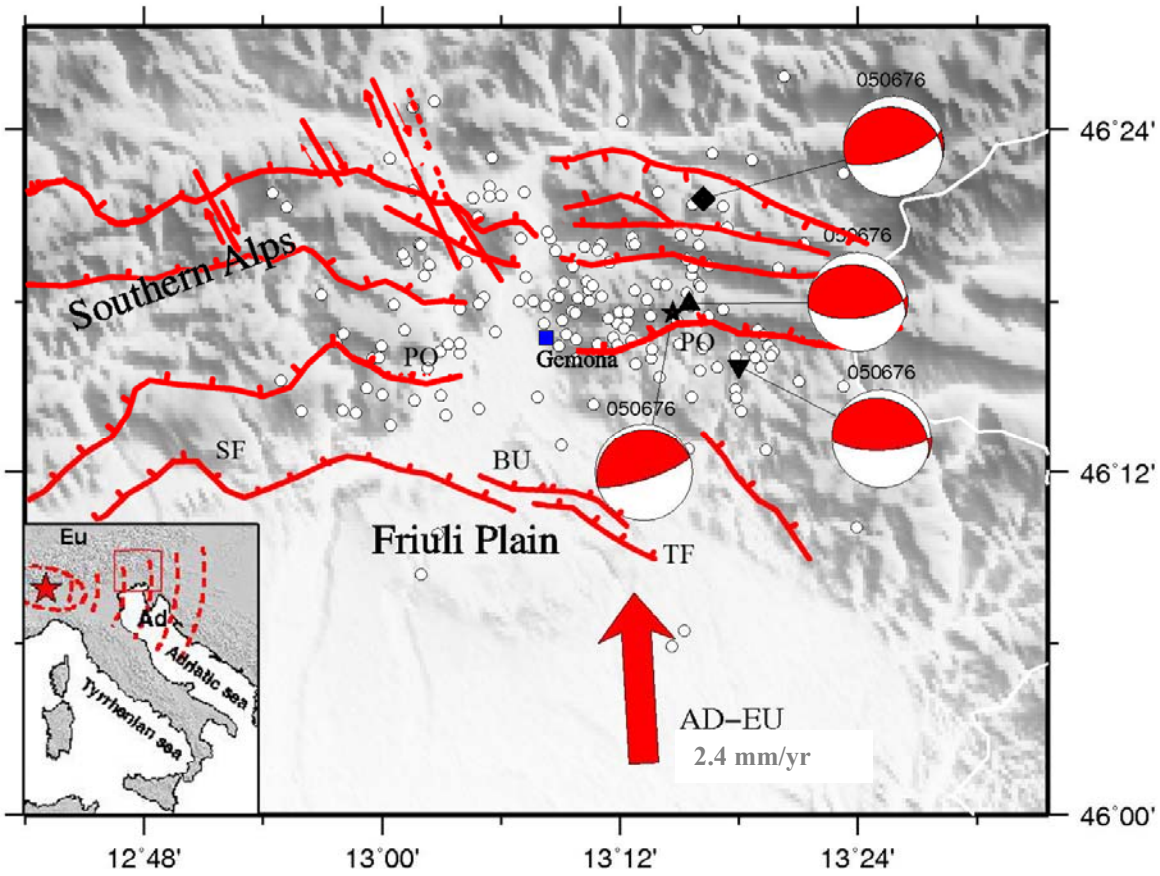

Figure 5.1 Tectonic setting of Friuli region. The red solid lines represent the known tectonic structures of the area: SF is the Sequal fault, BU the Buia fault, TF the Tricesimo fault and PO the Periadriatic overthrust [modified from *Pondrelli et al., 2001*]. The red arrow indicates the relative motion of Adria (AD) microplate with respect to Eurasia (EU), based on CGPS observations [*D'Agostino et al., 2005*]. The circles represent the earthquakes recorded during the 1976 seismic sequence [from *Poli et al., 2002*]. Also shown the fault plane solutions of the main shocks according to different authors [star: *Briole et al., 1986*; triangle: *Aoudia et al., 2000;* diamond: *Pondrelli et al., 2001;* inverted triangle: *Poli et al., 2002*]. The inset shows eulerian pole of rotation of Adria with respect to Eurasia; the small circles represent the direction of motion predicted by that pole of rotation.

The comparison between the GPS horizontal velocities and the topographic swath profile (Figure 5.2b) shows that the largest strain rate is localized along the front of the mountain belt as observed in other actively deforming regions [*D'Agostino et al., 2005*]. Thus, at present, the Eastern Alps represent the most seismic area in the central and eastern Southern Alps, with the main activity occurring close to the relief margin, near the villages of Gemona and Venzone [*Bressan et al., 2003*].

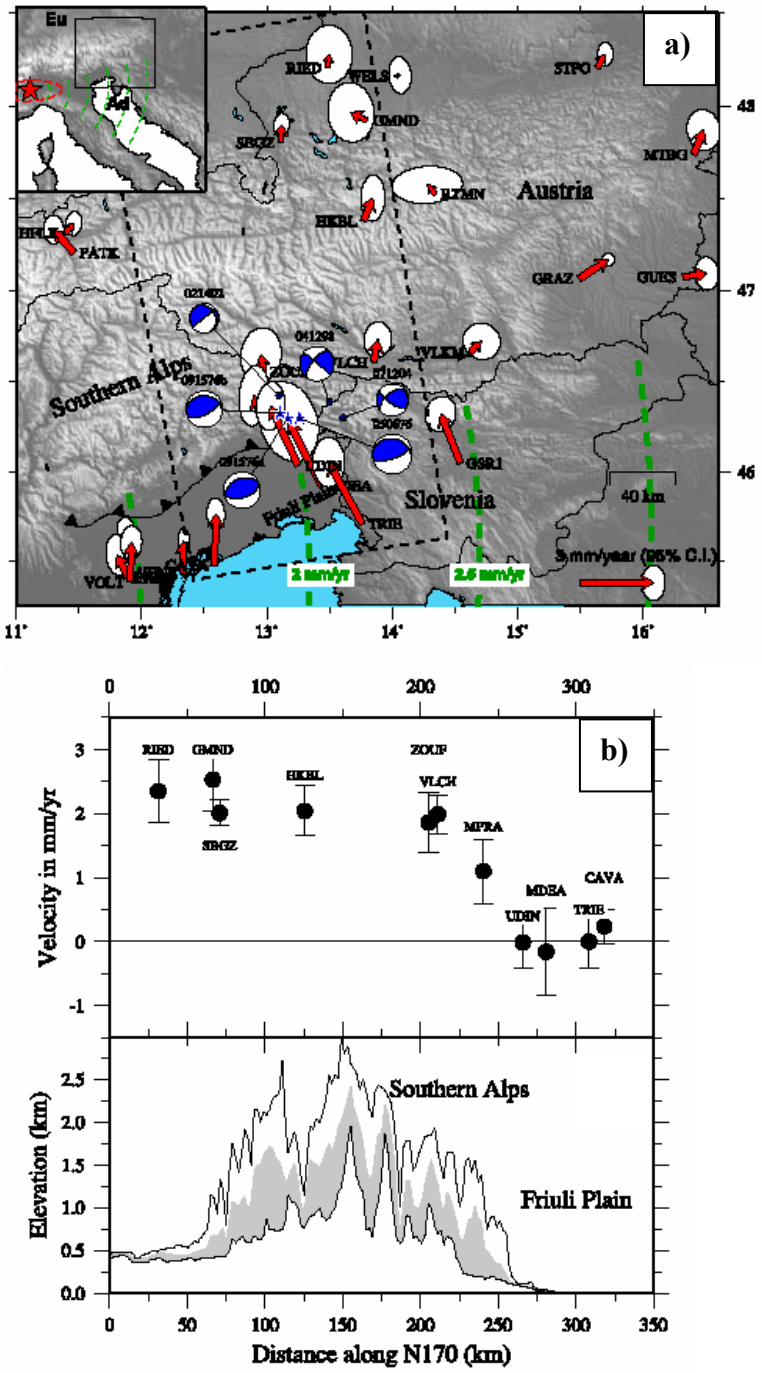

Figure 5.2 a) Current tectonic setting of the southern Alps as depicted by GPS observations. Red arrows are Eurasia-fixed GPS velocities (ellipses 95% C.I.). The black line with triangles represents the southern Alps frontal thrust system. The stars indicate the locations of the 1976 seismic events. Green dashed lines are small circles of constant velocity about the Adria-Eurasia pole of rotation. The rate of shortening between the Friuli plain and the southern part of the eastern Alps, depicted by GPS velocities, shows that the motion of Adria is largely absorbed by thrusting and crustal thickening in Friuli and very little or no motion is rigidly transferred to the north in the Austrian Alps. The black dashed lines encloses the GPS sites whose velocities have been projected onto a N170 direction. b) Projected GPS and topographic data. GPS velocities with respect to TRIE. From *D'Agostino et al.*[*2005*].

Before May 6 1976, this region was struck by only few moderate earthquake with magnitude > 6 (in 1348 and 1511; *Boschi et al.,* [*1997*]). The earthquake sequence started on May 6, 1976 with a M_W = 6.4 event [*Pondrelli et al., 2001*] and the seismic sequence which followed was characterized by numerous aftershocks which decrease in frequency and magnitude until September (main shocks, M_W = 5.9, 6.0 [*Pondrelli et al., 2001*]). This sequence of moderate events has been largely discussed and different focal mechanism solutions have been proposed for the May 6, 1976 main event, computed by seismological data [e.g., *Cipar, 1980; Aoudia et al., 2000; Pondrelli et al., 2001; Peruzza et al., 2002; Poli et al., 2002*] or by the inversion of geodetic data [*Arca et al., 1985; Briole et al., 1986*]. The focal mechanism has been generally interpreted as showing northward dipping thrust motion, with a small dextral E-W strike-slip component (Figure 5.3), whereas there are differences about the location of the main events (Figure 5.1).

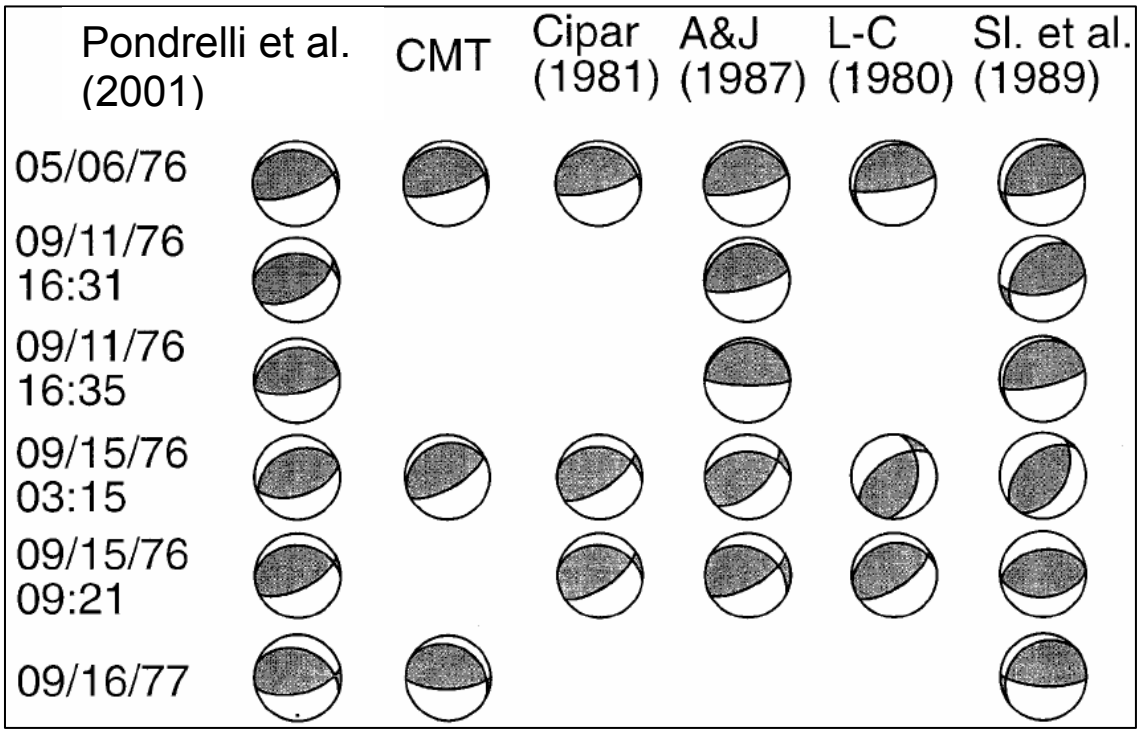

Figure 5.3 Focal mechanisms computed for larger events of the 1976 Friuli sequence as proposed by different authors [modified from *Pondrelli et al., 2001*].

5.2.1 The inferred seismogenetic sources of the 1976 Friuli earthquake sequence

Amato et al. [*1976*], based on a complete geological, geophysical and seismological dataset, reconstructed the evolution of the 1976 Friuli sequence and proposed a faulting mechanism for the main shocks. In particular, analysing the spatial and temporal distribution of the main shocks and of their aftershocks, they pointed out that the hypocentral location of the May event is more to the South and is shallower than that of the September event. Furthermore, they noticed that the hypocenter of the May earthquake lies on the down-dip prolongation of the Buia-Tricesimo thrust. On this basis, the authors hypothesised that the May event occurred on a EW-treding, S-verging, low-angle thrust belonging to the Dinaric system, while the September event was generated by a deeper EW-trending, S-verging, blind thrust, located more to the North and belonging to the Periadriatic system (Figure 5.4).

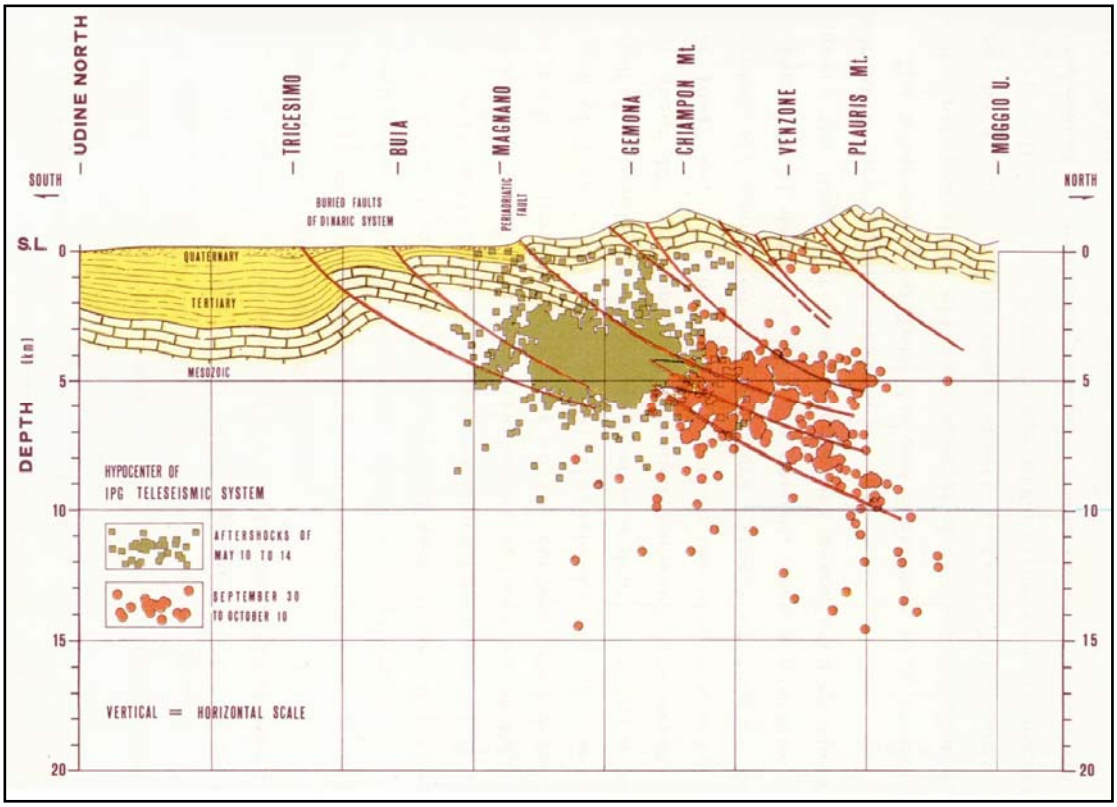

Figure 5.4 Tectonic scheme and hypocenter distribution along a Buia-Venzone cross section. From *Amato et al.,* [*1976*].

Bosi et al. [*1976*] mapped surface ruptures located in the epicentral area of the May 1976 Friuli earthquake by means of air photos interpretation and aerial and field surveys. The authors, on the basis of geomorphic observations, hypothesized the presence of a major EW-trending, S-verging active tectonic structure (the Periadriatic thrust). Furthermore, the authors studied in details the active tectonic structure few days after the May event, mapping several ground fractures located where this thrust outcrops. In particular, the authors described a EW and a SW-NE oriented set of ground ruptures on both sides of Tagliamento river, on the southern slope of Mt. Cuar and Mt. Cuarnan (Figure 5.5). The authors suggested that these ruptures may be the direct surficial expression of slip on a main EW-striking thrust fault as a consequence of the May earthquake.

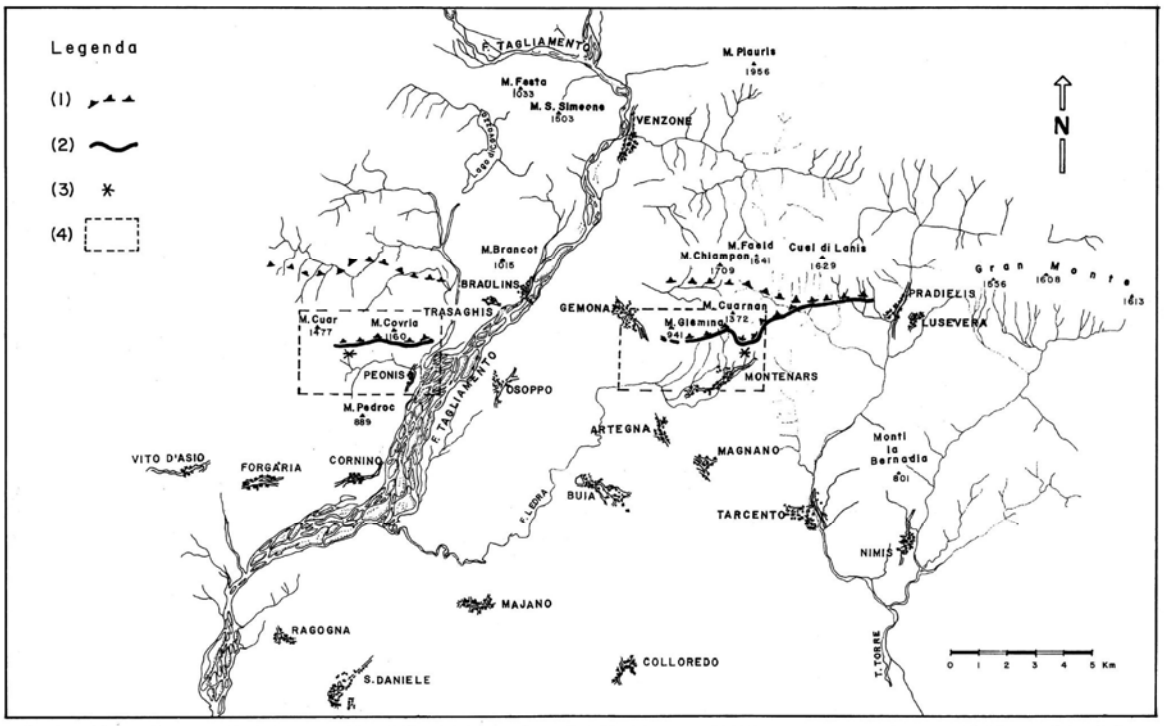

fig. 1 — Corografia generale della zona più colpita dal terremoto. LEGENDA: 1) Elementi del « sovrascorrimento periadriatico ». 2) Contatto tra la zona « calcareo-dolomitica » e « marnoso-arenacea ». 3) Zone delle fratture descritte ai paragrafi 5 e 6. 4) Ubicazione delle aree di fig. 2 e fig. 3.

Figure 5.5 Epicentral area of the 1976 Friuli earthquake. The black lines with triangle indicate the Periadriatic thrust system. The asterisks represent the location of the observed ground ruptures after the May earthquake. From *Bosi et al.,* [*1976*].

Finetti et al. [*1976*], using a mobile seismic array, calculated the epicenter of the May and September main shocks and aftershocks, and proposed a correlation between the main earthquakes and tectonic structures imaged in oil industry reflection profiles. They pointed out that the aftershocks of the May earthquake lay in the area of Gemona, and are found only E of the Tagliamento River; instead the September aftershocks are located northward and have a wider E-W dispersion (Figure 5.6). According to the authors, the projection of the September aftershocks onto a N-S section running East of the Tagliamento river, shows a good fit of the hypocenters with a N-dipping fault plane, which would correspond with the Periadriatic thrust system. Furthermore, the authors hypothesized that the May event occurred on the Buia-Tricesimo thrust fault, while the September event was generated by the Mt. Chiampon thrust fault.

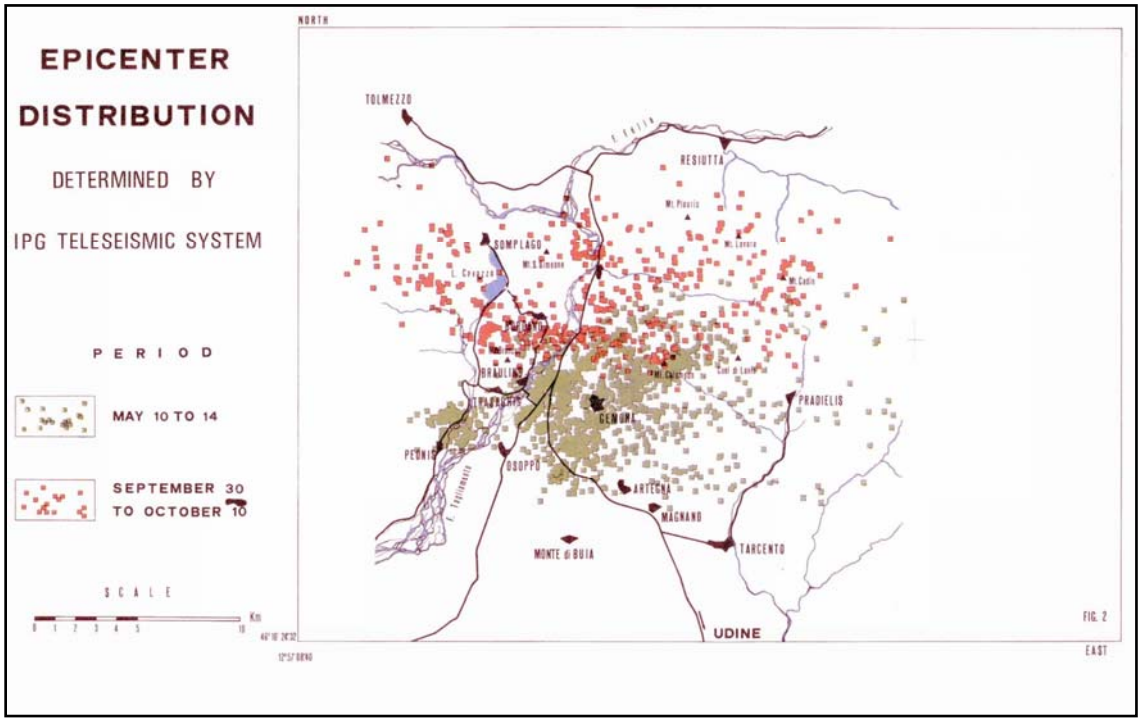

Figure 5.6 Epicenter distribution determined by IPG's teleseismic system after each main shock respectively of May and Septemebr 1976. From *Finetti et al.,* [*1976*].

Lyon-Caen [*1980*] presented a relocation of all the main shocks and the aftershocks of the Friuli sequence and computed the focal mechanism of four main shocks analysing long-period teleseismic body waves. The author pointed out that, even if the hypocentral depths were not well-constrained, all of them appeared to be located between 0 and 12 km depth, and that, the earthquake sequence migrated westward since the epicentral location of the May and September main shocks were aligned in a E-W direction that follows the regional trend of the main tectonic structures.

Cipar [*1980; 1981*] modelled short-period and long-period seismograms of the May event and of the two main September aftershocks using synthetic seismograms. The author found that the hypocenters of the May and September earthquakes are found to lie between 6 and 10 km depth, and based on their focal mechanism they represent underthrusting of the Friuli plain beneath the southern Alps.

Briole et al. [*1986*] proposed a fault model for the main earthquakes of the 1976 Friuli sequence derived from the inversion of leveling data and using as initial fault parameters those proposed by *Lyon-Caen* [*1980*]. According to their best-fitting model (Figure 5.7) the May event occurred on a S-verging, N70°-striking, low-angle thrust located East of the Tagliamento river, while the two September main shocks occurred West of the Tagliamento river, in agreement with the seismological observation of a westward migration of the deformation.

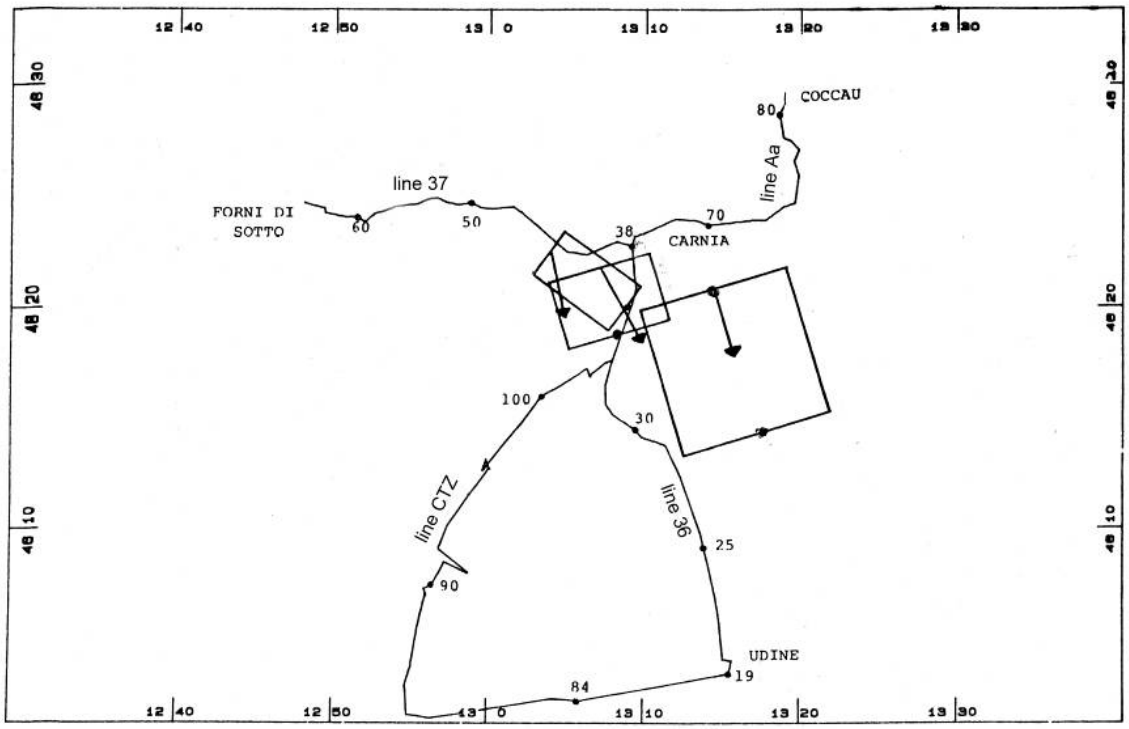

Figure 5.7 Surface projection of the three best-fitting faults. Arrows indicate the surface projection of the hanging wall displacement relatively to the footwall one. The leveling lines 36, 37, A and CTZ are illustrated. From *Briole et al.,* [*1986*].

Aoudia et al. [*2000*] revisited the 1976 earthquake sequence by combining different data sets. Using a joint inversion method of long-period surface waves spectra, the authors calculated the geometrical parameters of the main shock (May event) and of the two largest September aftershocks. In addition, they observed that all the aftershocks were located west of the May main shock, implying an unilateral and westward propagation of the rupture. The authors assumed that the three main events could have occurred on three different segment of a unique S-verging, EW-striking blind thrust, the surface expression of which can be found in the Bernadia thrust and in the Buia and Susans folds (Figure 5.8). The geometrical parameters of their fault model are the: length 18.5 km, width 11.2 km, dip 20° northward, depth of the top 1.5 km.

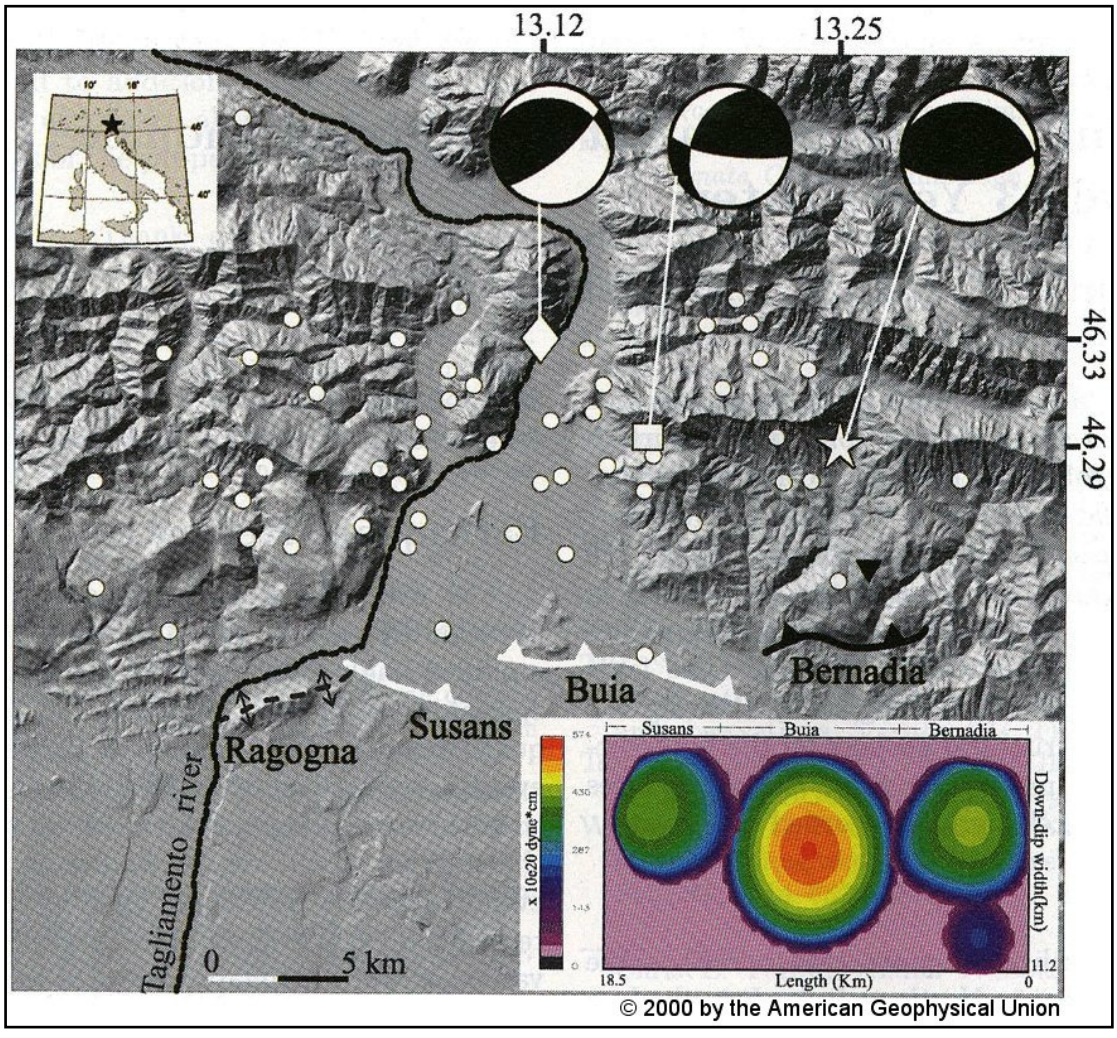

Figure 5.8 Fault model of the 1976 Friuli earthquake. The white barbed lines are the vertical projection of the top of the blind thrusts while the black line corresponds to an emergent thrust. The fault plane solutions fot the main shock (star) and the September aftershocks (square and diamond) are also shown. From *Auodia et al.,* [*2000*].

Pondrelli et al. [*2001*] reviewed the locations of the 10 largest events of the Friuli sequence computing their centroid moment tensors and source parameters. The authors compared their estimates with all available geological, geodetic and seismological data and concluded that most of the earthquakes may be associated with the EW-striking Periadriatic thrust system, whereas only two aftershocks appeared to have occurred on NW-SE-striking Dinaric structures (Figure 5.9).

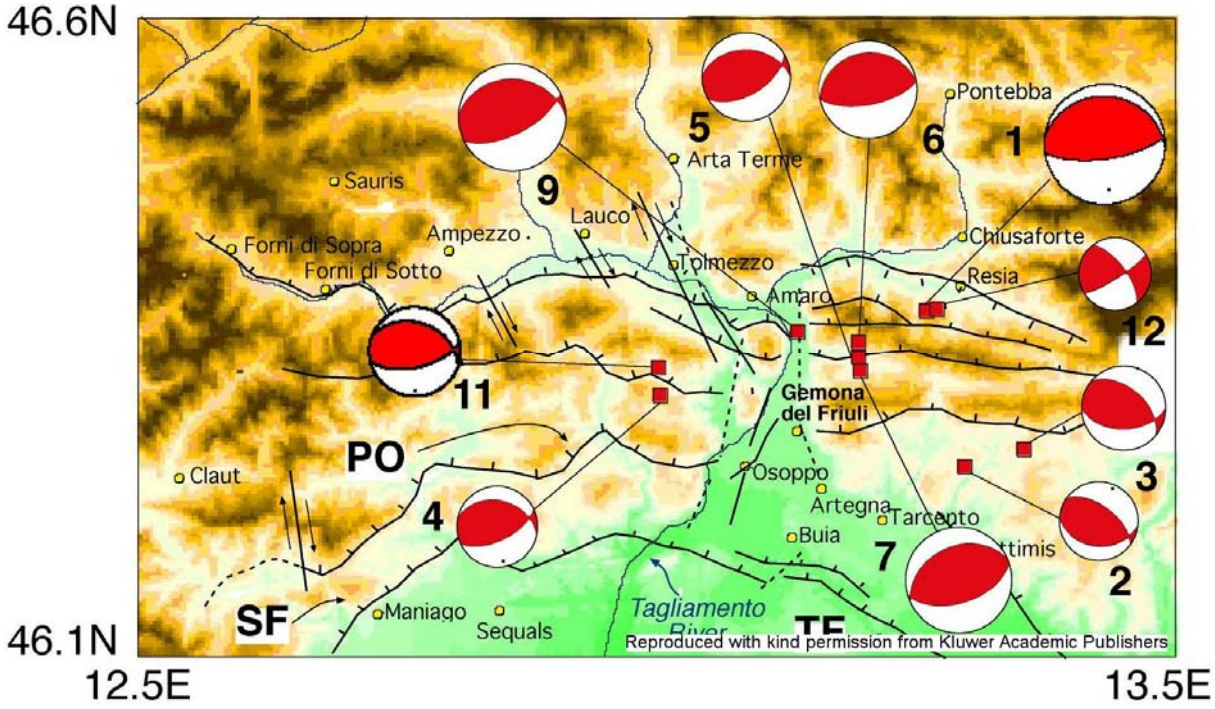

Figure 5.9 Seismotectonic sketch of the area of the 1976 sequence and the 10 relocated largest events. The size of focal mechanism is proportional to the moment magnitude (main shocks n°1, 7 and 9). From *Pondrelli et al.,* [*2001*].

Poli et al. [*2002*] and *Peruzza et al.* [*2002*] re-evaluated most of the seismological data, collected during the first year after the main shock and during the following years. According to the authors the epicentral distribution of the seismicity during the first year clearly showed a north-westward migration from May to September. Furthermore, all the fault-plane solutions of the main events were in agreement with a thrusting mechanism with one plane dipping northward. Finally, the authors emphasised the complex pattern of brittle deformation, suggesting also the presence of high-angle, south-dipping faults.

Perniola et al. [*2004*] used the location and focal mechanisms proposed by *Pondrelli et al.* [*2001*] as starting input for their fault model, and studied it with a Coulomb failure stress approach. The authors justified the whole sequence in terms of mutual stress interaction between adjacent faults. Furthermore, the authors highlighted a westward migration of the seismicity during the sequence, and proposed that the earthquakes characterized by higher magnitude mainly occurred on EW-trending thrusts and triggered the other events on NW-SE-striking faults belonging to the Dinaric system.

Galadini et al. [*2005*], on the basis of structural and geomorphological observations and of the interpretation of a dense grid of reflection seismic profiles, defined the 3-D geometry of 10 seismogenetic sources able to generate M > 6 earthquakes in the Veneto-Friuli plain. They associated the 1976 May main shock with the Susan-Tricesimo thrust, and the September event with the Trasaghis thrust (Figure 5.10).

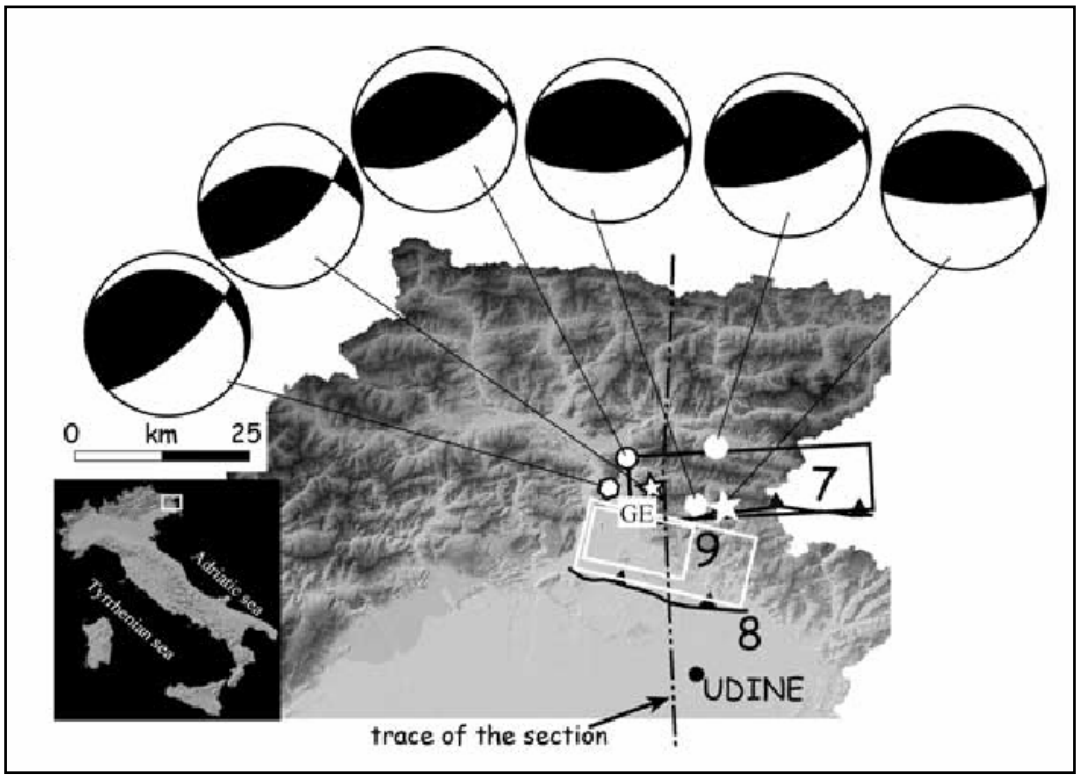

Figure 5.10 Epicentral location and focal mechanisms of the 1976 main shocks. The sources are numbered as: 7, Gemona-Kobarid; 8 Susans-Tricesimo; 9 Trasaghis). From *Galadini et al.,* [*2005*].

In summary, location uncertainties were mainly due to the different methods, but also to the lack of local data, specially for the 6 May main event. [*Pondrelli et al., 2001*]. In fact the main shock has been attributed both to the compressive structure affecting the Buia-Tricesimo area [*Amato et al., 1976; Finetti et al., 1976; Aoudia et al., 2000; Peruzza et al., 2002; Poli et al., 2002; Galadini et al., 2005*] and to the activation of the northward Periadriatic thrust [*Bosi et al., 1976; Perniola et al., 1999; Pondrelli et al., 2001*]. An understanding of these earthquakes in terms of reactivated geological structures is then still a matter of debate.

5.2.2 Open questions

Despite the 1976 Friuli sequence has been largely discussed and different focal mechanism solutions have been proposed for the May 6, 1976 main event, computed by means of different kind of data, some important related questions still remain poorly understood. For example:

- Which fault systems were activated during the 1976 Friuli earthquake sequence?

- Is the rupture process of the whole sequence consistent with the progressive rupture of a single fault system (e.g., as proposed by *Aoudia et al.* [*2000*]) or it involves different thrust systems (e.g., as proposed by *Amato et al.* [*1976*])?

- What is the relationship with the seismotectonic setting?

- Where is the 1976 rupture plane relative to the shear zone active at depth > 5 – 10 km responsible for the interseismic deformation measured with GPS data by *D'Agostino et al.* [*2005*]?

5.3 Geodetic dataset

The data set used in this work consists of two different and independent set of observations: triangulation and leveling measurements. These data were obtained during 2 campaign periods from the Istituto Geografico Militare Italiano (I.G.M.I.), before (1949-1952) and shortly after the earthquake sequence (1977). The close proximity of the leveling

routes and of the triangulation network to the epicentral area permits the estimation of the fault geometry. In this Thesis, for the first time, all the geodetic data available, that consists of first, second and third order triangulation measurements plus vertical displacements from double run high-precision leveling, were inverted to retrieve a source model for the main event that optimally fits the set of coseismic geodetic measurements. By means of the optimal source model, some considerations about which fault system has been reactivated during this sequence, were made.

5.3.1 Triangulation data

Triangulation data measures horizontal deformation using the angles between geodetic monuments. The triangulation network consists of 19 geodetic points of first to third order trigonometric points (Figure 5.11), angularly measured in 1949 and 1977 [*IGM-RG, 1978*] and adjusted in the classical way by the I.G.M.I., keeping fixed two points which were considered sufficiently far away from the area affected by coseismic deformation [*IGM-RG, 1978*].

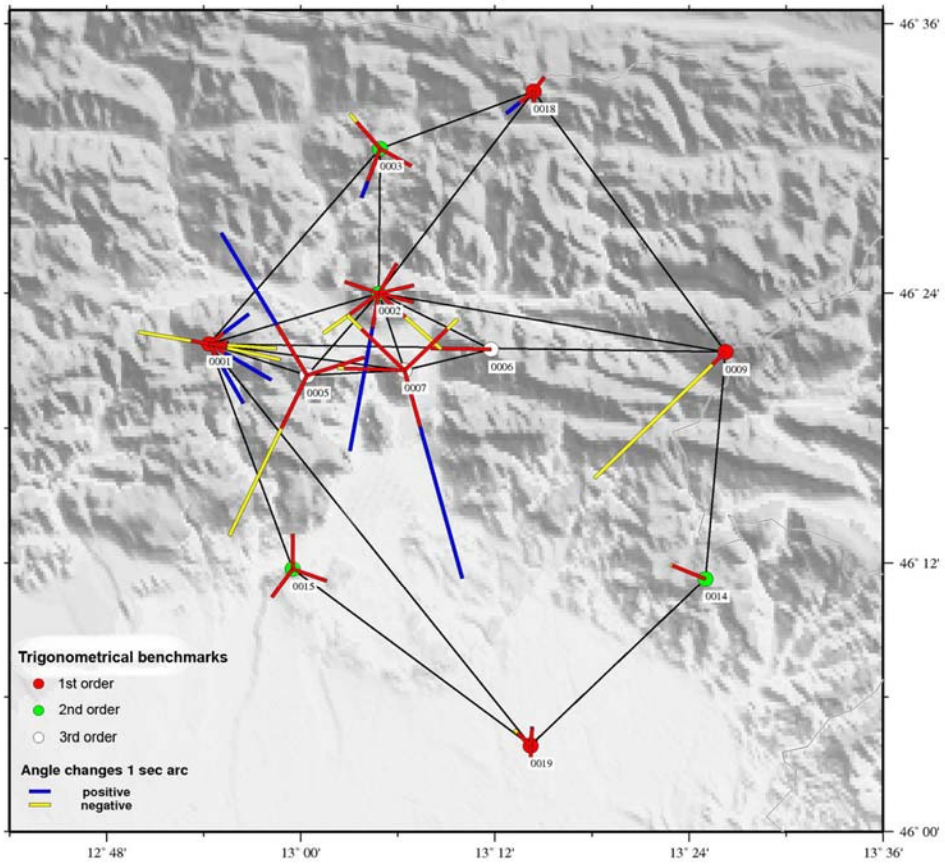

Figure 5.11 Observed angle changes and triangulation network in the epicentral area. The bars are proportional to the observed coseismic angle changes. The red bars show the assumed a priori uncertainties.

The 1949 - 1977 Friuli Angle Changes (36 angles)

Triangle			Δθ (observed)	Triangle			Δθ (observed)
A	V[a]	B	*arc sec*	A	V[a]	B	*arc sec*
05	01	19	3,39	07	05	01	-8,58
19	01	15	3,29	01	05	02	8,00
15	01	03	-3,36	07	06	02	0,32
03	01	02	2,35	06	07	05	10,44
02	01	09	0,91	05	07	01	-3,13
09	01	07	-3,17	01	07	02	-3,80
07	01	05	-3,41	02	07	06	-3,51
03	02	18	0,35	14	09	02	-8,65
18	02	09	-0,41	09	14	19	-1,79
09	02	06	0,66	10	15	19	-0,90
06	02	07	-3,99	19	15	01	0,66
07	02	05	7,77	01	15	10	0,24
05	02	01	-3,25	09	18	02	-0,92
01	02	03	-1,13	02	18	03	1,67
18	03	02	-0,35	03	18	09	-0,75
02	03	01	2,54	14	19	15	0,18
01	03	18	-2,19	15	19	01	-1,07
02	05	07	0,58	1	19	14	0,89

Abbrevation: A,V and B are the triangle vertices; Δθ is the angle change.
[a] is the angle vertex (clockwise from AV to BV).
The computed average uncertainties for the angle changes is given by $\sqrt{\sigma_{1949}^2 + \sigma_{1977}^2}$

Table 5.1 Observed angle changes.

These triangulation data were firstly analyzed by different authors to derive the strain pattern of the area struck by the earthquake sequence. On the basis of these data *Livieratos* [*1980*] has shown a concentration of high values of the maximum shear strain located between San Simeone, Brancot, Chiampon and Plauris, varying from $5 \cdot 10^{-5}$ to $16 \cdot 10^{-5}$. Using the same dataset *Bencini et al.* [*1982*] have computed a peak of maximum shear strain between Venzone and Gemona. However these data were never used to infer the geometry of the source. In fact, these data set have been disregarded by *Briole et al.* [*1986*] due to the possible large instrumental errors and problems concerning the network compensation. Furthermore, the computed horizontal displacements produced by their dislocation model for

the triangulation benchmarks were not compatible with the observed values reduced by fixing two northernmost and southernmost points.

The general method to use triangulation data for the determination of surface deformation is to construct a reference frame from the sites that are assumed to have remained stable during the earthquake and to explicitly determine the coordinates of all sites at each epoch with respect to this reference frame. Then the displacement field is simply computed from the difference in the displacements. In the following analysis, to avoid reference frame problems and to minimize the influence of systematic errors, we use the difference between repeated angle observations as a measure of relative deformation of the geodetic network [*Thatcher, 1979; Bilham & England, 2001; Nyst et al., 2006*], instead of horizontal displacements. Of course, a disadvantage of this method is the use of only the repeated angle observations from the two measurement surveys instead of all measurements. Furthermore, in the subsequent inversion, all the poor reliable benchmarks were excluded (in particular the unstable benchmarks, e.g., the benchmarks materialized as bell tower). Then, the final triangulation data set consists of 36 repeated angles (Table 5.1).

There are different ways to judge the accuracy of a triangulation measurement. For example, an unbiased estimate of the accuracy of a repeated measurement is simply given by its variance. However simply repeating the measurement does not involve resampling all the sources of random error (centering, leveling and lateral refraction errors for example) and then the use of variance would give too optimistic a measure of the precision of an observed angle [*Cross, 1990*]. A better way to determine the accuracy of a repeated measurement is to compare its result with some known value. In this case, with angle measurements, it is know that the three angles in a plane triangle should sum to 180° (plus the spherical excess). Using the *Ferrero*'s formula [e.g., quote by *Bomford, 1980; Cross, 1990*] the average observational error (ε_a) in a network of N closures is given by:

$$\varepsilon_\alpha = \sqrt{\frac{\sum_{i=1}^{N} (\delta c)^2}{3N}} \tag{5.3.1}$$

where δ_c is the triangle closures. By using the (5.3.1) average observational error for the Friuli triangulation network is 2.5 sec arc.

5.3.2 Leveling data

Leveling measures vertical deformation using elevation differences between geodetic monuments. The double run high precision leveling data are related to 96 benchmarks distributed along 3 lines (line 36-Udine/Carina; line 37-Carina/Forni di Sotto; line Aa-Carnia/Coccau; Figure 5.12) and measured in 1952 and 1977 by the I.G.M.. These measurements were made according to the highest precision leveling standards [*Talamo et al., 1978*].

The leveling measurements has been firstly analyzed by *Talamo et al.* [*1978*] to retrieve a description of the altimetry variations of the ground. *Briole et al.,* [*1986*] modelled only the observed vertical deformation by means of three different faults, with the largest ones associated with the 6 May 1976 event and defined by a rectangular fault plane ENE-WSW trending located about 5 km south of Gemona.

The principal features of the observed coseismic elevation changes are an area of maximum uplift of about 20 cm along line 36 and an area of subsidence of about 10 cm along both the three lines, located respectively southward and northward of the Venzone-Monte San Simeone line (Figure 5.12). To avoid problems concering absolute reference datum, we use these data in terms of relative elevation changes between consecutive benchmarks of each route, instead of absolute elevation changes.

A method to estimate the accuracy of the double-run leveling measurements is to consider the discrepancies between forward and backward leveling of consecutive benchmarks. Follow *Talamo et al.* [*1978*] we estimate the associated a posteriori errors between consecutive benchmarks through the formula:

$$\varepsilon_L = \pm 2.5\sqrt{L} \tag{5.3.2}$$

where L is the distance in km between two consecutive benchmarks. Using the (5.3.2) we have computed the a posteriori discrepancies that result in a mean error of 3.0, 2.6 and 2.8 mm (for km) for the route Aa, 37 and 36 respectively. However *Talamo et al.* [*1978*] have estimated a very small mean error of 0.98 mm for km for each leveling lines. The leveling errors are therefore very small compared to the errors of the angle changes and this can be illustrated by the difference in signal-to-noise ratio of both data types, which is 8.57 for the leveling data and 1.14 for the triangulation data. Following *Nyst et al.* [*2006*], in the subsequent inversion a weighting factor was introduced to allow for the leveling data to

dominate the searching. This factor is defined as the ratio of the signal-to-noise ratios of leveling and triangulation data.

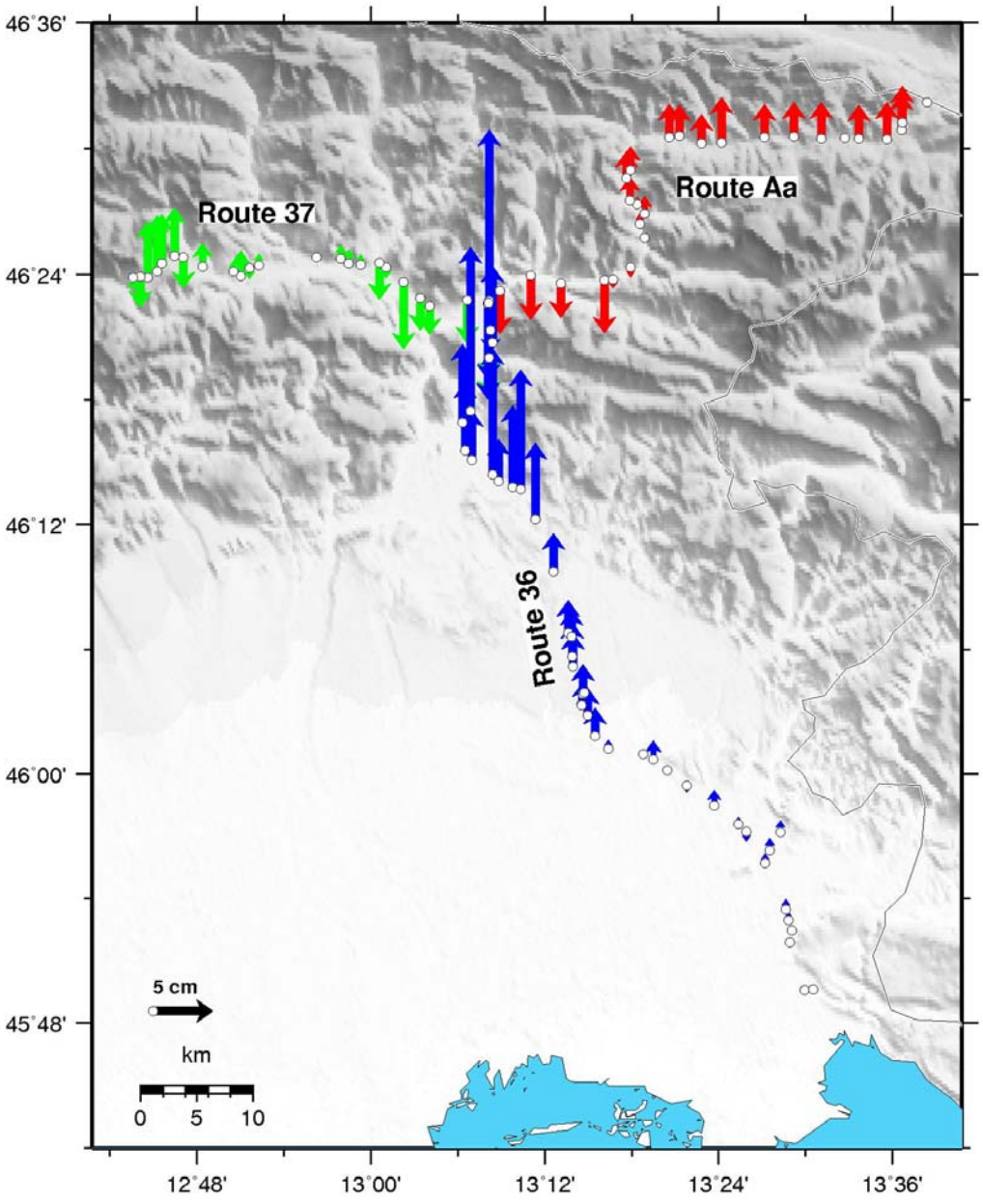

Figure 5.12 Observed vertical displacement along the three leveling routes in Friuli (37 in green, 36 in blue and Aa in red).

The coseismic elevation changes reveal an unplift of around 20 cm on route 36 in the sector between Artegna and Venzone, relative to the initial point of the line. The area were the three leveling lines joint together (northward of the Venzone-M. San Simeone line) underwent subsidence with a maximum of around 10 cm.

5.4 Adjustment for interseismic deformation

Because of the relatively longer span time intervals (about 30 years) between the two surveys (Figure 5.13), some nominally "coseismic" observations could be influenced by interseismic secular deformation. Under the assumption that the style and rate of deformation in the study area are the same before and after the 1976 earthquake, the geodetic data were adjusted by using an interseismic velocity model for the Friuli region, based on continuous GPS data [*D'Agostino et al., 2005*], over the appropriate time interval. This shear zone, responsible for the interseismic deformation, is defined by a creeping dislocation located along the front of the southern Alps, verging northward, and characterized by an horizontal component of the slip on the fault of about 2.4 mm/yr. The horizontal velocity field in an Eurasian frame is then dominated by the roughly N-S convergence of the Adria microplate at a rate of ~ 2.4 mm/yr (Figure 5.1 and 5.2). This causes a general uplift of the mountain chain (Figure 5.14).

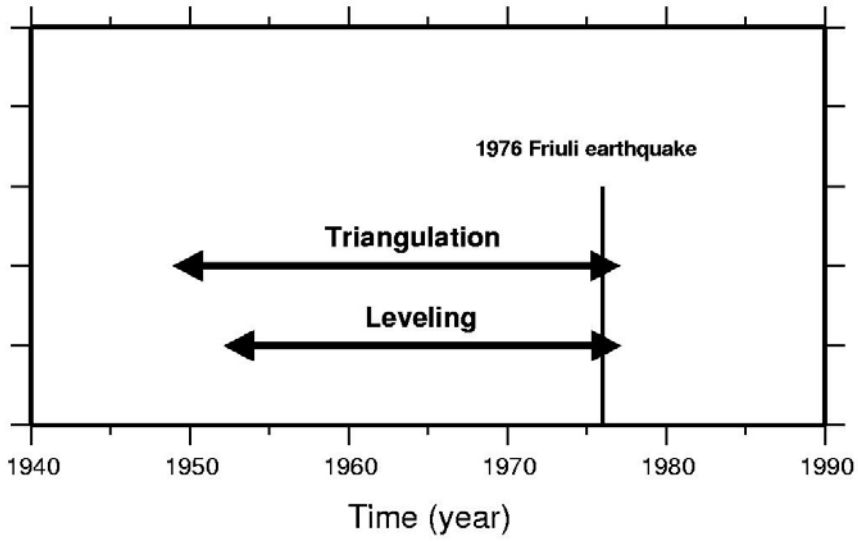

Figure 5.13 Temporal scheme of the triangulation and leveling surveys related to the 1976 Friuli earthquake.

Therefore the interseismic velocity field is both opposite and concordant in sense to the coseismic deformation, causing increase or decrease in the coseismic signal depending on the location of each individual geodetic sites. However, as shown in Figure 5.15, due to the low rate of deformation and to the position of the geodetic stations with respect to the GPS-based interseismic velocity model, the interseismic deformation accumulated between 1949 and 1976 for both triangulation and leveling data can be considered as only a minor part of the

coseismic signal (~ 5 cm of maximum uplift along line 36) and so no corrections were made to account for it.

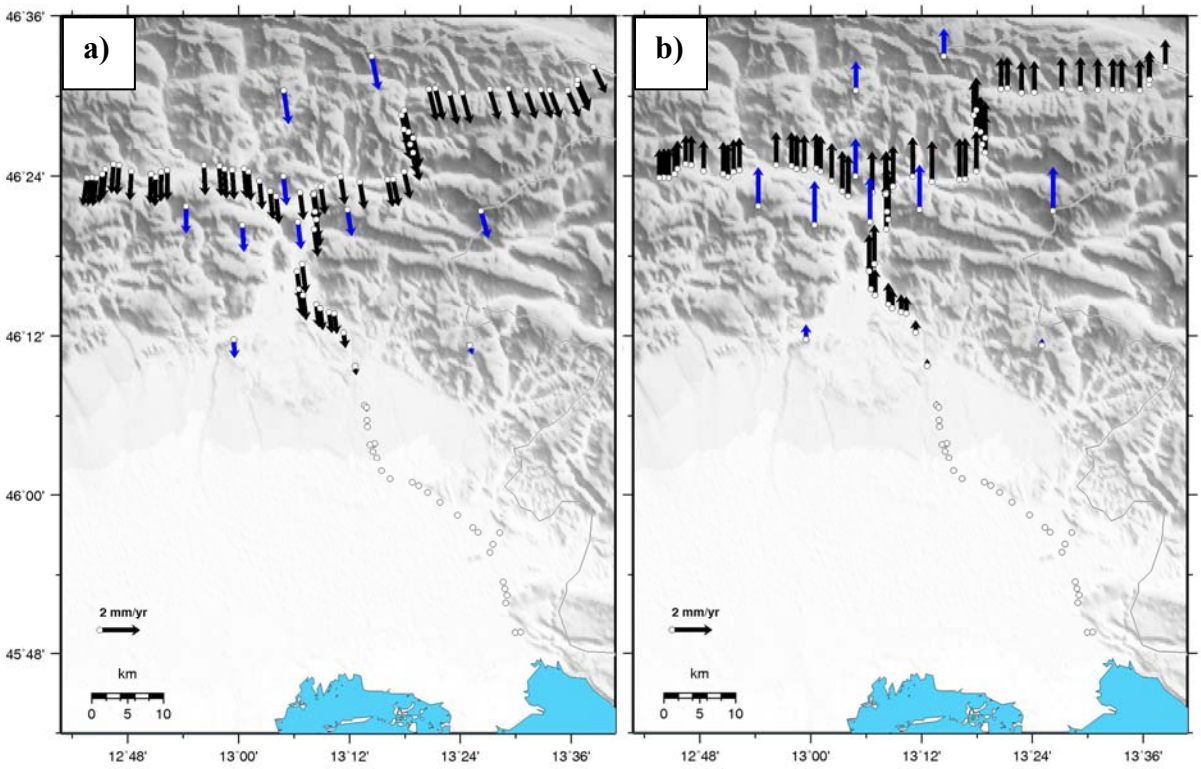

Figure 5.14 Interseismic velocity field based on GPS observations [*D'Agostino et al., 2005*] in an Adria reference frame. (a) Horizontal velocity vectors computed at triangulation (blue arrows) and leveling (black arrows) benchmarks. (b) Vertical velocity plotted at the same benchmarks.

5.5 Inversion procedure

The inversion problem consists in estimating the dislocation parameters at depth from the geodetic data (see Chapter IV for more details). The relationship between the deformation field and the source geometry can be expressed by the following equation:

$$\mathbf{d} = \mathbf{G}(\mathbf{m}) + \boldsymbol{\sigma} \tag{5.5.1}$$

where **d** is the deformation data vector, **m** is the source geometry vector, **G** is the function that relates the two and **σ** is a vector of observation errors. For the source geometry estimation problem the data are related non-linearly to the source parameters. The optimal source model will minimize the misfit between observation and prediction. To quantify the misfit between observation and predicted deformation for each model, a classical weighted residual sum of squares, *MSE*, (normalized by the number of individual data, *N*, minus the number of estimated model parameters *m*) was used:

$$MSE = \frac{1}{N-m}\sum_{n=1}^{N}\frac{(d_i - p_i)^2}{\sigma_i^2 w_i} \tag{5.5.2}$$

where d_i is the *i*th-observation, p_i the *i*th-prediction, σ_i the standard deviation of d_i and w_i a weighting factor. The weighting factor is defined as the ratio of the signal-to-noise ratios of leveling and triangulation data. The introduction of this factor in the misfit function allows to equally weight the two different data set in the computation of the misfit value.

Different methods have been developed for rigorously invert surface deformation fields for source type and geometry (see Chapter IV). In this study, after some preliminary tests (see paragraph 4.6), a simulated annealing (SA) algorithm was used to estimate the overall earthquake geometry and motion, using the *Okada* analytical solution for deformation. The SA is stochastic search methods, that is, it is a useful tool for solving non-linear problems with many local minima (see Chapter IV for details about these searching algorithms).

The geodetic data sets were jointly inverted using an appropriate weighting. The introduction of a weighting factor in the misfit function, permits to consider one data misfit value based on both leveling and triangulation data, without having one data set dominate the searching in the modelling [e.g., *Nyst et al., 2006; Peyret et al., 2007*], so that the misfit is approximately equilibrated between the different data sets used. In the computation, the

angular and elevation changes has been treated as they reflect homogeneous slip on a rectangular plane buried in an isotropic, elastic, uniform half-space. Following O*kada* [*1985*] this model can be evaluated from nine parameters that describe the geometry, the slip of the plane and the spatial coordinates of one corner of the fault plane.

Thus, starting with the simplified hypothesis that the rupture process of the whole sequence (May shock plus September shocks) could be consistent with the progressive rupture of a single fault system, the geodetic data were initially jointly inverted for a single fault plane. Initial models used no a priori constraints allowing all parameters to vary over a wide range, with the exception that the north dipping plane was chosen because of the seismotectonic setting of the area (see Paragraph 5.2): ±20 km location, 1-30 km length, ±50° strike, 0-10 km depth, 1-20 km width, 1-60° dip, reverse-slip 0-3 m, strike-slip ± 3m.

The best-fitting solution, in the sense of minimizing the misfits to the angular changes and to the elevation changes normalized by their uncertainties is shown in Table 5.2. The model reproduces well the strongest uplift signal along route 36 and the northward subsidence along route 37 and Aa, whereas it does not reproduce the other southward small features along route 36 (Figure 5.16). The angles changes are instead well reproduced almost anywhere (Figure 5.15 and 5.17).

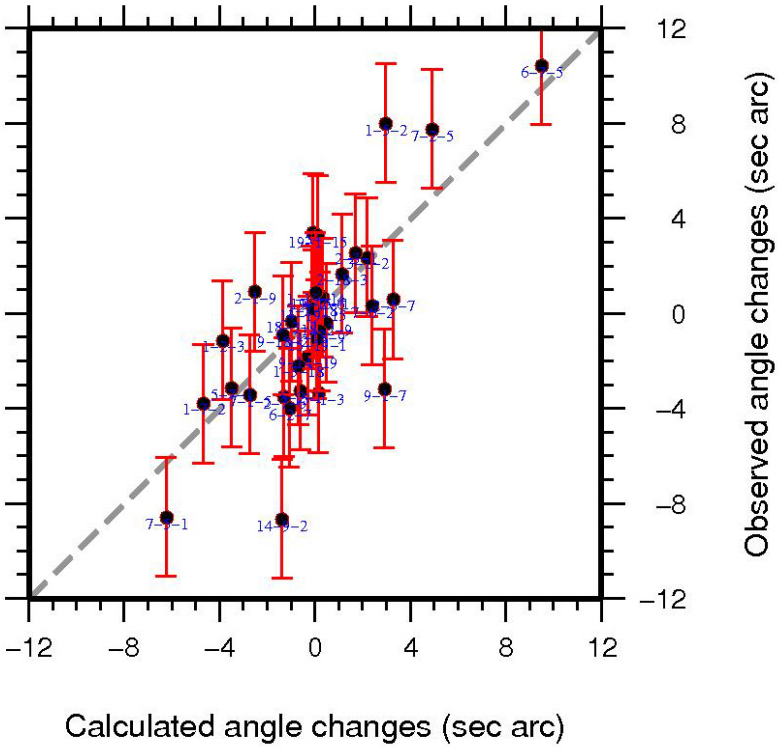

Figure 5.15 Correlation between observed and best-fit modelled angle changes. The red bars represent the associated 1 sigma error.

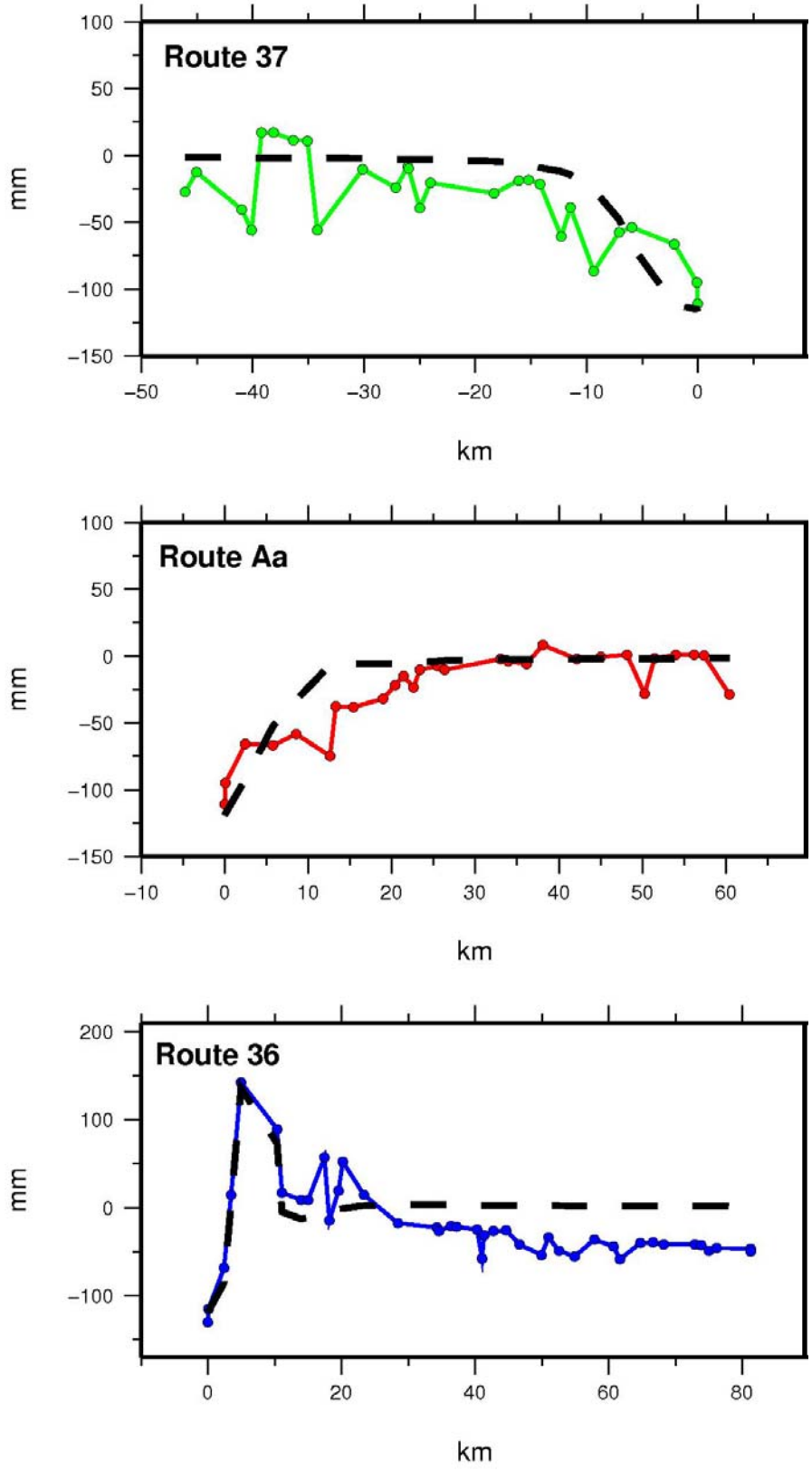

Figure 5.16 The optimal model fit to the leveling data along routes 37 (a), Aa (b) and 36 (c). The continuous lines in represent the observed elevation changes, the coarse dashed lines represent the vertical displacement of the optimal model and the thin dashed lined are the vertical component of the interseismic deformation field.

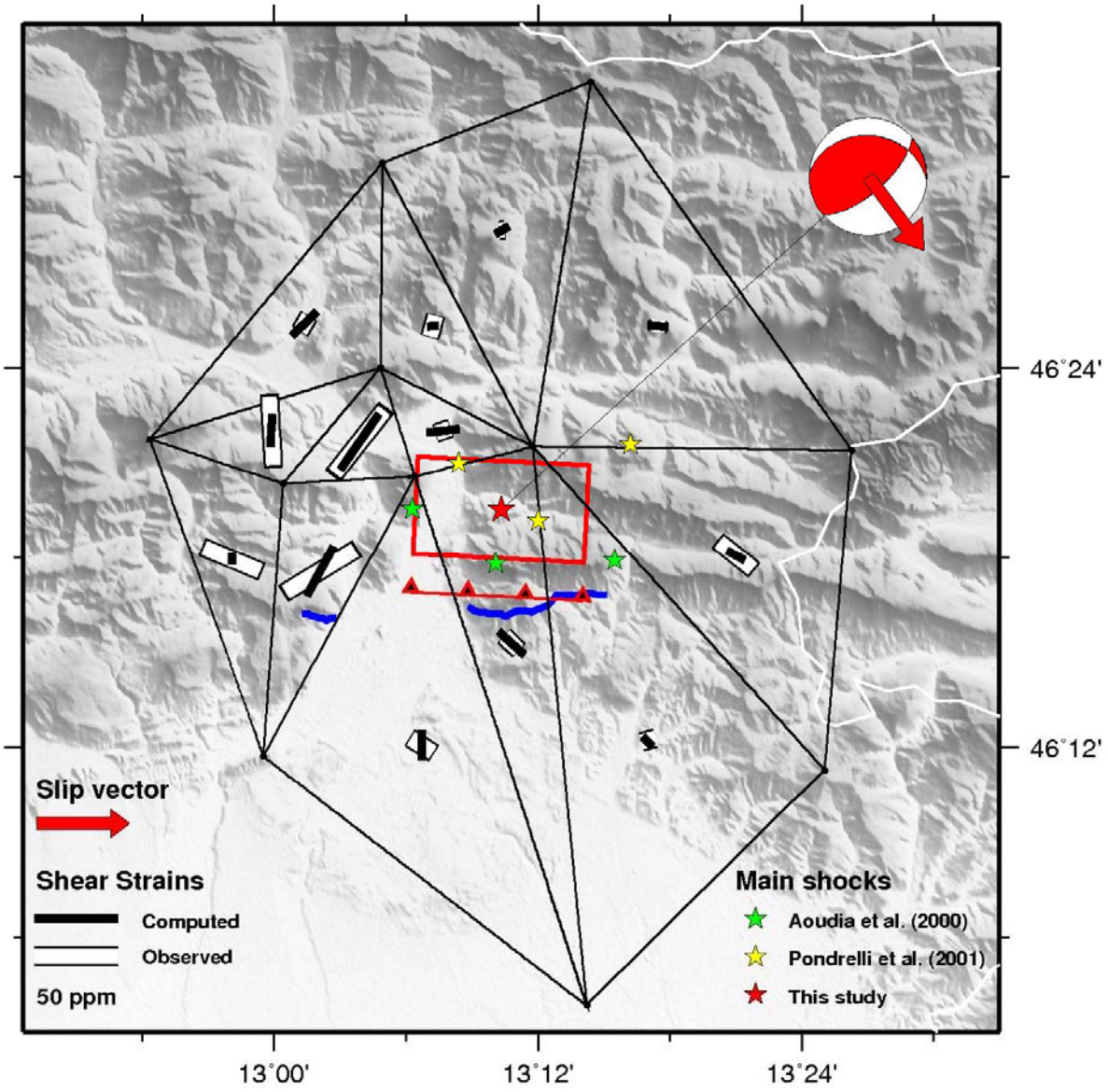

Figure 5.17 Trigonometrical stations remeasured in epicentral area following the 1976 Friuli earthquake. Both observed and predicted angle changes are displayed as bar whose orientations are parallel to the most compressional principal strain (calculated in the related triangles) and whose lengths are proportional to the shear strain [*Frank, 1966*] $\gamma_{tot} = \left(\gamma_1^{\,2} + \gamma_2^{\,2}\right)^{1/2}$, where $\gamma_1 = \delta u / \delta x - \delta v / \delta y$, $\gamma_2 = \delta u / \delta y + \delta v / \delta x$ and u, v are components of displacement in the easterly (x) and northerly (y) directions. White bars are calculated for the triangulation angle change observations, and black bars how strain calculated for the optimal fault model. Red rectangle indicates surface projection of the optimal fault model while red line with filled triangles shows the surface intersection of the continuation of this plane to the surface. The green and yellow stars indicate the epicenters of the main shocks of the 1976 Friuli earthquake according to different authors [*Aoudia et al., 2000; Pondrelli et al., 2001*], while the red star represents the optimal fault solution. Blue thick lines are surface breaks (after *Bosi et al.* [*1976*]).

In summary the main characteristics of the leveling and triangulation data are fit by the optimal single fault model, that is, these results are consistent at the first order with a progressive rupture of a single fault system (e.g., as proposed by *Aoudia et al.* [*2000*]). As it will be discuss later, the single fault plane solution of this study differs from that of *Aoudia et al.* [*2000*] because the latter is located more to the south. A single uniform-slip fault model seems to not reproduce some minor complexities of the observations. In fact the single fault plane model does not reproduce some minor features of the leveling deformation field (Figure 5.16) along the Route 36 leveling line south of the main peak of observed uplift.

5.5.1 Confidence intervals of estimated model parameters

To estimate the individual confidence intervals associated with the inverted model parameters, a Monte-Carlo simulation technique (see Chapter IV) [e.g., *Press et al., 1992; Wright et al., 1999; Sudhaus & Jonsson, 2007*] was performed. The 2000 minimum-misfit solutions that have been determined, each using the SA, were obtained using different input data sets, each one derived from the original displacements by adding synthetic realizations of data noise to the original data. In particular, the displacements were randomly perturbed in a normal distribution about their original values using an a-priori standard deviation of 10 mm for leveling data and 2.5 arc sec for angle measurements.

			Best-fit model	
Parameter	**Min**	**Max**	**Optimal model parameter**	**1 sigma error**
X[a] (km)	-20	20	-2.3	2.8
Y[a] (km)	-20	20	0.0	1.2
Depth (km)	0	10	1.3	0.7
Length (km)	1	30	10.0	5.2
Width (km)	1	20	6.6	1.6
Dip (deg)	1	60	30.0	9.6
Strike (deg)	220	320	273.3	24.4
Dip-slip (cm)	0	300	144.7	68.5
Strike-slip (cm)	-300	300	-120.7	88.2

Table 5.2 Source parameters of the 1976 Friuli earthquake from inversion of geodetic data. [a] X and Y represent the kilometric coordinates of a point of the fault, particularly this point is defined as the middle point of the upper edge of the fault plane.

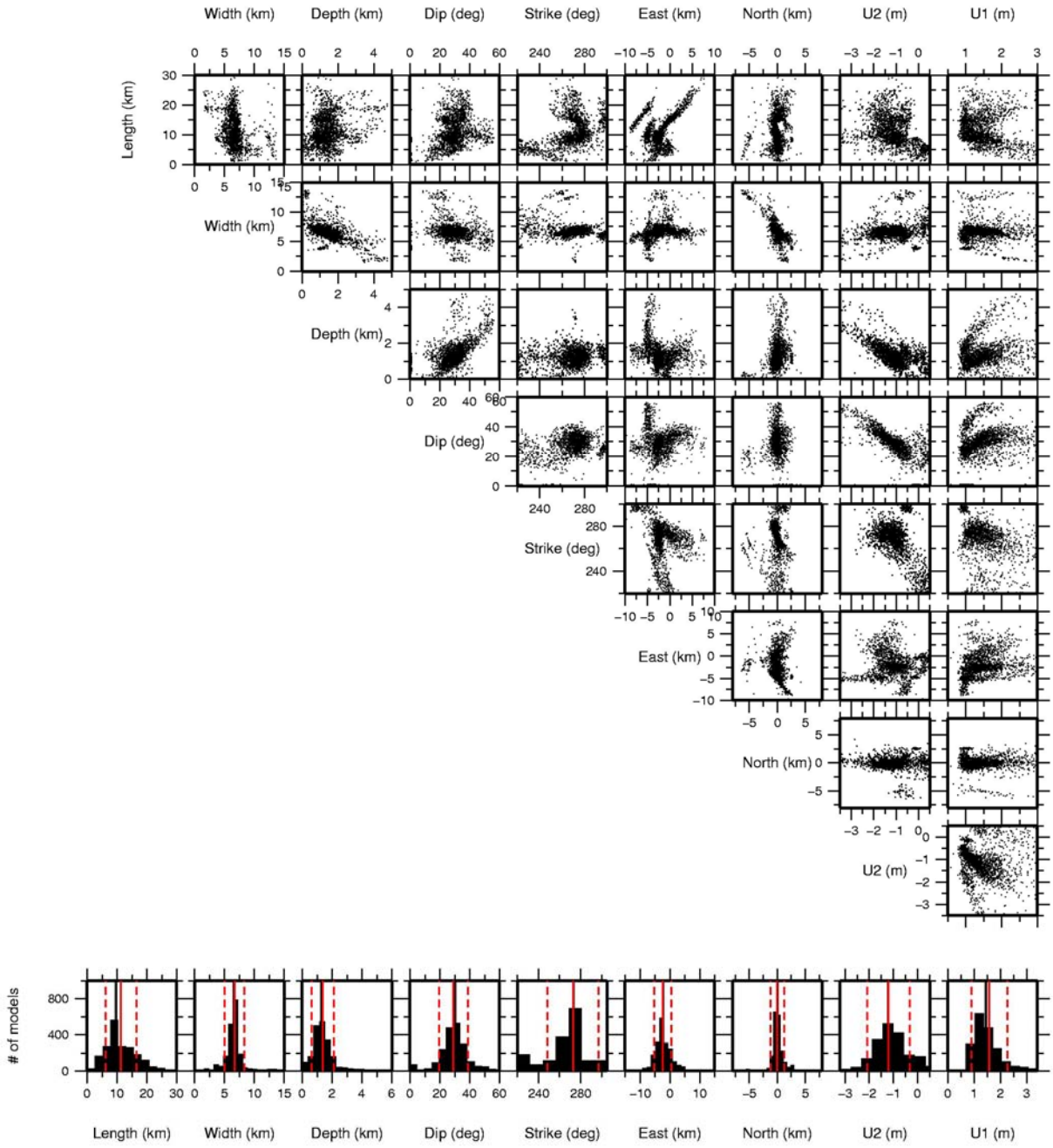

Figure 5.18 A covariance scatter plot for the fault from the optimal Friuli model. The bottom row shows the 1-D a posteriori distribution for the 9 model parameters. The vertical dashed lines in the bottom row bracket the 1σ confidence intervals. The other rows represent the correlations between parameters pair.

The results of many optimization runs using these modified input data provide a distribution of source models which outline the confidence intervals of the optimum source model parameters. The 1σ errors in Table 5.2 reflect the distribution of solutions found (Figure 5.18).

5.5.2 Results and Discussion

The main shock of the 1976 Friuli earthquake sequence (6 May 1976) has been attributed both to the compressive structure affecting the Buia-Tricesimo area [*Aoudia et a., 2000; Peruzza et al., 2002; Poli et al., 2002*], characterized by a Dinaric (NW-SE) trend and to the activation of the Periadriatic thrust [*Bosi et al., 1976; Pondrelli et al., 2001*], characterized by an Alpine (E-W) trend. Geological evidence of surface breaks were immediately identified after the main shock in proximity of the Periadriatic thrust. These features were interpreted by *Martinis and Cavallin* [*1978*] as possibly being the result of landslides, whereas by *Bosi et al.* [*1976*] as surface faulting because of their continuity over different terrains. The previous geodetic source solutions [*Arca et al., 1985; Briole et al., 1986*] modelled the observed deformation by means of three different faults, with the largest ones associated with the 6 May 1976 event and defined by a rectangular fault plane ENE-WSW trending located about 5 km south of Gemona.

The optimal uniform–slip elastic dislocation model (Figure 5.17) consists of a 30° north-dipping shallow (depth 1.30±0.75 km) fault plane with azimuth of 273° and accommodating reverse dextral slip of about 1.8 m (in particular, ~1.5 m of reverse slip and ~1.2 m of strike slip). Some model parameters are quite poorly constrained by the data set (Table 5.2 and Figure 5.18), probably due to the geometry distribution of the data and/or to the limited numbers of available geodetic observations. Other model parameters are instead well constrained by the used data set. In particular the latitude of the fault and the width, depth and dip of the plane are well constrained by the leveling leveling data, since the upper edge of the fault must lie beneath the position of the peak uplift. In fact the asymmetry of the vertical motion depends on the dip of the fault and moreover the uplift and subsidence die away with the distance from the fault on a length-scale that depends on the down-dip fault width. So the clear coseismic subsidence of the line 37, Aa and 36 excludes a fault solution that extends more to the North of the area where the three lines joint together. The peak of maximum uplift also constrains the position of the fault to the South. The geodetic data set then exclude the source solution of *Aoudia et al.* [*2000*], *Peruzza et al.* [*2002*] and *Poli et al.* [*2002*] that considers the Susans-Tricesimo thrust as the May 6 event. The best-fit source model is then more consistent with the solution of *Pondrelli et al.* [*2001*], which proposed the activation of other thrusts located more to the North of the Susans-Tricesimo thrust, probably on Periadriatic related thrust faults (Figure 5.1). This can be seen also by projecting the optimal fault plane solution along a section across the eastern Alps (Figure 5.19).

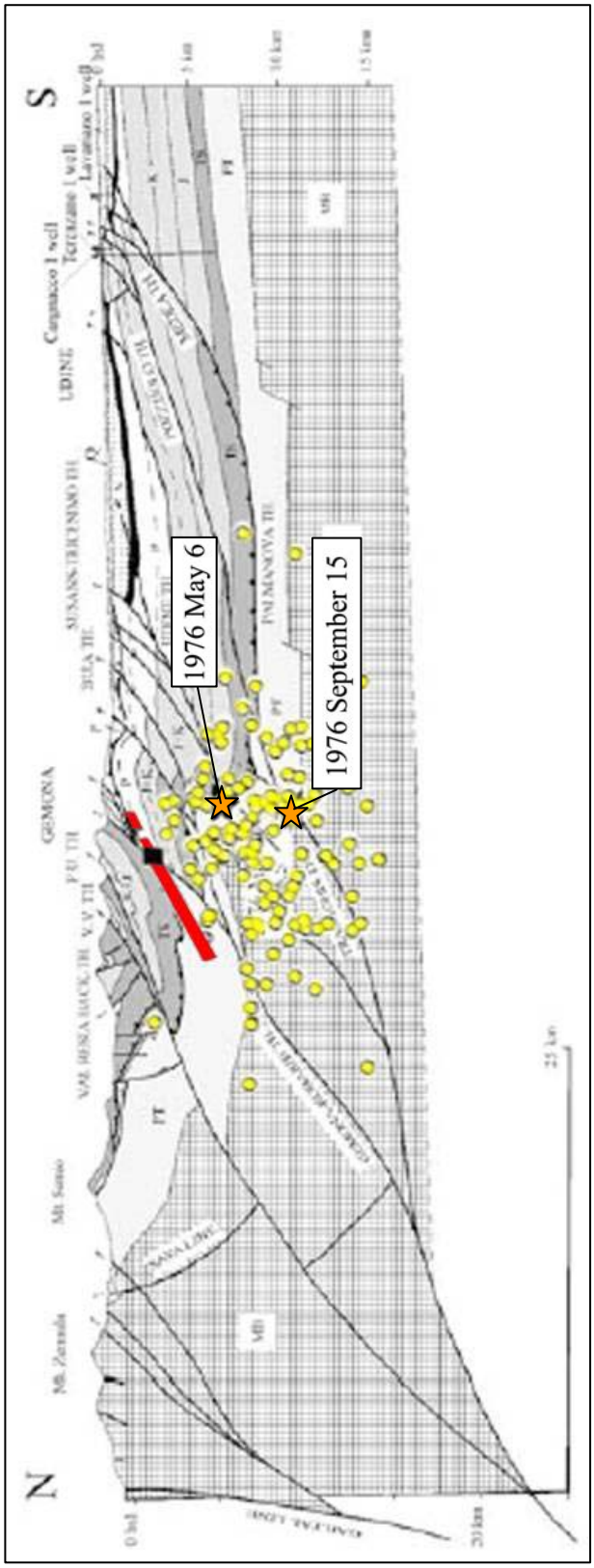

Figure 5.19 Geological cross section across the Eastern Alps. In red is showed the optimal single fault plane solution. The yellow circles represent the aftershocks of the 1976 Friuli sequence while the stars indicate the main shocks [*Poli et al., 2002*]. Modified from *Galadini et al.* [*2005*].

The hypocentral location and inferred fault plane of the main event are more consistent with the activation of Periadriatic overthrusts and other related thrust faults as the Gemona-Kobarid thrust (Figure 5.19). The epicentral location appears not consistent with the know damage distribution (located more the south) [*Monachesi and Stucchim 1998*], but it is known that the area of maximum damage can differ from the epicentre due to local site amplification on alluvial deposits, and in fact this area is almost completely covered by a thick layer of quaternary sediments [*Venturini et al., 2004*]. The surface projection of the best-model solution is consistent with the locations of the main shocks of the sequence proposed by *Pondrelli et al.* [*2001*] (focal depth between 6-10 km), but the best-fit solution proposed in this Thesis shows a shallower focal depth (max ~5 km). It is important to remark that the focal depths computed by *Pondrelli et al.* [*2001*] were not well constrained by the available data set used in that study. The surface projection of the optimal solution is also in agreement with the surface breaks which has been observed shortly after the May 6 main shock along the Periadriatic thrust by *Bosi et al.* [*1976*] (Figure 5.17).

The best-fit geodetic moment (M_0=2.9*10^{18} Nm) is in good agreement with the body wave solution of *Cipar* [*1980*] but is underestimated respect to the solution of *Aoudia et al.* [*2000*] and *Pondrelli et al.* [*2001*]. Finally, the azimuth of the coseismic slip vector in the best-fit source model is consistent with the seismological solutions and with the average relative plate motion orientation based on continuous GPS data [e.g., *D'Agostino et al., 2005*]. Furthermore, the optimal single fault model, relative to the creeping fault of *D'Agostino et al.* [*2005*], is located in the shallow part of the area affected by intense microseismicity, at the base of the locked fault zone, where 1976-like seismic events can nucleate (Figure 5.20).

In summary the main characteristics of the leveling and triangulation data are fit by the optimal model, however single uniform-slip fault model seems to not reproduce the complexity of the observations. In fact the single fault plane model does not reproduce some minor features of the leveling deformation field.

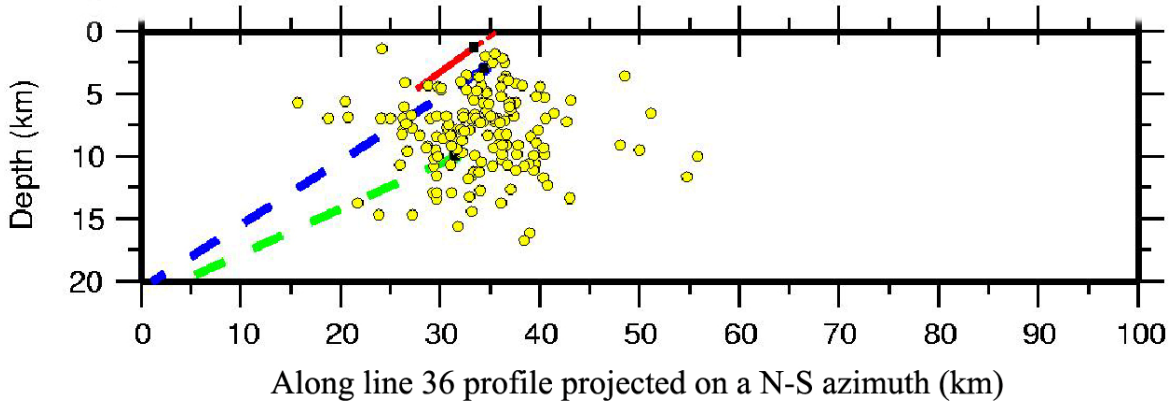

Figure 5.20 Model geometry and seismicity projected along a N-S profile. Yellow circles are the aftershock of the 1976 Friuli earthquake sequence (from *Poli et al.* [*2002*]). The optimal single fault model is depicted in red, while the two possible interseismic dislocation planes computed from GPS observations are in blue and green (from *D'Agostino et al.* [*2005*]).

5.6 Secondary faulting or postseismic deformation ?

The observed vertical deformation recorded by the leveling measurements between 1952 and 1977, after the 1976 Friuli earthquake, seems to contain other tectonic signals (specially along route 36), much larger than the inferred interseismic deformation over the considered time period, and that are not modelled by the optimal single fault plane solution (Figure 5.16). In particular, along route 36 (Figure 5.21) about 10 km southward of the strong modelled uplift, another smaller uplift signal is observed, which is not modelled by the single fault plane solution. Other possible processes which can contribute to these observed signals include secondary faulting and/or postseismic deformation (e.g., *Fielding et al.* [*2004*], *Mahsas et al.* [*2007*]). In fact, after the main shock some large aftershocks (M >5) took place, and these events may have contributed to the geodetic deformation. Furthermore, because the geodetic measurements were made about 16 months later the main event, the geodetic signal may be also contaminated by postseismic deformation (e.g., afterslip, viscoelastic relaxation of the asthenosphere).

Regarding the first hypothesis, the stress imparted by a blind thrust earthquake to the overlying crust is often relieved by secondary surface faults [e.g., *Lin and Stein, 2004*]. However, for testing the hypothesis of secondary faulting, a second formal inversion for an elastic dislocation fitting the residual signal, is not viable, due to the very poor resolution of the "residual" data with respect to almost all the model parameters. In fact, this strong residual

signal is present only along the N-S trending leveling route 36 (Figure 5.21), and thus, one leveling line alone cannot be used to constrain, e.g., the azimuth and/or the length of this possible second fault plane.

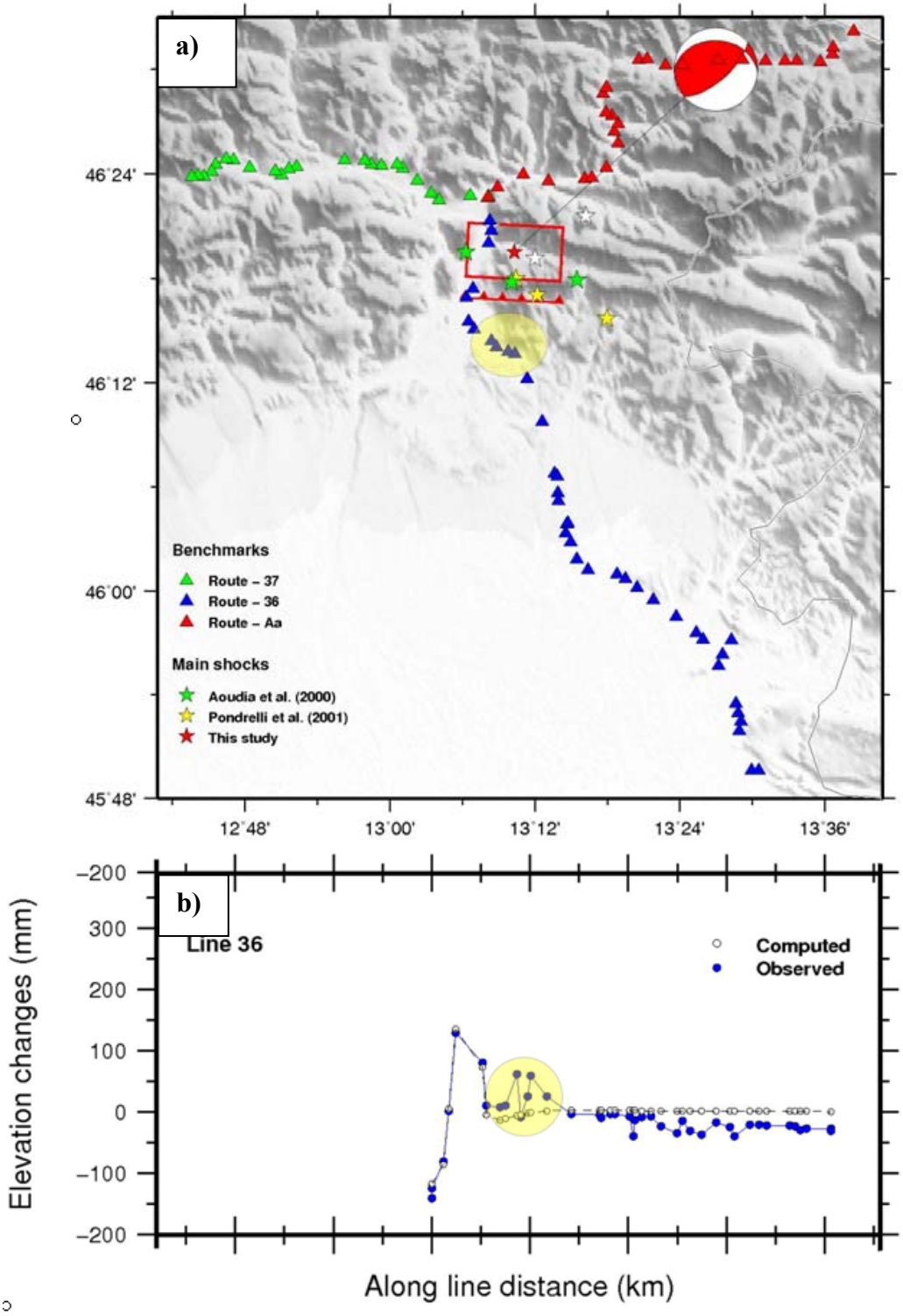

Figure 5.21 (a) Map of the studied area: the leveling routes are showed as well as optimal fault model (box) and previous epicentral estimates (stars). The transparent yellow circles indicates the positions of the residual signal not fitted by the optimal single fault model. (b) Observed and elevation changes along Route 36. Also remarked (in yellow) the residual signal.

Despite these limitations, some forward models have been tentatively made, by taking in account some a priori information. In fact, as seen in paragraph 5.1, the study area is characterized by the coexistence of various thrust systems (Figure 5.1 and 5.22), and southward of the computed optimal single fault plane solution, other shallower thrust systems have been recognized [e.g., *Amato et al., 1976; Galadini et al., 2005*]. In particular, the observed residual signal occurs across the surface trace of the Buia-Tricesimo thrust system. This geological a priori information has been used to fix some characteristics of the second plane dislocation.

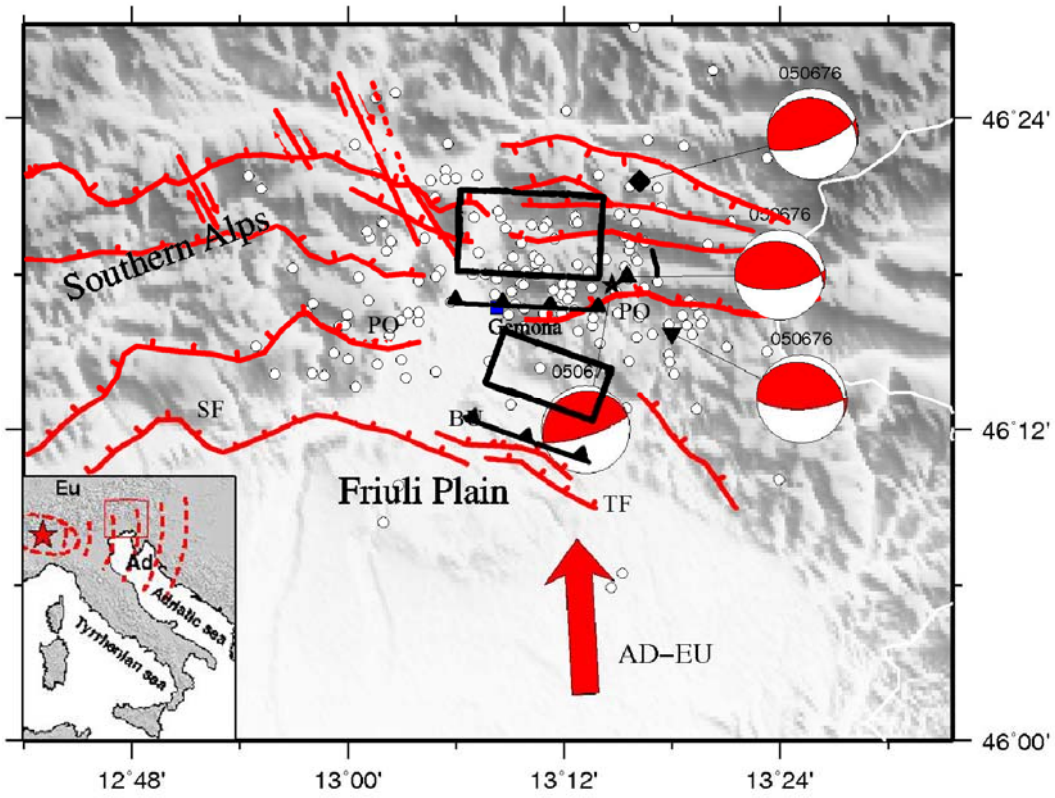

Figure 5.22 Tectonic setting of the study area. The boxes indicate the optimal solution and the secondary dislocation plane. For abbreviations see Figure 5.1.

Thus, fixing some model parameters, a second fault plane that fits the residual signal has been tentatively searched, constraining the models to be roughly correspondent to some mapped thrust (e.g., Buia-Tricesimo thrust). The resulting secondary fault plane (Figure 5.22) fits pretty well the residual leveling signal (Figure 5.23), while the computed angle changes remain unchanged by the adding of this secondary dislocation.

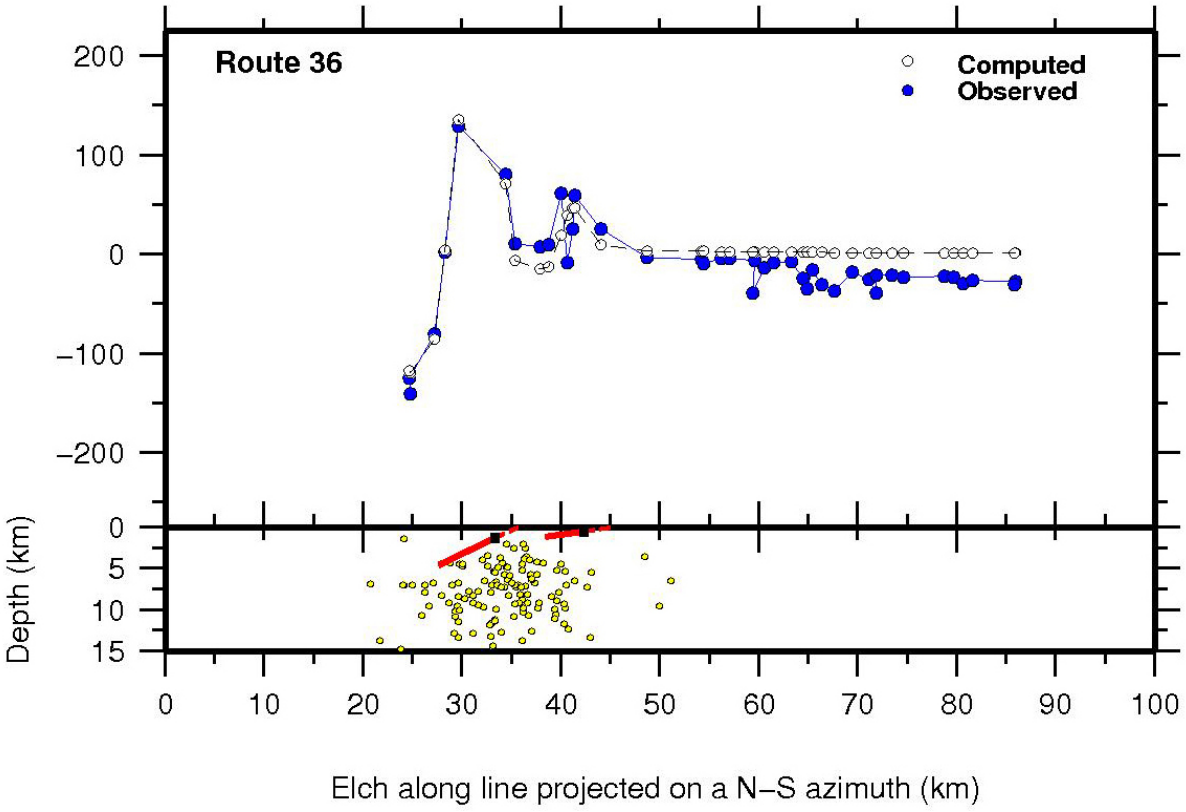

Figure 5.23 Observed (blue circles) and computed (white circle) elevation changes for the Route 36, plotted along a N-S direction. In the panel below the relative dislocation planes are plotted together with the hypocentral solutions of *Poli et al.* [*2002*].

5.7 Conclusions

Despite the 1976 Friuli earthquake has been one of the most damaging events recorded in Northern Italy, debate still persists about the reactivated geological structures [e.g., *Aoudia et al., 2000; Pondrelli et al.,2001; Peruzza et al., 2002; Galadini et al., 2005*]. In fact the main shock has been attributed both to the compressive structure affecting the Buia-Tricesimo area [*Aoudia et al., 2000; Peruzza et al., 2002; Poli et al., 2002*] and to the activation of the northward Periadriatic thrust [*Bosi et al., 1976; Pondrelli et al., 2001*] (Figure 5.1). In this Thesis, all the geodetic displacements available, that consists of first to third order triangulation measurements plus vertical displacements from leveling were jointly inverted to retrieve a source model for the 1976 Friuli earthquake. The computed optimal uniform–slip elastic dislocation model consists of a single 30° north-dipping shallow (depth 1.30±0.75 km) fault plane with azimuth of 273° and accommodating reverse dextral slip of about 1.8 m

(Figure 5.17), consistently with seismological information. The hypocentral location and inferred fault plane of the main event are then consistent with the activation of Periadriatic overthrusts or other related thrust faults as the Gemona-Kobarid thrust (Figure 5.19). The main characteristics of the leveling and triangulation data are fit by the optimal single fault model, that is, these results are consistent at the first order with a progressive rupture of a single fault system. A single uniform-slip fault model seems to not reproduce minor complexity of the observations, and some large residual signals that are not modelled by the optimal single fault plane solution, were observed. By assuming movements along some mapped thrust located southward of the inferred optimal single plane solution, the residual signal has been successfully modelled. In summary, the inversion results presented in this Thesis, are consistent with the activation of some Periadriatic related thrust for the main events of the sequence, and with a minor importance of the southward thrust systems of the middle Tagliamento plain.

Chapter VI

General Conclusions

6.1 General conclusions

The systematic analysis of geodetic measurements in actively deforming regions currently represents one of the most important tool in the study of crustal deformation over different temporal scales. Although during the last decades geodetic methods and technology to measure active deformation of the Earth's crust have tremendously improved, particularly the space geodetic data, the studies of tectonic deformation can still take advantage of classical terrestrial measurements, spanning long time of observations. In fact, repeated terrestrial geodetic observations have been successfully used to give estimates of tectonic deformation in several parts of the world, providing detailed information on ground displacements, such as how active faults move in earthquakes [e.g. *Lin & Stein, 1989; Arnadottir & Segall, 1994; Yu & Segall, 1996; Thatcher et al., 1997; King & Thatcher, 1998; Bilham & England, 2001; Nyst et al., 2006*] as well as refined estimates of the long-term accumulation of elastic strain [e.g. *Harada & Shimura, 1979; Thatcher, 1979; Savage et al., 1981; Savage, 1983; Walcott, 1984; King et al., 1987; Feigl et al., 1990; Davies et al., 1997; Hunstad et al., 2003*] over time spans of decades to a century. The subject of this thesis was to use terrestrial geodetic measurements to investigate crustal deformation, particularly related to two different active tectonic regions of the Italian peninsula where some problems still remains poorly understood: the Messina Straits and the Friuli area.

6.1.1 The Messina Straits

The aim of this Thesis was to use a set of historical terrestrial geodetic observations, particularly triangulation measurements that were never elaborated in an homogeneous way, to investigate the crustal deformation accumulated by this boundary zone in relationship with the boundary kinematic condition imposed by the relative motion between the two different domains.

To determine the rates of deformation the observations were processed utilizing an extended version of the *Frank*'s method that permits to adjust all of the available observations simultaneously. The average annual shear strain rates for the time period between 1971 and 2004 are γ_1 = 113.89 ± 54.96 nanostrain/yr and γ_2 = -23.38 ± 48.71 nanostrain/yr, with the orientation of the most extensional strain (θ) at N140.80° ± 19.55°E, indicating that the triangulation measurements are consistent with an active NW-SE extension across the

Messina Straits. The orientation of θ agree well with GPS deformation estimates, calculated over shorter time interval, and is consistent with previous preliminary GPS estimates [*D'Agostino and Selvaggi, 2004; Serpelloni et al., 2005*] and is also similar to the direction of the 1908 (M_W 7.1) earthquake slip vector. We infer that the measured strain rate is due to acive extension across the Messina Straits, corresponding to a relative extension rate ranges between < 1mm/yr and up to 2 mm/yr. These results are consistent with the hypothesis that the Messina Straits is an important active geological boundary between the Sicilian and the Calabrian domains and support previous preliminary GPS-based estimates of strain rates across the Straits. Finally, the preliminary dislocation modelling has shown that, although the current geodetic measurements do not resolve the geometry of the dislocation models, they solve well the rate of interseismic strain accumulation across the Messina Straits and give useful information about the locking the depth of the shear zone.

6.1.2 The 1976 Friuli earthquake

The second region where crustal deformation (on different temporal scale) has been analyzed is the Friuli region (NE Italy). This area was struck on 1976 by a sequence of moderate-to large earthquakes. Despite the 1976 Friuli earthquake has been one of the most damaging events ever recorded in Northern Italy, causing many victims and destroying large parts of several nearby localities, debate still persists about the reactivated geological structures [e.g. *Aoudia et al., 2000; Pondrelli et al., 2001; Peruzza et al., 2002; Galadini et al., 2005*]. In this thesis, for the first time, all the geodetic displacements available, that consists of first, second and third order triangulation measurements plus vertical displacements from double run high-precision leveling, were inverted to retrieve a source model for the main event that optimally fits the set of coseismic geodetic measurements. By means of the optimal source model we further tried to understand which fault system has been reactivated during this sequence. The computed optimal uniform–slip elastic dislocation model consists of a 30° north-dipping shallow (depth 1.30±0.75 km) fault plane with azimuth of 273° and accommodating reverse dextral slip of about 1.8 m. The hypocentral location and inferred fault plane of the main event are then consistent with the activation of Periadriatic overthrusts or other related thrust faults as the Gemona-Kobarid thrust. The main characteristics of the leveling and triangulation data are fit by the optimal single fault model, that is, these results are consistent at the first order with a progressive rupture of a single fault

system. However, single uniform-slip fault model seems to not reproduce the complexity of the observations, and some large residual signals that are not modelled by the optimal fault plane solution, were observed. By assuming movements along some mapped thrust located southward of the inferred optimal single plane solution, the residual signal has been successfully modelled. In summary, the inversion results presented in this Thesis, are consistent with the activation of some Periadriatic related thrust for the main events of the sequence, and with a minor importance of the southward thrust systems of the middle Tagliamento plain.

Bibliography

Achilli, V., Baldi P., Zerbini S., Broccio F., Cagnetti V., Marsan P., Gubellini A. & Ungendoli M., 1988. Comparison between GPS and round based distance measurements in the Messina Straits area, *Boll. Geof. Teor. Appl.,* **30**, 361 – 369.

Allman, J.S. & Bennett G.G., 1966. Angles and directions, *Survey Review,* **139**, 219 – 228.

Altamini, Z., Collilieux X., Legrand J., Garayt B. & Boucher C., 2007. ITFR2005: A new release of the International Terrestrial Reference Frame based on time series of station positions and Earth Orientation Parameters, *J. Geophys. Res.,* **112**, B09401, doi:10.1029/2007JB004949.

Amato, A., Barnaba P.F, Finetti I., Groppi G., Martinis B. & Muezzin A., 1976. Geodynamic outline and seismicity of Friuli Veneta Julia region, *Boll. Geof. Teor. Appl.,* **18**, 217-256.

Amato, A., Alessandrini B., Cimini G., Frepoli A. & Selvaggi G., 1993. Active and remnant subducted slabs beneath Italy: evidence from aseismic tomography and seismicity, *Ann. Geofis.,* **36**, 201 – 214.

Amoruso, A., Crescentini L. & Scarpa R., 1998. Inversion of source parameters from near- and far-field observations: An application to the 1915 Fucino earthquake, central Apennines, Italy, *J. Geophys. Res.,* **103**, 29989 – 29999.

Amoruso, A., Crescentini L. & Scarpa R., 2002. Source parameters of the 1908 Messina Straits, Italy, earthquake from geodetic and seismic data, *J. Geophys. Res.,* **107**, 2080, doi:10.1029/2001JB000434.

Anderson, H. & Jackson J., 1987. Active tectonics in the Adriatic region, *Geophys. J. R. Astron. Soc.,* **91**, 937-983.

Anzidei, M., Baldi P., Casula G., Galvani A., Mantovani E., Pesci A., Riguzzi F. & Serpelloni E., 2001. Insights into present-day crustal motion in the central Mediterranean area from GPS surveys, *Geophys. J. Int.,* **146**, 98 – 110.

Aoki, Y., Segall P., Kato T., Cervelli P. & Shimada S., 1999. Upward dike migration during the 1997 seismic swarm off the Izu Peninsula, Japan, from inversion of deformation data, *Science,* **286**, 927 – 930.

Aoudia, A., Saraó A., Bukchin B. & Suhadolc P., 2000. The 1976 Friuli (NE Italy) thrust faulting earthquake: A reappraisal 23 years later, *Geophys. Res. Lett.,* **27**, 573–576.

Arca, S., Pierozzi M., Giorgetti G. & Marchioni A., 1986. Controllo geodetico periodico dello Stretto di Messina – Misure eseguite nel 1986 dall'IGMI, *Boll. Geod. Sci. Aff.,* **4**, 345 – 359.

Argus, D. F., Gordon R. G., DeMets C. & Stein S, 1989. Closure of the Africa-Eurasia-North American plate motion circuit and tectonics of the Gloria fault, *J. Geophys. Res.,* **94**, 5585 – 5602.

Arnadottir, T. & Segall P., 1994. The 1989 Loma Prieta earthquake imaged from inversion of geodetic data, *J. Geophys. Res.,* **99**, 21835 – 21855.

Arnadottir, T., Segall P. & Matthews M., 1992. Resolving the discrepancy between geodetic and seismic fault models for the 1989 Loma Prieta, California, earthquake, *Bull. Seismol. Soc. Am.,* **82**, 2248 – 2255.

Bagh, S., Chiaraluce L., De Gori P., Moretti M., Govoni A., Chiarabba C., Di Bartolomeo P. & Romanelli M., 2007. Background seismicity in the Central Apennines of Italy: the Abruzzo region case of study, *Tectonophysics,* **444**, 80 – 92.

Baldi, P., Achilli V., Mulargia F. & Broccio F., 1983. Geodetic surveys in Messina Straits area, *Bull. Geod.,* **57**, 283 – 293.

Barbano, M.S., Kind R. & Zonno G., 1985. Focal parameters of some Friuli earthquakes (1976-1979) using complete theoretical seismograms, *J. Geophys.,* **58**, 175-182.

Basu, A. & Frazer L.N., 1990. Rapid determination of critical temperature in simulated annealing inversion, *Science,* **249**, 1409 – 1412.

Bencini, P., 1975. Geodetic Measurements made by Istituto Geografico Militare in the Strait of Messina area, *Tectonophysics,* **29**, 331 – 337.

Bencini, P., Dermanis A., Livieratos E. & Rossikopoulos D., 1982. Crustal deformation at the Friuli area from discrete and continuous geodetic prediction techniques, *Bull. Geod. Sci. Aff.,* **41**, 137-148.

Berg, B., 1993. Locatine global minima in optimization problems by a random-cost approach, *Nature,* **361**, 708 – 710.

Bilham, R. & England P., 2001. Plateao 'pop-up' in the great 1897 Assam earthquake, *Nature,* **410**, 806 – 809.

Bomford, G.,1980. *Geodesy*, Claredon, Oxford, p. 855.

Boschi, E., Guidiboni E., Ferrari G., Valensise G. & Gasperini P. (eds.) 1997. *Catalogo dei forti terremoti in Italia dal 461 a.C. al 1990, 2*, ING-SGA, Bologna, p. 644.

Boschi, E., Pantosti D. & Valensise G., 1989. Modello di sorgente per il terremoto di Messina del 1908 ed evoluzione recente dell'area dello stretto, *paper presented at Atti 89th GNDT Workshop, Cons. Naz. Delle Ric., Rome.*

Bosi, C., Camponeschi B. & Giglio G., 1976. Indizi di possibili movimenti lungo faglie in occasione del terremoto del Friuli del 6 Maggio 1976, *Boll. Soc. Geol. It.,* 95, 803 – 830.

Bottari, A., Carapezza E., Carapezza M., Carveni P., Cefali F., Lo Giudice E. & Pandolfo C., 1986. The 1908 Messina Strait earthquake in the regional geostructural framework, *Journal of Geodynamics,* **5**, 275 – 302.

Bressan, G., Bragato P.L. & Venturini C., 2003. Stress and strain tensors based on focal mechanisms in the seismotectonic framework of the Friuli-Venezia Giulia Region (North-eastern Italy), *Bull. Seism. Soc. of Am.,* **3**, 1280 – 1297.

Briole, P., De Natale G., Gaulon R., Pingue F. & Scarpa R., 1986. Inversion of geodetic data and seismicity associated with the Friuli earthquake sequence (1976-1977), *Annales Geophysicae,* **4**, 481–492.

Capuano, P., De Natale G., Gasperini P., Pingue F. & Scarpa R., 1988. A model for the 1908 Messina Straits (Italy) earthquake by inversion of levelling data, *Bull. Seism. Soc. Am.,* **78**, 1930 – 1947.

Caputo, M., Pieri L., Barbarella M., Gubellini A., Russo P. & Console R., 1981. Geophysical geodetic observations in the Messina Straits, *Tectonophysics,* **74**, 147 – 154.

Chang, S.-J., Baag C.-E. & Langston C.A., 2004. Joint analysis of teleseismicreceiver functions and surface wave dispersion using the genetic algorithm, *Bull. Seism. Soc. Am.,* **94**, 691 – 704.

Chiarabba, C., Jovane L. & Di Stefano R., 2005. A new view of Italian seismicity, using 20 years of instrumental recordings, *Tectonophysics,* **395**, 251 – 268.

Cipar, J., 1981. Broadband time domain modelling of earthquakes from Friuli, Italy, *Bull. Seism. Soc. Am.,* **71**, 1215 – 1231.

Corana, A., Marchesi M., Martini C. & Ridella S., 1987. Minimizing multimodal functions of continuous variables with the "Simulated Annealing" algorithm, *ACM Trans. Math. Softw.,* **13**, 262 – 280.

Cross, P.A., 1990. *Advanced least squares applied to position-fixing*, Working Paper No. 6, Polytechnic of East London, Department of Land Surveying, p. 205.

D'Agostino, N. & Selvaggi G., 2004. Crustal motion along the Eurasia-Nubia plate boundary in the Calabrian Arc and Sicily and active extension in the Messina Straits fro GPS measurements, *J. Geophys. Res.,* **109**, B11402, doi:10.1029/2004JB002998.

D'Agostino, N., Cheloni D., Mantenuto S., Selvaggi G., Michelini A. & Zuliani D., 2005. Strain accumulation in the southern Alps (NE Italy) and deformation at the northeastern boundary of Adria observed by CGPS, *Geophys. Res. Lett.,* **32**, L19306, doi:10.1029/2005GL024266.

Davies, R., England P., Parsons B., Billiris H., Paradissis D. & Veis G., 1997. Geodetic strain of Greece in the interval 1892-1992, *J. Geophys. Res.,* **102**, 24571 – 24588.

De Natale, G. & Pingue F., 1991. A variable slip fault model for the 1908 Messina Straits (Italy) earthquake, by inversion of levelling data, *Geophys. J. Int.,* **104**, 73 – 84.

DeMets, C., Gordon R.G., Argus D.F. & Stein S., 1994. Effect of recent revisions to the geomagnetic reversals time scale on estimates of current plate motions, *Geophys. Res. Lett.,* **21**, 2191 – 2194.

Dixon, T.H., 1991. An introduction to the Global Positioning System and some geological applications, *Rev. Geoph.,* **29/2**, 249 – 276.

Doglioni, C. & Bosellini A., 1987. Eoalpine and Mesoalpine tectonics in the southern Alps, *Geol. Rundsch.,* **76/3**, 735 – 754.

Efron, B. & Tibshirani R.J., 1993. An introduction to the Bootstrap, *Chapman and Hall, New York,* p. 436.

Engdahl, E.R., van der Hilst R. & Buland R., 1998. Global teleseismic earthquake relocation with improved travel times and procedures for depth determination, *Bull. Seismol. Soc. Am.,* **88**, 722 – 743.

Faccenna, C., Becker T. W., Lucente F. P., Jolivet L. & Rossetti F., 2001. History of subduction and back-arc extension in the central Mediterranean, *Geophys. J. Int.,* **145**, 809 – 820.

Feigl, K. L., King R.W. & Jordan T.H., 1990. Geodetic measurements of tectonic deformation in the Santa Maria Fold and Thrust Belt, California, *J. Geophys. Res.,* **95**, 2679 – 2699.

Feigl, K.L., Sergent A. & Jacq D., 1995. Estimation of an earthquake focal mechanism from a satellite radar interferogram: Application to the December 4, 1992 landers aftershock, *Geophys. Resl. Lett.,* **22**, 1037 – 1040.

Fielding, E.J., Wright T.J., Muller J., Parsons B.E. & Walker R., 2004. Aseismic deformation of a fold-and-thrust belt imaged by synthetic aperture radar interferometry near Shahdad, southeast Iran, *Geology*, **32**, 577 – 580.

Finetti, I., Giorgetti F., Haessler H., Hoang T.P., Slejko D. & Wittlinger G., 1976. Time space epicenter and hypocenter distribution and focal mechanism of 1976 Friuli earthquakes, *Boll. Geofis. Teor. Appl.,* 72, 637 – 655.

Frank, F.C., 1966. Deductions of earth strains from survey data, *Bull. Seism. Soc. Am.,* **56**, 35–42.

Frepoli, A., Selvaggi G., Chiarabba C. & Amato A., 1996. State of stress in the Southern Tyrrhenian subduction zone from fault-plane solutions, *Geophys. J. Int.,* **125**, 879 – 891.

Galadini, F., Poli M.E. & Zanferrari A., 2005. Seismogenic sources potentially responsible for earthquakes with $M \geq 6$ in the eastern Southern Alps (Thiene–Udine sector, NE Italy), *Geophys. J. Int.,* **161**, 739–762.

Ghisetti, F., 1984. Recent deformations and seismogenic source in the Messina Straits (southern Italy), *Tectonophysics,* **109**, 191 – 208.

Giardini, D. & Velonà M., 1988. La sismicità profonda del Mar Tirreno, *Mem. Soc. Geol. Ital.,* **41**, 1079 – 1087.

Gill, P.E., Murray W. & Wright M.H., 1981. *Practical optimization*, Academic, San Diego, Calif., p. 401.

Goffe, W.L., Ferrier G.D. & Rogers J., 1994. Global optimization of statistical functions with simulated annealing, *J. Econometrics,* **60**, 65 – 100.

Guarnieri, P., Di Stefano A., Carbone S., Lentini F. & Del Ben A., 2004. A multidisciplinary approach to the reconstruction of the Quaternary evolution of the Messina Strait area, *Mapping Geology In Italy,* APAT, S.E.L.C.A., Firenze, p. 336.

Gueguen, E., Doglioni C. & Fernandez M., 1998. On the post-25 Ma geodynamic evolution of the western Mediterranean, *Tectonophysics,* **298**, 259 – 269.

Harada, T. & Shimura M., 1979. Horizontal deformation of the crust in Western Japan revealed from first-order triangulation carried out three times, *Tectonophysics,* **52**, 469 – 478.

Hesterberg, T., Moore D.S., Monaghan S., Clipson A. & Epstein R., 2006. *Bootstrap methods and permutation tests, 2nd edition,* W.H. Freeman, N.Y.

Holland, J.H., 1975. Adaptation in natural and artificial systems, *MIT Press.*

Hollenstein, Ch., Kahale H.-G., Geiger A., Jenny S., Goes S. & Giardini D., 2003. New GPS constraints on the Africa-Eurasia plate boundary zone in southern Italy, *Geophys. Res. Lett.,* **30**, No. 18, 1935, doi:10.1029/2003GL017554.

Hunstad, I., Selvaggi G., D'Agostino N., England P., Clarke P. & Pierozzi M., 2003. Geodetic strain in peninsular Italy between 1875 and 2001, *Geophys. Res. Let.,* **30**, No. 4, 1181, doi:10.1029/2002GL016447.

I.G.M.-RG, 1978. *Relazione sui lavori di triangolazione eseguiti nel Friuli dall'Istituto Geografico Militare nell'anno 1977,* Reparto Geodetico, Firenze.

Jackson, J., 2001. Living with earthquakes: know your faults, *J. Earthquake Eng.,* **5**, 5-123.

Jonsson, S., Zebker H., Cervelli P., Segall P., Garbeil H., Mougnis-Mark P. & Rowland S., 1999. A shollow-dipping dike fed the 1995 flank eruption at Fernandina Volcano, Galapagos, observed by satellite radar interferometry, *Geophys. Res. Lett.,* **26**, 1077 – 1080.

Kim, W., Hahm I.-K., Ahn S.J. & Lim D.H., 2006. Determining hypocentral parameters for local earthquakes in 1-D using a genetic algorithm, *Geophys. J. Int.,* **166**, 590 – 600.

King, N.E. & Thatcher W., 1998. The coseismic slip distribution of the 1940 and 1979 Imperial Valley, California, earthquakes and their implications, *J. Geophys. Res.,* **103**, 18069 – 18086.

King, N.E., Segall P. & Prescott W., 1987. Geodetic measurements near Parkfield, California, 1959-1984, *J. Geophys. Res.,* **92**, 2747 – 2766.

Lin, J. & Stein R.S., 1989. Coseismic folding, earthquake recurrence, and the 1987 source mechanism at Whittier Narrows, Los Angeles Basin, California, *J. Geophys. Res.,* **94**, 9614 – 9632.

Lin, J. & Stein R.S., 2004. Stress triggering in thrust and subduction earthquakes and stress interaction between the southern San Andreas and nearby thrust and strike-slip faults, *J. Geophys. Res.,* **109**, B02303, doi:10.1029/2003JB002607.

Livieratos, E., 1980. Crustal deformations from geodetic measurements, *Boll. Geofis. Teor. Appl.,* **22**, 255–260.

Lyon-Caen, H., 1980. Séismes du Frioul (1976): modèles de source à l'aide de sismogrammes synthetiques d'ondes de volume, Thesis, Université Paris VII.

Mahsas, A., Lammali K., Yelles K., Calais E., Freed A.M. & Briole P., 2007. Shallow afterslip following the 2003 May 21, Mw = 6.9 Boumerdes earthquake, Algeria, *Geophys. J. Int.,* doi:10.1111/j.1365-246X.2007.03594x.

Malinverno, A. & Ryan W. B., 1986. Extension in the Tyrrhenian Sea and shortening in the Apennines as arc migration driver by the sinking of the lithosphere, *Tectonics,* **5**, 227 – 245.

Marshal, G.A., Stein R.S. & Thatcher W., 1991. Faulting geometry and slip from co-seismic elevation changes: the 18 October 1989, Loma Prieta, California, Earthquake, *Bull. Seismol. Soc. Am.,* **81**, 5, 1660 – 1693.

Matsu'ura, M., Iwasaki T., Suzuki Y. & Sato R., 1980. Statical and dynamical study on faulting mechanism of the 1923 Kanto earthquake, *J. Phys. Earth,* **28**, 119 – 143.

McKenzie, D., 1972. Active tectonics of the Mediterranean region, *Geophys. G. R. Astron. Soc.,* **30**, 109 – 185.

Metropolis, N., Rosenbluth A., Teller A. & Teller E., 1953. Equation of state calculations by fast computing machines, *J. Chem. Phys.,* **21**, 1087 – 1092.

Minster, J.B., Jordan T.H., Molnar P. & Haines E., 1974. Numerical modelling of instantaneous plate tectonics, *Geophys. J. R. astr. Soc.,* **36**, 541 – 576.

Monachesi, G. & Stucchi M., 1998. *DOM 4.1 an intensity database of damaging earthquakes in the Italian area*, http://emidius.mi.ingv.it/DOM/home.html

Mulargia, F. & Boschi E., 1983. The 1908 Messina earthquake and related seismicity, *Proc. Int. School Phys. E. Fermi,* Earthquakes: observation, theory and interpretation, 493 – 518.

Murray, M.H., Marshal G., Lisowski M. & Stein R., 1996. The 1992 M=7 Cape Mendocino, California, earthquake: Coseismic deformation at the south end of the Cascadia megathrust, *J. Geophys. Res.,* **101**, 17707 – 17725.

Nyst, M., Nishimura T., Pollitz F.F. & Thatcher W., 2006. The 1923 Kanto earthquake re-evaluated using a newly augmented geodetic data set, *J. Geophys. Res.,* **111**, B11306, doi:10.1029/2005JB003628.

Okada, Y., 1985. Surface deformation due to shear and tensile faults in a half-space, *Bull. Seism. Soc. Am.,* **75**, 1135–1154.

Patacca, E., Sartori R. & Scandone P., 1990. Tyrrehenian basin and Apenninic arcs. Kinematic relations since late Tortonian times, *Mem. Soc. Geol. Ital.,* **45**, 425 – 451.

Perniola, B., Bressan G. & Pondrelli S., 2004. Changes in failure stress and stress transfer during the 1976-77 Friuli earthquake sequenze, *Geophys. J. Int.,* **156**, 297 – 306.

Peruzza L., Poli M.E., Rebez A., Renner G., Rogledi S., Slejko D. & Zanferrari A., 2002. The 1976-1977 seismic sequence in Friuli: new seismotectonic aspects, *Mem. Soc. Geol. It.,* **57**, 391-400.

Peyret, M., Chery J., Djamour Y., Avallone A., Sarti F., Briole P. & Sarpoulaki M., 2007. The source motion of 2003 Bam (Iran) earthquake constrained by satellite and round-based geodetic data, *Geophys. J. Int.,* doi:10.1111/j.1365-246X.2007.03358.x

Pino, A. N., Giardini D. & Boschi E., 2000. The December 28, 1908, Messina Straits, southern Italy, eartuquake: Waveforn modeling of regional seismograms, *J. Geophys. Res.,* **105**, 473 – 25, 492.

Poli, M.E., Peruzza L., Rebez A., Renner G., Slejko D. & Zanferrari A., 2002. New seismotectonic evidence from the analysis of the 1976–1977 and 1977–1999 seismicity in Friuli (NE Italy), *Boll. Geof. Teor. Appl.,* **43**, 53–78.

Pollitz, F.F., Nyst M., Nishimura T. & Thatcher W., 2005. Coseismic slip distribution of the 1923 Kanto earthquake, Japan, *J. Geophys. Res.,* **110**, doi:10.1029/2005JB003638.

Pondrelli, S., Ekström G. & Morelli A., 2001. Seismotectonic re-evaluation of the 1976 Friuli, Italy, seismic sequence, *J. Seismol.,* **5**, 73–83.

Prescott, W. H., 1976. An extension of Frank's method for obtaining crustal shear strains from survey data, *Bull. Seism. Soc. Am.,* **66**, No. 6, 1847 – 1853.

Press W.H., Teukolsky S.A., Vetterling W.T. & Flannery B.P., 1992. *Numerical Recipes in C: The Art of Scientific Computing, 2nd ed.,* Cambridge University Press, Cambridge, p. 99.

Reid, H.F., 1910. *The Mechanics of the Earthquake*, Vol. II of The California Earthquake of April 18, 1906, Report of the State Earthquake Investigation Commission, A.C. Lawson, Chairman, Carnegie Institution of Washington Publication 87, p 192. (reprinted 1969).

Rosembaum, G., Lister G.S. & Duboz C., 2002. Reconstruction of the tectonic evolution of the western Mediterranean since the Oligocene, *Journal of the Virtual Explorer,* **8**, 107 – 130.

Rothman, D.H., 1985. Nonlinear inversion, statistical mechanics, and residual statics estimation, *Geophysics,* **50**, 2784 – 2796.

Rothman, D.H., 1986. Automatic estimation of large residual statics corrections, *Geophysics,* **51**, 337 – 346.

Sambridge, M. 1999. Geophysical Inversion with a Neighbourhood Algorithm -I. Searching a parameter space, *Geophys. J. Int.,* **138** , 479 – 494.

Savage, J.C. & Prescott W.H., 1978. Asthenospher readjustment and the earthquake cycle, *J. Geophys. Res.,* **83**, 3369-3376.

Savage, J.C., 1983. Strain accumulation in Western United States, *Ann. Rev. Earth Planet. Sci.,* **11**, 11 – 43.

Savage, J.C., Prescott W.H., Lisowski M. & King E., 1981. Strain accumulation in Southern California, 1973-1980, *J. Geophys. Res.,* **86**, 6991 – 7001.

Savage, J.C., 1990. Equivalent strike-slip earthquake cycles in half-space and lithosphere-asthenosphere Earth models, *J. Geophys. Res.,* 95, 4873 – 4879.

Schick, R., 1977. Eine seismotektonische Bearbeitung des Erdbebens von Messina im Jahre 1908, *Geol. Jhrb.,* **11**, 74 (in German).

Selvaggi, G. & Chiarabba C., 1995. Seismicity and P-wave velocity image of the southern Tyrrhenian zone, *Geophys. J. Int.,* **121**, 818 – 826.

Sen, M.K. & Stoffa P.L., 1991. Nonlinear one-dimensional seismic waveform inversion using simulated annealing, *Geophysics,* **56**, 1624 – 1638.

Serpelloni, E., Anzidei M., Baldi P., Casula G. & Galvani A., 2005. Crustal velocità and strain-rate fields in Italy and surrounding region: new results from the analysis of permanent and non-premanent GPS stations, *Geophys. J. Int.,* **161**, 861-880.

Slejko, D., Carulli G.B., Nicolich R., Rebez A., Zanferrari A., Cavallin A., Dogliosi C., Carraio F., Castaldini D., Illecito V., Semenza E. & Zanolla C., 1989. Seismotectonics of the Eastern Southern Alps: a review, *Boll. Geof. Teor. Appl.,* **31**, 109 – 136.

Stoffa, P.L. & Sen M.K., 1991. Nonlinear multiparameter optimization using genetic algorithms: Inversion of plane wave seismograms, *Geophysics,* **56**, 1794 – 1810.

Sudhaus, H. & Jonsson S., 2007. Improvement of fault model estimations by using multiple datasets and full data covariance: an application to the Kleifarvatn earthquake, Iceland, *Fringe 2007 Abstract Book,* 46.

Talamo, R., Pampaloni M. & Grassi S., 1978. Risultati delle misure di livellazione di alta precisione eseguite dall'Istituto Geografico Militare nelle zone del Friuli interessate dalle recenti attività sismiche, *Boll. Geod. Sci. Aff.,* **37**, 61–75.

Thatcher, W., 1979. Horizontal crustal deformation from historic geodetic measurements in Southern California, *J. Geophys. Res.,* **84**, 2351 – 2370.

Thatcher, W., 1979. Systematic inversion of geodetic data in Central California, *J. Geophys. Res.,* **84**, 2281-2295.

Thatcher, W., 1993. The earthquake cycle and its role in the long-term deformation of the continental lithosphere, *Ann. Geofis.,* **36**, 13 – 24.

Thatcher, W., Marshall G. & Lisowski M., 1997. Resolution of fault slip along the 470-km-long rupture of the great 1906 San Francisco earthquake and its implications, *J. Geophys. Res.,* **102**, 5353 – 5367.

Tortorici, L., Monaco C., Tansi C. & Cocina O., 1995. Recent and active tectonics in the Calabrian Arc (southern Italy), *Tectonophysics,* **243**, 37 – 55.

Valensise, G. & Pantosti D., 1992. A 125 Kyr-long geological record of seismic source repeatability: the Messina Straits (southern Italy) and the 1908 earthquake (M_s 7½), *Terra Nova,* **4**, 472 – 483.

Vanicek, P. & Krakiwsky E.J., 1986. *Geodesy: the Concepts*, Elsevier, p.714.

Venturini, C., Astori A. & Cisotto A., 2004. The Late Quaternary evolution of the Friuli upper plain (NE Italy), *Mapping Geology In Italy,* APAT, S.E.L.C.A., Firenze, p. 336.

Walter, W.R., 1993. Source parameters of the June 29, 1992 Little Skull mountain earthquake from complete regional waveforms at a single station, *Geophys. Res. Lett.,* **20**, 403 – 406.

Ward, S.N. & Barrientos S.E., 1986. An inversion for slip distribution and fault shape from geodetic observations of the 1983, Borah Peak, Idaho, earthquake, *J. Geophys. Res.,* **91**, 4909 – 4919.

Wessel, P. & Smith W.H.F., 1995. New, improved version of the Generic Mapping Tools Released, *EOS Trans. AGU,* **79**, 579.

Wortel, M.J.R. & Spakman W., 2000. Subduction and slab detachment in the Mediterranean-Carpathian region, *Science,* **290**, 1910 – 1917.

Wright T.J., Parsons B.E., Jackson J.A., Haynes M., Fielding E. J., England P.C. & Clarke P.J., 1999. Source parameters of the 1 October 1995 Dinar (Turkey) earthquake from SAR interferometry and seismic bodywave modelling*, Earth and Planet. Sci. Lett.,* **172**, 23-37.

Yu, E. & Segall P., 1996. Slip in the 1868 Hayward earthquake from the analysis of historical triangulation data, *J. Geophys. Res.,* **101**, 16101 – 16118.

Zanferrari, A. et al., 1982. Evoluzione neotettonica dell'Italia nord-orientale, *Mem. Soc. Geol.,* **35**, 355 – 376.

Zeng, Y. & Anderson G., 1996. A composite source model of the 1994 Northridge earthquake using genetic algorithms, *Bull. Seism. Soc. Am.,* **86**, S71 – S83.

Zhao, L.S. & Helmberger D.V., 1994. Source estimation from broadband regional seismograms, *Bull. Seism. Soc. Am.,* **84**, 91 – 104.

Zumberge, J.F., Heflin M.B., Jefferson D.C., Watkins M.M. & Webb F.H., 1997. Precise point positioning for the efficient and robust analysis of GPS data from large networks, *J. Geophys. Res.,* **102**, 5005 – 5017.